IGNITION BY WATER HAMMER

J.-C. VEILLEUX
S. A. CORONEL
J. E. SHEPHERD
GRADUATE AEROSPACE LABORATORIES
CALIFORNIA INSTITUTE OF TECHNOLOGY
PASADENA, CA 91125

GALCIT REPORT EDL2019.001

Published by California Institute of Technology

IGNITION BY WATER HAMMER

Jean-Christophe Veilleux (Current address: Eli Lilly and Company, Indianapolis, IN)
Stephanie A. Coronel (Current address: Sandia National Laboratories, Albuquerque, NM)
Joseph E. Shepherd
Graduate Aerospace Laboratories
California Institute of Technology
Pasadena CA 91125

GALCIT REPORT EDL2019-001

December 2019

Abstract

The potential of water hammer events for igniting hydrogen-oxygen mixtures was examined in an experimental study. Compression waves simulating water-hammer events were created by projectile impact on a piston in a water-filled pipe terminated by a test section filled with gas. Triangular wave forms with peak pressures up to 50 MPa propagated through the piping system and compressed the gas in the test section. Experiments were carried out with both air and hydrogen-oxygen gas mixtures using high-speed video of the transparent test section, dynamic pressure and spectroscopic measurements to examine the motion of the water-gas interface and determine ignition thresholds. The impulsive acceleration of the water-gas interface and deceleration created by the compression of the gas resulted in Richtmyer-Meshkov and Rayleigh-Taylor instabilities that grew to create large distortions of the initially planar and horizontal water-gas interface. The gas layer was compressed in volume by up to a factor of 50 and the gas pressures increased to as high as 20 MPa within 2 to 4 ms. The distortion of the water surface during compression resulted in a significant increase in interfacial area and ultimately, creation of a two-phase mixture of water and compressed gas. Some ignition events were observed, but the dispersion and mixing of water with the gas almost completely suppressed the pressure rise during the ignition transient. Only by eliminating the instability of the water interface with a solid disk between the water and gas were we able to observe consistent ignition with significant pressure rises associated with the combustion.

Contents

1 Introduction **1**

2 Experimental methodology **3**
2.1 Facility . . . 3
2.2 Experimental procedure . . . 6
2.2.1 Non-reactive gas . . . 6
2.2.2 Reactive gas . . . 6

3 Air-filled volume results **8**
3.1 Effect of air volume height . . . 13
3.2 Effect of projectile velocity . . . 16
3.3 Suppression of interfacial instabilities . . . 18
3.4 Origin of interfacial instabilities . . . 18

4 Estimating ignition thresholds **27**
4.1 Reaction mechanism validation . . . 27
4.2 Critical pulse width . . . 28

5 Reactive gas volume Results **33**
5.1 Tests with a disc . . . 33
5.2 Tests without a disc . . . 36
5.3 Effect of N_2 dilution . . . 44

6 Conclusions **46**

References **48**

A Test Series A **51**

B Test Series B **52**

C Plots for Test Series B **54**

List of Figures

1 Diagram of experimental setup . . . 4
2 Diagram of test cell . . . 5
3 Schematic of plumbing . . . 7
4 z-t diagram of projectile impact on buffer . . . 8
5 Method of characteristics simulation of reflection . . . 10
6 x-t diagram of waves in liquid . . . 11
7 Pressure and images for test A014 . . . 12
8 Images for tests A011 and A024 . . . 13
9 Pressure traces for cases A011 and A024 . . . 14
10 Cell pressure vs h_0 . . . 15
11 Buffer velocity and peak pressure vs projectile velocity . . . 17
12 Pressure traces with and without disc . . . 21
13 Images of gas compression with and without disc . . . 22
14 Overlay of disc with test cell images . . . 23
15 Schematic of interface instability . . . 23
16 Gas height vs time, test B044 . . . 24
17 Gas height derivative vs time, test B044 . . . 25
18 Gas height acceleration vs time, test B044 . . . 26
19 Experimental and computed ignition delay time . . . 29
20 Mean error in predicted ignition delay time . . . 30
21 Critical pulse width simulation . . . 32
22 Test B044 cell volume and pressure histories . . . 34
23 Disc configuration peak pressure and ignition results . . . 35
24 Pressure in the pipe and test cell during test B060. . . . 36
25 Sequence of images of the test cell for test B060. . . . 37
26 Sequence of images of the top portion of the test cell for test B065. . . . 38
27 Spectra of the chemiluminescence for test B065. . . . 39
28 No disc configuration peak pressure and ignition results . . . 40
29 Sequence of images of the test cell for test B059. . . . 41
30 Pressure in the pipe and test cell during test B059. . . . 42
31 Pressure in the pipe and test cell during test B068. . . . 43
32 Comparison of three tests . . . 44
33 Critical pulse half-width for N_2 dilution . . . 45
34 Test B010 . . . 55
35 Test B011 . . . 56
36 Test B012 . . . 57
37 Test B014 . . . 58
38 Test B015 . . . 59
39 Test B016 . . . 60
40 Test B017 . . . 61
41 Test B018 . . . 62
42 Test B019 . . . 63
43 Test B020 . . . 64
44 Test B021 . . . 65
45 Test B022 . . . 66
46 Test B023 . . . 67
47 Test B024 . . . 68
48 Test B025 . . . 69
49 Test B026 . . . 70
50 Test B027 . . . 71
51 Test B028 . . . 72
52 Test B029 . . . 73

53 Test B030 . . . 74
54 Test B031 . . . 75
55 Test B032 . . . 76
56 Test B033 . . . 77
57 Test B034 . . . 78
58 Test B035 . . . 79
59 Test B036 . . . 80
60 Test B037 . . . 81
61 Test B038 . . . 82
62 Test B039 . . . 83
63 Test B040 . . . 84
64 Test B041 . . . 85
65 Test B042 . . . 86
66 Test B043 . . . 87
67 Test B044 . . . 88
68 Test B045 . . . 89
69 Test B046 . . . 90
70 Test B047 . . . 91
71 Test B048 . . . 92
72 Test B049 . . . 93
73 Test B050 . . . 94
74 Test B051 . . . 95
75 Test B052 . . . 96
76 Test B053 . . . 97
77 Test B054 . . . 98
78 Test B055 . . . 99
79 Test B056 . . . 100
80 Test B057 . . . 101
81 Test B058 . . . 102
82 Test B059 . . . 103
83 Test B060 . . . 104
84 Test B061 . . . 105
85 Test B062 . . . 106
86 Test B063 . . . 107
87 Test B064 . . . 108
88 Test B065 . . . 109
89 Test B066 . . . 110
90 Test B067 . . . 111
91 Test B068 . . . 112
92 Test B069 . . . 113
93 Test B070 . . . 114
94 Test B071 . . . 115
95 Test B072 . . . 116
96 Test B073 . . . 117
97 Test B074 . . . 118

List of Tables

1 Experiment dimensions, see Fig. 1 for nomenclature. 3
2 Series A test conditions 51
3 Series B test conditions 52

1 Introduction

Water hammer (Wylie and Streeter, 1993) is colloquial term for the generation and propagation of pressure transients within piping systems and the associated structural response. In piping systems, pressure transients are usually the result of the sudden opening or closing of valves when the fluid (gas or liquid) within the pipe is flowing rapidly or when a low-pressure piping system is connected by a rapidly opening valve or rupture disk to a high-pressure piping system. In piping systems that contain two-phase regions (liquid-vapor mixtures) or distinct regions of liquid and vapor, positive pressure transients may cause the compression of the vapor phase, possibly completely collapsing vapor bubbles or a vapor region. Pressure transients with a magnitude of 15-150 MPa can be obtained in liquid water with velocity changes on the order of 10-100 m/s; the pressure change scales directly with the velocity change since the motion in the water is acoustic at these amplitudes.

When a vapor bubble or region is composed of flammable or explosive vapors, compression may result in temperatures sufficiently high to cause ignition and explosion of the vapor. This is a known hazard (Hershkowitz and Dobratz, 1989) in handling liquid propellants and explosives (e.g., hydrazine or nitromethane) or industrial scale production of unstable compounds like tetrafluoroethylene (Ferrero et al., 2013). Pressure waves created by the ignition of a vapor bubble or region can propagate into the surrounding liquid explosive and initiate a propagating explosion or decomposition wave with highly destructive consequences (Ringer, 1985). This mechanism has been proposed by Leishear (2013) as being relevant to accidents in nuclear power plants.

When a bubble is surrounded by an inert liquid (e.g., a hydrogen-oxygen bubble in water), pressure waves in the liquid can result in individual bubbles exploding (Beylich and Gulhan, 1990, Mitropetros et al., 2006) or in the case of a bubbly liquid, may result in a *bubble detonation*, a self-sustaining wave of bubble collapse and ignition (Hasegawa and Fujiwara, 1982, Pinaev and Sychev, Nov-Dec 1987). The conditions under which individual bubble or propagating explosions occur depend on many factors including bubble size, void fraction, gas mixture composition and initiating pressure wave amplitude (see Ch. 4 and 5 of Kedrinskii (2005)). Of particular relevance for the present study are the microdroplets and interfacial area enhancement generated by the interactions of pressure waves with the bubbles. The formation of microdroplets and enhancement of interfacial area is due to the instability of the bubble surface created by the interaction with the pressure wave (Johnsen and Colonius, 2008) and subsequent nonspherical oscillations of the bubble volume (Brennen, 1995). The enhancement of water content due to vaporization can have a significant inhibiting effect on the ignition of the gas within a collapse of a single bubble.

In the present study we are not concerned with the ignition of a single bubble within a liquid but rather an extended volume of reactive gas that fills or partially fills the entire cross-section of a pipe. Specifically we consider a volume of gas within a vertical section of pipe that is bounded above by a closure (dead end) and below by a liquid (water) with a horizontal interface. Motivated by the observations of explosions of radiolysis gases in nuclear power plant piping (Naitoh et al., 2003b,a, Schulz et al., 2002) we have used a stoichiometric H_2-O_2 gas mixture in our ignition testing. A pressure wave produced by water hammer is incident on the liquid-gas interface from below and initiates the compression of the gas volume. This is an idealized situation and many other configurations are possible in industrial facilities. Our primary objective in choosing this configuration is to have a well-defined geometry that would result in sufficient compression that the potential for ignition due to compression by water hammer could be studied. A secondary objective is to provide data that will be of value for validation of numerical simulations.

The configuration we examine in this study is closely related to the rapid compression machine (RCM) (Goldsborough et al., 2017), which uses a piston to rapidly (within 10-30 ms) compress and hold a reactive mixture at an elevated pressure to enable measurements of autoignition chemistry at pressures and temperatures up to 8 MPa and 1200 K, respectively. Extensive testing has been carried out on H_2-air and syngas (H_2-CO)-air mixtures (See Table 2 of Goldsborough et al. (2017)) over a range of pressures between 0.5 and 8 MPa and temperatures from 855 to 1200 K. One of the goals of the present study is to examine the applicability of the RCM results to autoignition of H_2-O_2 mixtures by water hammer.

A variety of ignition behaviors are observed for syngas mixtures just as has been previously noted (Boeck et al., 2017) for shock compression of H_2-O_2 mixtures with various diluents. The "strong" ignition regime is characterized by nearly homogeneous reaction throughout the compressed volume and "mild" or "weak" ignition occurs through flame propagation originating at numerous ignition sites located throughout the volume. The origin and prediction of the boundary between weak and strong ignition regimes is an ongoing topic of research (Grogan and Ihme, 2018, Pal et al., 2017) and it is unclear how the results of RCM and shock tube studies will apply to the present situation. Water hammer compression superficially resembles RCM operation and we anticipate on the basis of the RCM data (see Fig. 34 of Goldsborough et al. (2017)) that at sufficiently high temperatures, above 1050-1100 K, strong ignition will

likely predominate. The ignition delay time, or time to ignition from initial compression, increases drastically with decreasing temperature for H_2-O_2 mixtures below about 1000 K and we anticipate below 900 K, ignition may not be possible due to the competing effects of turbulent mixing, heat transfer and vaporization.

The key difference between the present study and previous RCM or shock tube studies of autoignition is that the gas volume is being compressed by a liquid surface that is initially impulsively accelerated by a pressure wave and then continuously decelerated as the pressure in the gas volume increases during compression. This results in a combination of Richtmyer-Meshkov (due to the shock wave) and Rayleigh-Taylor (due to the deceleration) instabilities of the liquid-gas interface (Zhou, 2017). The relevance of these instabilities to ignition has already been pointed out in connection with the studies of bubble collapse through the creation of increased interfacial area and microdroplets, resulting in enhanced heat transfer and water vaporization, potentially inhibiting ignition and flame propagation. Although there have been numerous studies of Richtmyer-Meshkov instabilities at gaseous interfaces, there are fewer that examine liquid-gas interfaces in combination with the destabilizing effects of Rayleigh-Taylor instability. Flow visualization studies (Shi and Zhuo, 2009, Wang et al., 2001) with incident air shock waves and destabilizing interface acceleration show the characteristic bubble and spike interface instabilities that are characteristic of the nonlinear development of instabilities on gaseous interfaces. We anticipate that these instabilities will also occur in the water hammer case. An additional feature that we expect to observe in our tests and which is not present in the Shi and Zhuo (2009) or Wang et al. (2001) tests is the creation of cavitation below the surface (Ohtani and Ogawa, 2016) and a mist of microdroplets in the gas phase above due to the reflection of the pressure waves incident from the liquid side as tension waves; see Fig. 16 of Kleine (2010) and the discussion in Besov et al. (2002) and Kedrinskii (1978). Finally, another key difference is that in shock tube or RCM testing, the compressed gas is maintained at nearly constant temperature and pressure over a well defined test time while in the water hammer tests we performed, the compression process is almost immediately followed by an expansion so that the ignition process takes place under highly transient conditions. This creates the potential for quenching reactions during the expansion process and as a consequence, the critical conditions for ignition will depend not only on the magnitude of the compression but also on the rate of expansion.

The goals of our study were to examine the issues discussed above through an experimental study. We developed a facility (Section 2) to simulate water hammer compression of a gas volume and carried out experiments to characterize the compression of both inert (Section 3) and reactive gas (Section 5) volumes. We use (Section 4) detailed chemical kinetic modeling and a control volume analysis of the compression process with a model volume history to examine the potential for ignition for adiabatic compression. A set of tests (Section 5) with and without a solid disk (to suppress surface instabilities) demonstrate the dramatic effect of interfacial instabilities on the ignition and combustion process.

2 Experimental methodology

2.1 Facility

The experiments were performed in a stainless steel U-shaped pipe, shown in Fig. 1, with an inner diameter and thickness of approximately 52 mm and 4 mm, respectively. A transparent section (referred to as the test cell) was mounted on a standard stainless steel pipe flange on the right end of the pipe. The flange was 20 mm thick and welded to the pipe end. The test cell was constructed of a hollow, optical-quality polycarbonate cylinder with an inner diameter of 50 mm, outer diameter of 178 mm and a height of 127 mm. A section of the outside of the test cell was machined flat and vapor polished to improve the quality of visualization of the interior of the cell. The test cell top closure was a 165 mm diameter, 20 mm thick stainless steel flange with vacuum fittings for a pressure transducer, P_{cell}, and plumbing for filling the cell with the reactive gas mixture. Additional pressure transducers (P_1, P_2, P_3, and P_4) were placed along the length of the pipe; the transducers relative distances, d, are given in Table 1. The blue and yellow regions in Fig. 1 correspond to water and gas, respectively.

Parameter	Value
d_1	179 mm
$d_{1\rightarrow 2}$	308 mm
$d_{2\rightarrow 3}$	597 mm
$d_{3\rightarrow \text{cell}}$	627 mm
m_p	2.236 kg
m_b	0.431 kg

Table 1: Experiment dimensions, see Fig. 1 for nomenclature.

A vertical gas-gun was used to generate a pressure transient by accelerating downward a projectile which impacted a buffer in contact with the water at the left end of the pipe. The buffer, shown in Fig. 1, was made of a polycarbonate rod with an outer diameter of 53.3 mm and height of 152.4 mm. A hole with partial threads was bored through the buffer center axis, making it possible to evacuate the air between the buffer and water. The buffer also had gland seals (not shown) at two axial locations. The projectile, shown in Fig. 1, was made of a stainless steel rod with an outer diameter of 49.9 mm and height of 149.2 mm. The projectile had two gland seals, one near each end. The buffer and projectile masses, m_b and m_p, respectively, are indicated in Table 1. A detailed description of the gas-gun and its operation can be found in Inaba and Shepherd (2009). In the present study, the gas-gun, shown in Fig. 1b, accelerates projectiles up to 35 m/s by using compressed air with pressures up to 550 kPa (80 psig). A projectile is loaded in the gun barrel; subsequently, the volume between the top of the projectile and top of the barrel is evacuated so the projectile can move to the top of the barrel. The gas-gun reservoir has four ports that are open to the barrel; however, the gland seals on the projectile prevent leaks from the reservoir to the barrel. The reservoir is filled to the desired pressure, P_R; shortly after, the vacuum line is closed and an air valve connecting the evacuated space to the reservoir is opened. Once the air valve is opened, compressed air fills the previously evacuated space and causes the projectile to move downward, exposing the reservoir ports. With the reservoir ports exposed, the compressed air rushes into the space above the projectile and causes it to accelerate downward. As shown in Fig. 1a, the barrel is axially aligned with the buffer in the U-shaped pipe; the projectile impacts the buffer after exiting the barrel.

A close-up schematic of the test cell is shown in Fig. 2. The test cell was designed to withstand the high-pressure transients generated within the liquid and any gas explosion during a test. Figure 2 shows cross-sectional cuts of two test cell configurations used in the present study: (a) without and (b) with a polypropylene disc separating the gas and water. The polypropylene disc had a thickness of 25.4 mm, and two O-rings to provide gland seals.

PCB 113B23 high frequency pressure transducers (P_1, P_2, P_3, P_4, and P_{cell}) were used in the experiment along with Phantom V710 (2,600 to 88,000 fps) and Phantom V7.3 (12,000 fps) high-speed cameras to image the test cell and projectile-buffer interaction at impact, respectively. Additionally, an Ocean FX spectrometer was used to measure the optical radiation emitted by the igniting flammable mixture; the spectrometer was implemented in a few test cases. The cameras and data-acquisition were triggered off of P_1 shortly after the impact of the projectile on the buffer. The pressure signals were digitized with a Yokogawa DL850, 12-bit vertical resolution oscilloscope at 10 MHz. A TTL output signal from the oscilloscope was used to trigger the high-speed camera and spectrometer.

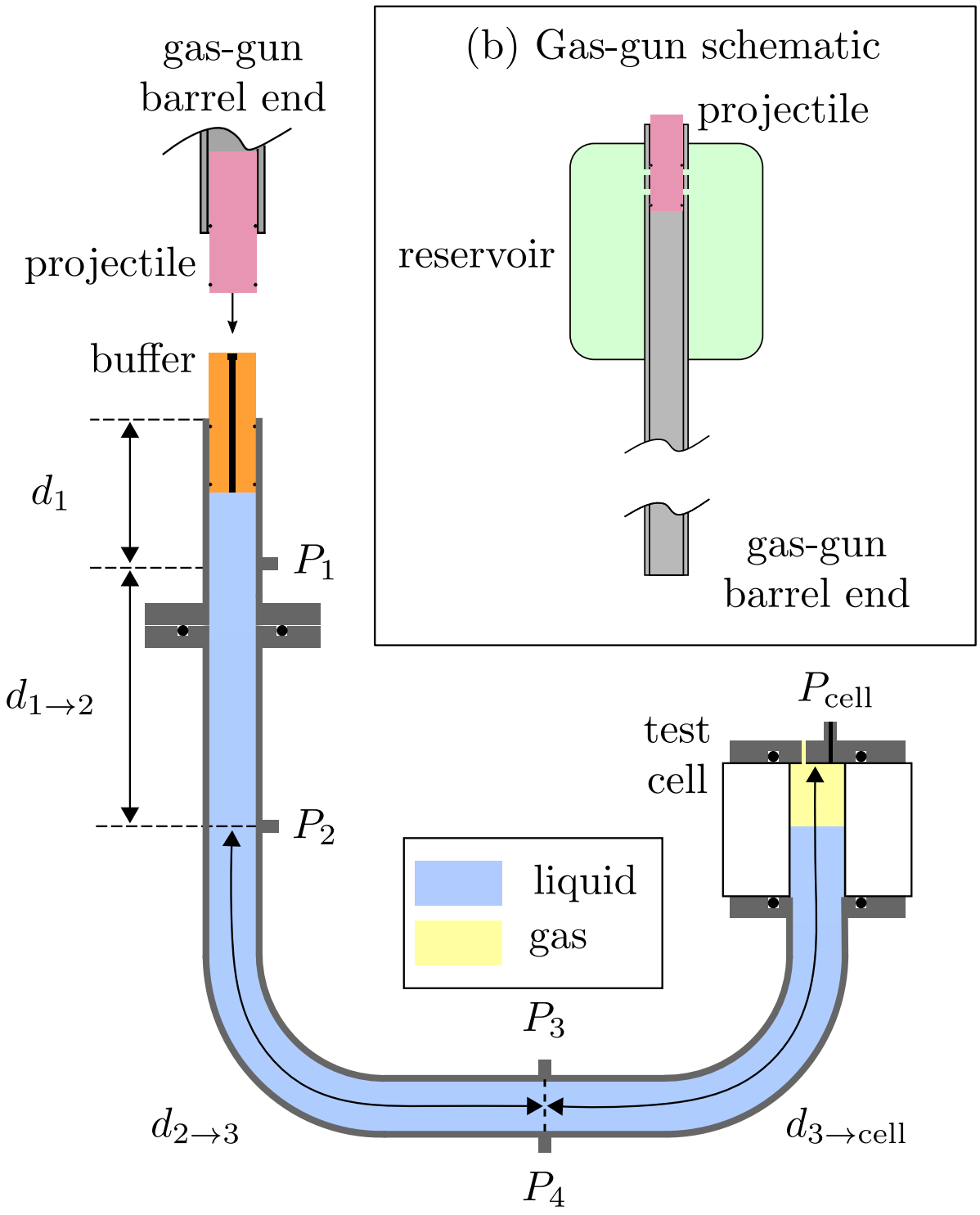

Figure 1: Schematics of (a) water hammer experiment fixture and (b) gas-gun. Dimensions are given in Table 1

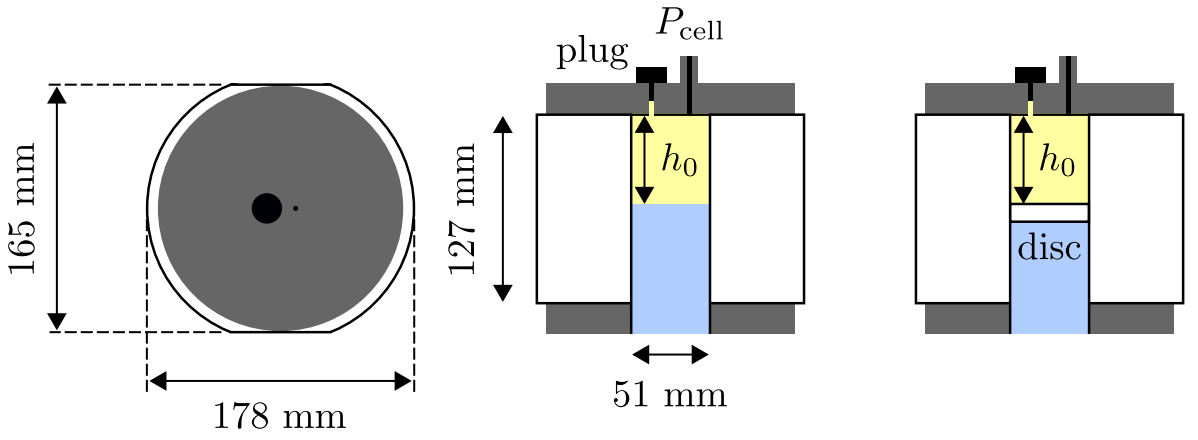

Figure 2: Schematic of (a) top-view of test cell, along with (b) no-disc and (b) disc configurations.

2.2 Experimental procedure

2.2.1 Non-reactive gas

To perform an experiment with air in the test cell, the test cell plug and buffer were removed. Water was introduced through the buffer-side open end of the pipe until the desired height h_0 of the gas volume was reached in the test cell; the water height was monitored with the high-speed camera. Once h_0 was reached, the test cell plug was replaced; subsequently, more water was introduced until the free surface was aligned with the top of the pipe open end. At that point, the buffer was plunged into the pipe; a small diameter bore through the center of the buffer allowed for water to spill out as the buffer was pushed farther into the pipe. The buffer was positioned such that both gland seals were in contact with the inside surface of the pipe. Finally, with the buffer properly positioned, a socket-head sealing screw was introduced into the buffer to plug the small diameter bore. For the initial round of tests, the projectile was accelerated by dropping it without O-rings from the top of the gun barrel; the projectile was accelerated by gravity alone and had a velocity of approximately 6.5 to 6.7 m/s when it impacted the buffer. After impact, the buffer suddenly accelerated leading to the formation of a primary compression wave in the water in the pipe. For the second round of tests, the projectile was placed at the top of the gun barrel and accelerated by the pressurized air in the reservoir. The projectile exited the barrel with velocities between 5 and 35 m/s depending on the pressure in the gun reservoir.

2.2.2 Reactive gas

The test cell plumbing was modified for testing with reactive mixtures, shown in Fig. 3. Prior to performing an experiment, an auxiliary stainless steel vessel was pressurized with the reactive mixture prepared using the method of partial pressures. To perform an experiment, valves V_3, V_4, and V_5 were closed and valves V_1 and V_2 were opened; the buffer was removed from the other pipe end. Water was introduced through the buffer-side pipe end until the test cell was completely flooded. At that point V_1 and V_2 were closed, and V_4 and V_5 (needle valve) were opened to evacuate the lines. Once the lines were evacuated, V_4 and V_5 were closed and subsequently V_3 was opened. Next, V_5 was opened a small amount and then V_1 was opened to fill the test cell with the reactive mixture contained in the pressurized cylinder. Since the pressure in the cylinder was greater than atmospheric pressure, the water was pushed down and replaced with the reactive mixture. V_5 remained open until the desired reactive mixture volume was reached, immediately followed by closure of V_1 and V_3. The buffer was introduced prior to filling the test cell with the reactive mixture. After the test cell was filled with gas, the socket head sealing screw was placed in the buffer. For the third round of tests, the projectile was placed at the top of the gun barrel and accelerated by the pressurized air in the reservoir.

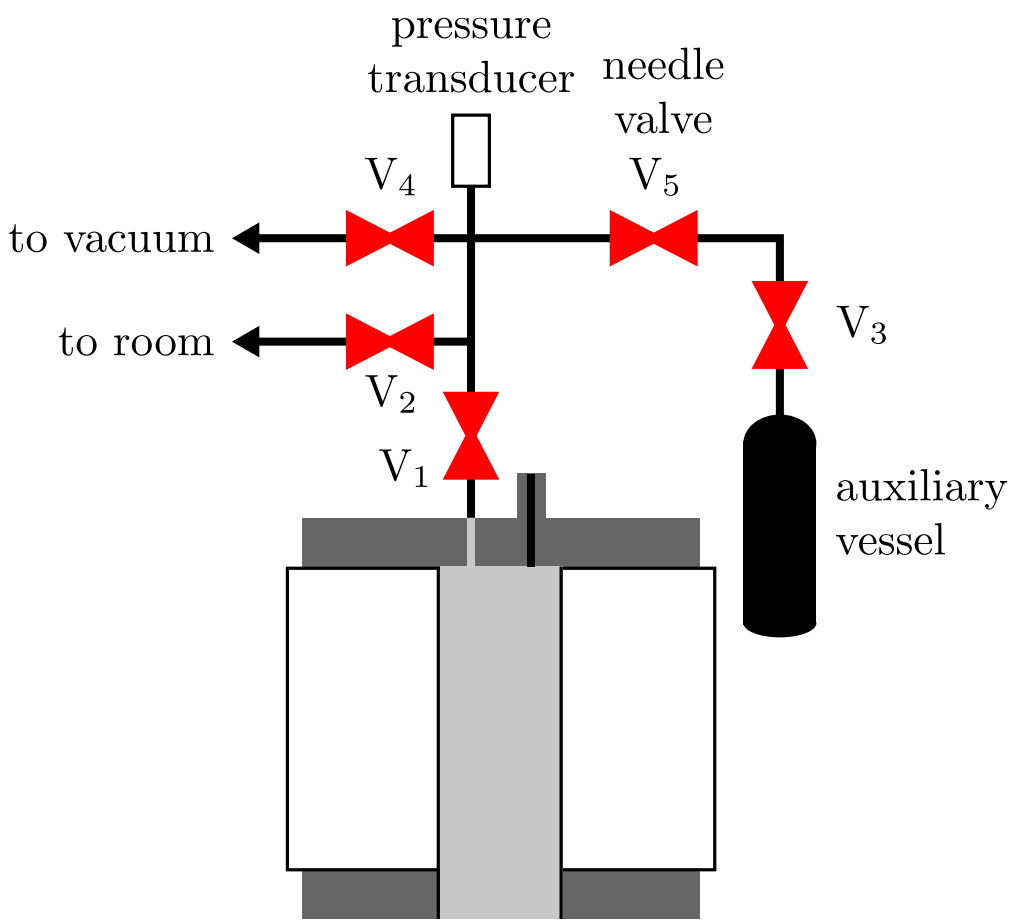

Figure 3: Schematic of test cell plumbing for reactive mixture testing.

3 Air-filled volume results

Prior to testing with the reactive mixture in the test cell, two series of experiments were performed to investigate the effect of initial gas volume height and projectile velocity on the compression behavior of air in the test cell. In the first series "A", 33 tests were performed at a fixed initial projectile velocity (gravity accelerated projectile), $v_p \approx$ 6.5-6.7 m/s, while varying the initial height of the air volume in the test cell. In the second series "B", 41 tests were carried out at three different gas heights varying the initial projectile velocity from 5 to 35 m/s. The nominal initial temperature, T_0, and pressure, P_0, in the test cell were 298 K and 101 kPa, respectively. In this study, all subsequent references to pressure correspond to the gauge pressure. Conditions and key results for the tests are tabulated in Appendices A and B. An extensive set of plots for the B series is given in Appendix C.

Figure 4 shows the trajectories of the lower face of the projectile and upper face of the buffer following a 6.66 m/s projectile impact. The distance and time axes are relative to the instant and location of impact. The impact appears to be essentially inelastic and for the first 2-3 ms, the projectile and buffer motion are coincident. The buffer is initially accelerated to about 75-80% of the projectile velocity then immediately begins to decelerate as pressure waves propagate away from the buffer into the water. The projectile essentially comes to a halt after transferring energy to the buffer and the buffer continues to move into the liquid for about 11 ms until the wave processes in the liquid reverse the direction of motion. The projectile accelerates downward due to gravity after halting due to the initial impact and eventually the projectile and buffer will collide and then rebound 23 ms after the initial impact.

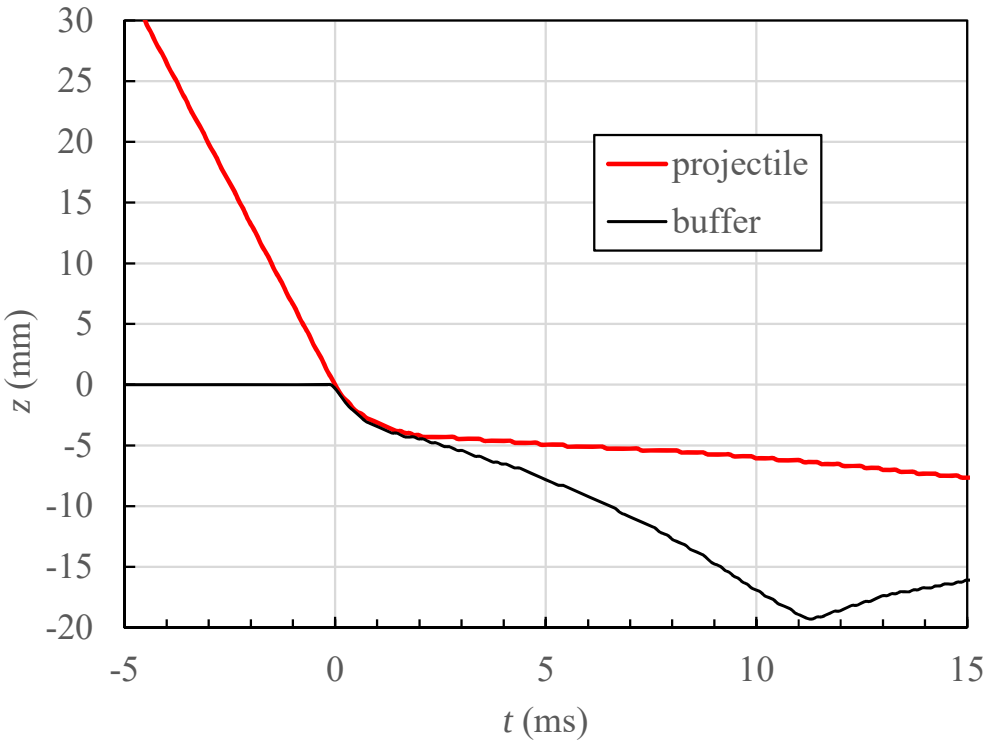

Figure 4: z-t diagram showing trajectory of projectile lower face and buffer upper face before and after impact of the projectile on the buffer. Test A014.

Figure 6 shows pressure traces and a schematic of expected wave propagation in the liquid column following projectile-buffer impact. A primary compression wave (solid blue line) is generated that travels from the buffer-liquid interface toward the liquid-gas interface and is followed immediately by expansion waves created as the buffer decelerates (Shepherd and Inaba, 2010). The first pressure waves on transducers P_1, P_2, P_3 and P_4 all consist of a sharp rise (less than 100 μs) followed by a decay to ambient pressure over 1-2 ms, which is consistent with the deceleration of the buffer shown in Fig. 4.

The peak pressure rise in the liquid is 8.9 MPa at P_1, 8.2 MPa at P_2, and 7.8 MPa at P_3 and P_4. The initial

magnitude is in agreement with the expected value according to acoustic theory where $P_{\max} \approx \rho c v_p = 9$ MPa, v_p is the projectile velocity at impact and c is the Korteweg speed (Shepherd and Inaba, 2010) of 1380 m/s, which is slightly less than the liquid sound speed due to the compliance of the piping. The decay in amplitude between the location of P_1 and P_3 can be seen more clearly in Fig. 7 and is due to the interaction of the trailing expansion with leading pressure wave during the propagation distance of 0.9 m.

At the liquid-gas interface within the test cell (dashed horizontal line at 1.35 m in Fig. 6), the compression wave reflects as a tension wave (trajectory indicated by the dashed blue line) due to the larger acoustic impedance of water compared to air. A small amplitude compression pulse is transmitted into the gas. Just after the instant of reflection, we can use pressure-velocity diagrams to find the amplitude of the reflected and transmitted waves. The pressure amplitude of the wave reflected back into the water is

$$\Delta P_r = \left[\frac{\rho_g a_g - \rho_l a_l}{\rho_g a_g + \rho_l a_l}\right] \Delta P_i \ , \tag{1}$$

the pressure amplitude of the wave transmitted into the gas is

$$\Delta P_t = \left[\frac{2\rho_g a_g}{\rho_g a_g + \rho_l a_l}\right] \Delta P_i \ , \tag{2}$$

and the peak velocity induced by the reflected and transmitted waves, as well as the velocity of the gas-liquid interface is

$$\Delta u_r = \left[\frac{2\rho_l a_l}{\rho_l a_l + rho_g a_g}\right] \Delta u_i \ , \tag{3}$$

where ρ_g and ρ_l are the gas and liquid densities, respectively, a_g and a_l are the sound speeds, ΔP_i and Δu_i is the pressure and velocity amplitude of the incident wave, and ΔP_r and Δu_r is the pressure and velocity amplitude of the reflected wave. Because the acoustic impedance ρa of air (4.1×10^2 kg·m^{-2}·s^{-1}) is so much smaller than that of water (1.5×10^9 kg·m^{-2}·s^{-1}), $\Delta P_r \approx -\Delta P_i$ and $\Delta u_r \approx 2\Delta u_i$. For example, consider a 40 MPa amplitude incident pressure pulse, the reflected pressure is -39.878 MPa. A 22 kPa compression pulse will be transmitted in the gas and the interface velocity will be 53.318 m·s^{-1}, slightly less than double the incident wave velocity amplitude of 26.667 m·s^{-1}. As the reflected wave propagates back into the liquid, the superposition of the reflected and incident waves will quickly result in a region of negative pressure (tension) between the reflected wave and the liquid-gas interface. This process is illustrated in Fig. 5 with a simulation of reflection from the gas-liquid interface using the method of characteristics (Wylie and Streeter, 1993) and treating the interface as a constant pressure boundary condition. The domain length (1.5 m) and pulse duration (2 ms) are chosen to simulate the present experiments with an impact velocity of $\sim$30 m·s^{-1}.

The liquid can not sustain the large negative pressure (tension) for an extended period of time and vapor-filled cavities grow from microscopic nuclei to create a two-phase mixture in the liquid in the region adjacent to the interface. Cavitation due to pressure wave reflection from a free surface has been observed by a number of researchers (Trevena, 1987, Williams and Williams, 2004). The threshold for cavitation onset and the time required for the appearance of visible cavities following tensile stressing will depend on a number of factors, particularly water chemistry, dissolved gas content, cleanliness and finish of the container surface. Previous researchers (see the review of Williams and Williams, 2004) report effective tensile strengths ranging from 0.8 to 30 MPa using various methods of static and dynamic stressing. For pressure wave reflection creation of cavitation in degassed, de-ionized water, Williams and Williams proposes an upper bound on the threshold value of incident pressure of $\sim$10 MPa; we observe cavitation in all of tests we conducted which have $5 < \Delta P_i < 50$ MPa. The low effective tensile strength we observe (< 5 MPa) is likely due to an abundance of nuclei (Mørch, 2015) in the water and nucleation sites on the pipe surfaces that are inevitable on commercial materials with rough finishes. The thresholds we observe are consistent with those of other researchers Williams and Williams (2004), Mørch (2015), Brennen (1995) using similar methods without any special attention to surface preparation or cleanliness.

Cavitation results in a two-phase flow with oscillating cavities or bubbles containing dissolved air and water vapor, the vapor pressure of water at the temperature of the tests is only 3.5 kPa. The pressure within the air volume adjacent

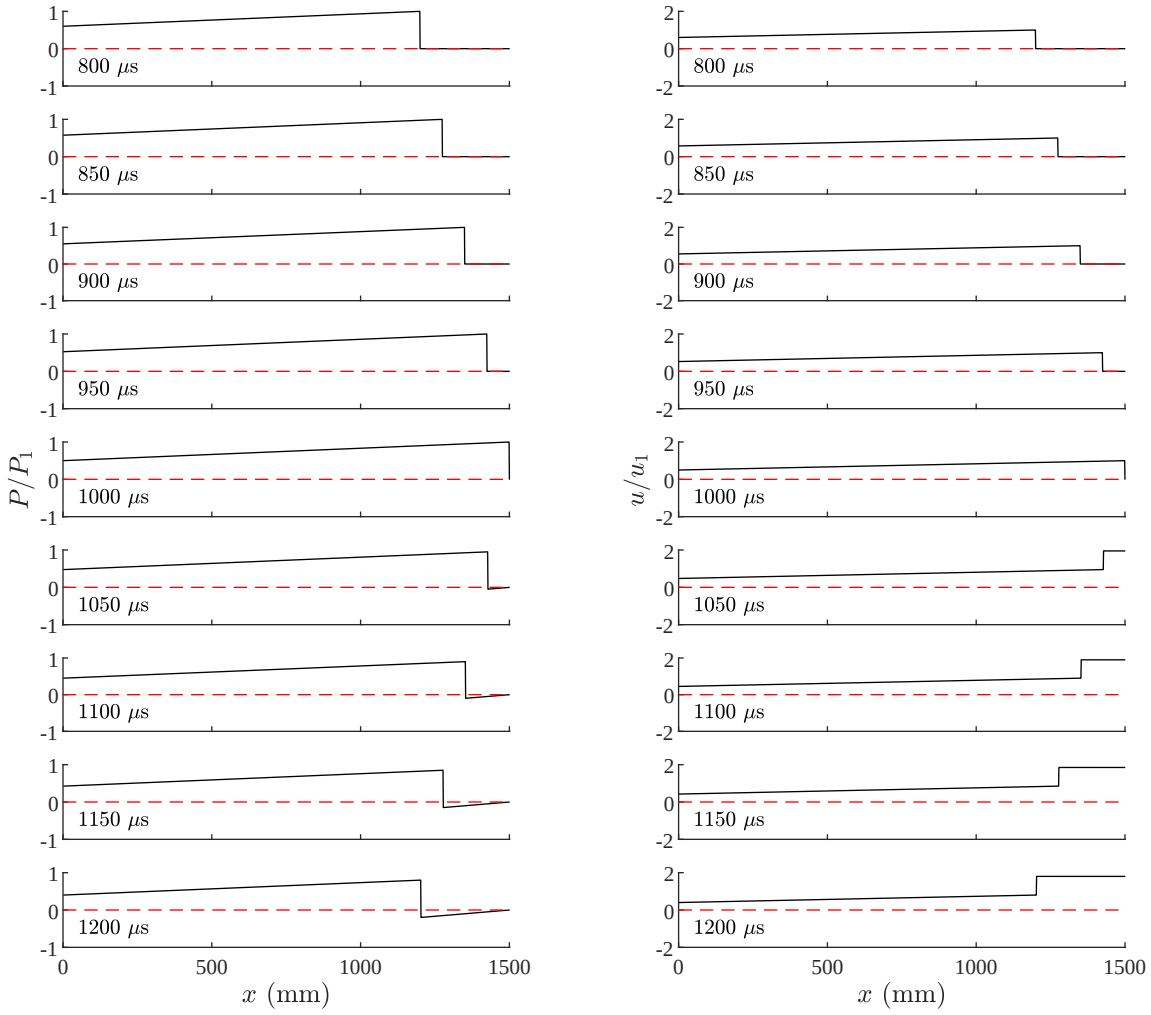

(a) (b)

Figure 5: Method of characteristics simulation of reflection of a triangular pressure pulse from a liquid-gas interface simulated as a free surface ($P = P_0$.) Spatial profiles at selected times before and after reflection for a) pressure, and b) velocity. Instant of wave reflection is 1000 μs, P_1 = 40 MPa, u_1 = 26.7 m·s^{-1}.

to the interface remains positive and increasing as the air volume decreases due to the compression by motion of the water. This generates pressure waves which propagate from the air-water interface back into the liquid, causing the cavities to collapse in the region next to the interface. The cavitation occurs both within the bulk liquid and at the surface of the test cell as visualized by the bubbles seen in Fig. 7b beginning at 1.6 ms. Propagation of the expansion waves from the test cell to the buffer will result in cavitation throughout the piping system (Veilleux and Shepherd, 2019, Inaba and Shepherd, 2010) creating an extended vaporous region with low wave speed and density. This explains the absence of any observable pressure rises associated with the nominal liquid wave trajectories shown in Fig. 6 between 2.5 and 5.5 ms. Instead there is an extended low pressure region in the liquid during this time.

Selected frames from the high-speed video of the test cell and a longer duration composite of the measured pressures for Test A014 are shown in Fig. 7. A notable feature at longer times is that P_3 shows a series of high-frequency

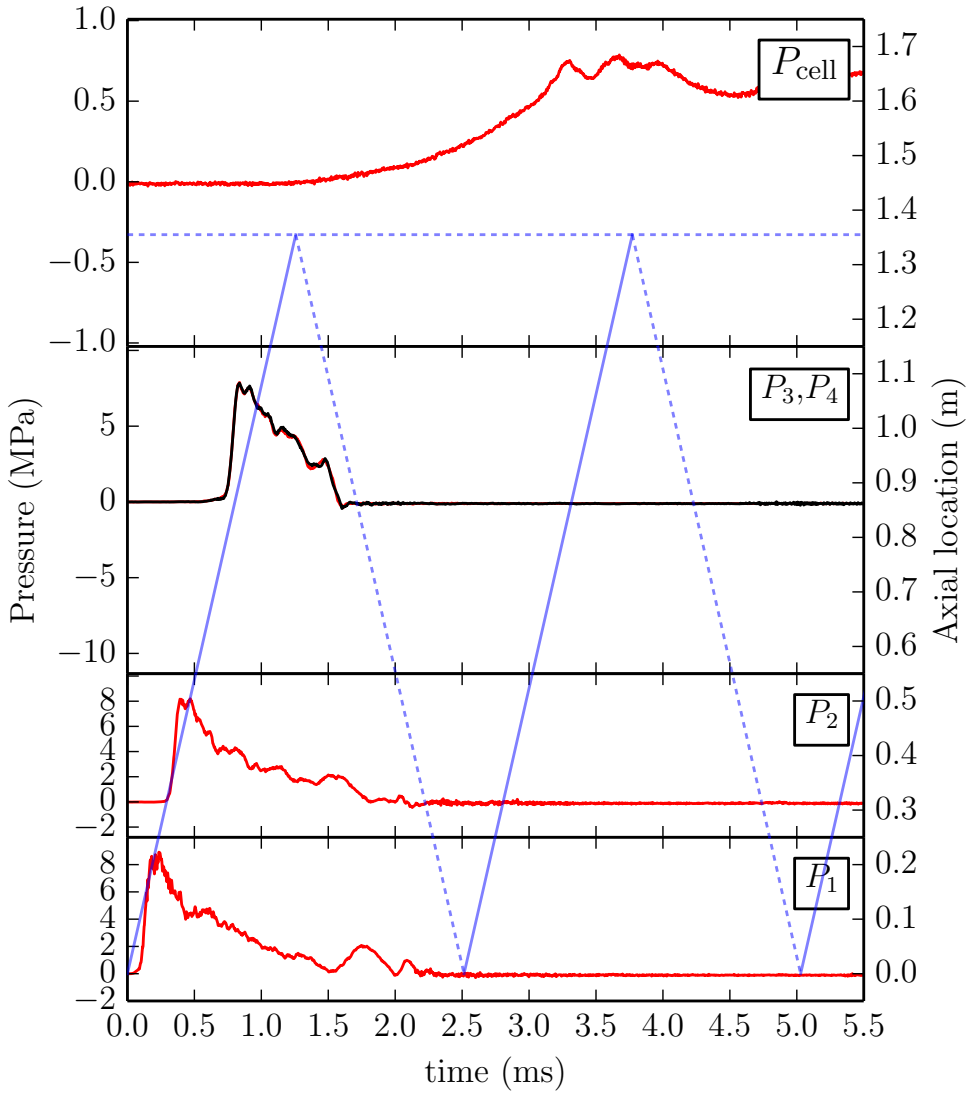

Figure 6: x-t diagram with measured pressures and nominal trajectories of waves in liquid following impact of the projectile on the buffer. Test A014.

pressure spikes starting at 6.5 ms that are likely due to bubbles collapsing near the transducer P_{cell}. The rise in pressure in the test cell, P_{cell}, is observed to begin at 2 ms; a pressure of approximately 0.8 MPa is first reached at 3.2 ms and the peak pressure of 1.0 MPa occurs at 7.3 ms. Figure 7b shows images of the air volume compression at selected times. The first frame corresponds to the approximate time of the arrival of the primary compression wave at the liquid-gas interface. The passage of a reflected tension wave can be observed by the formation and collapse of bubbles ($t > 1$ ms). Immediately following the arrival of the compression wave, the liquid column accelerates upwards, shown by the upward movement of the liquid-gas interface, and promptly starts decelerating. At 2.1 ms, the initially planar liquid-gas interface is visibly distorted. This distortion appears to originate from the instability of the interface due to a combination of effects: initially Ritchmyer-Meshkov instability due to the incident pressure wave followed by Rayleigh-Taylor instability due to the subsequent deceleration of the interface. The deceleration is caused by the increase in gas pressure due to the compression of the gas volume and decrease in the liquid pressure due to liquid wave dynamics. At 2.7 ms, the interface evolves into a structure consisting of gas bubbles that propagate downward into the liquid and liquid spikes or jets that propagate upward into the gas pocket. At 3.2 ms, the liquid splashes against the

top wall of the test cell; this time also corresponds to the first local maximum in P_{cell}. The first local minimum in P_{cell} is observed at approximately 4.3 ms corresponding to the expansion of the air volume.

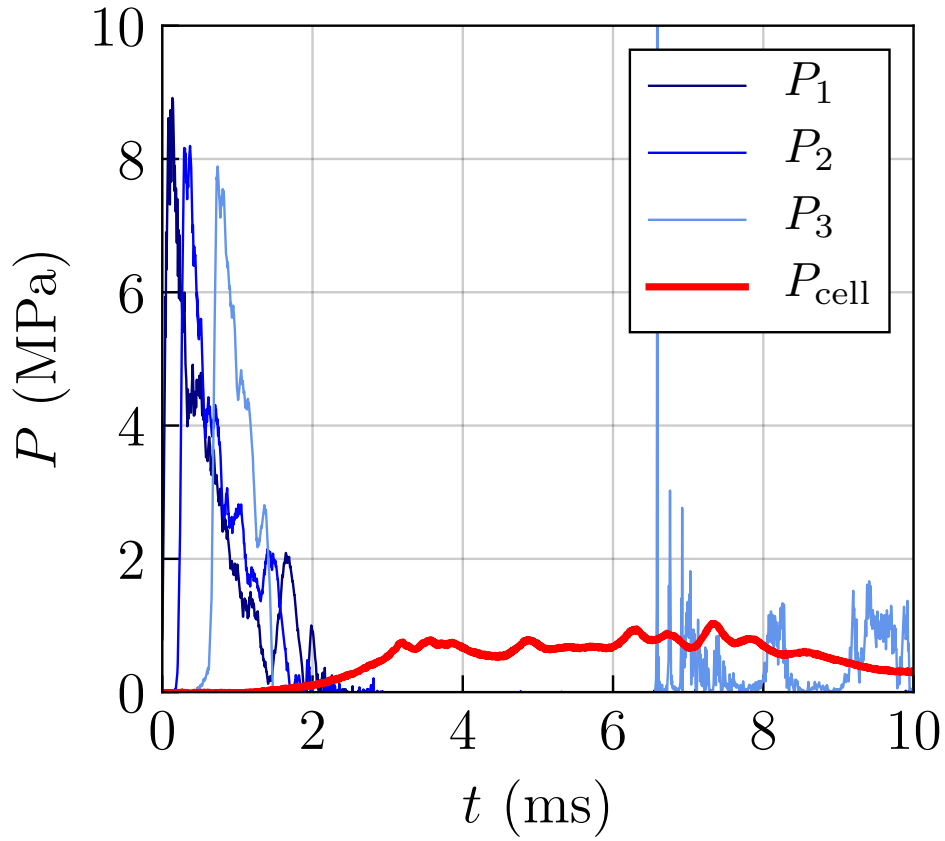

(a)

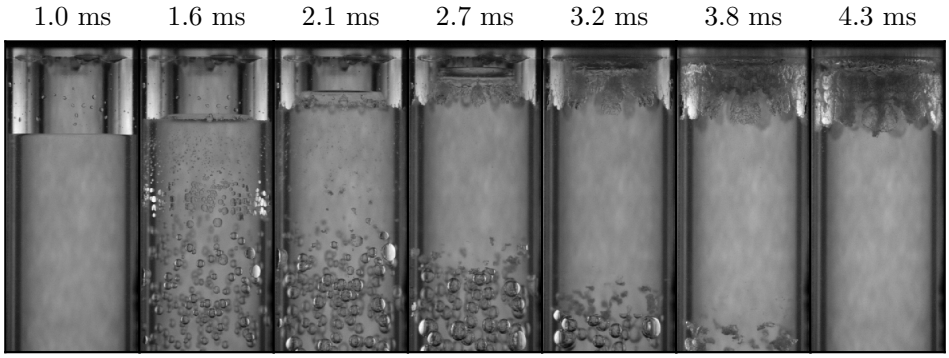

(b)

Figure 7: Experimental (a) pressure traces and (b) images of air volume and liquid-gas interface; $h_0 = 27$ mm, $v_p = 6.6$ m/s, and $\tau = 1.1$ ms is the initial compression wave arrival time at the liquid-gas interface. Test A014.

3.1 Effect of air volume height

A series of experiments were performed to determine the effect of the initial gas height, $h_0 = 3 - 50$ mm, on the compression history of the gas; the projectile velocity was between 6.5-6.7 m/s. Figure 8 shows the compression of air at two different heights, 3 ± 1 mm and 37 ± 1 mm. For an initial height of 3 mm, shown in Fig. 8a, the onset and growth of gas-liquid interface instabilities is difficult to observe but appears to be less significant than for larger heights. In contrast, for $h_0 = 37$ mm, shown in Fig. 8b, the onset of interface instabilities can be observed at 2.1 ms; the instabilities are amplified substantially prior to the liquid jets striking the top wall at 3.8 ms.

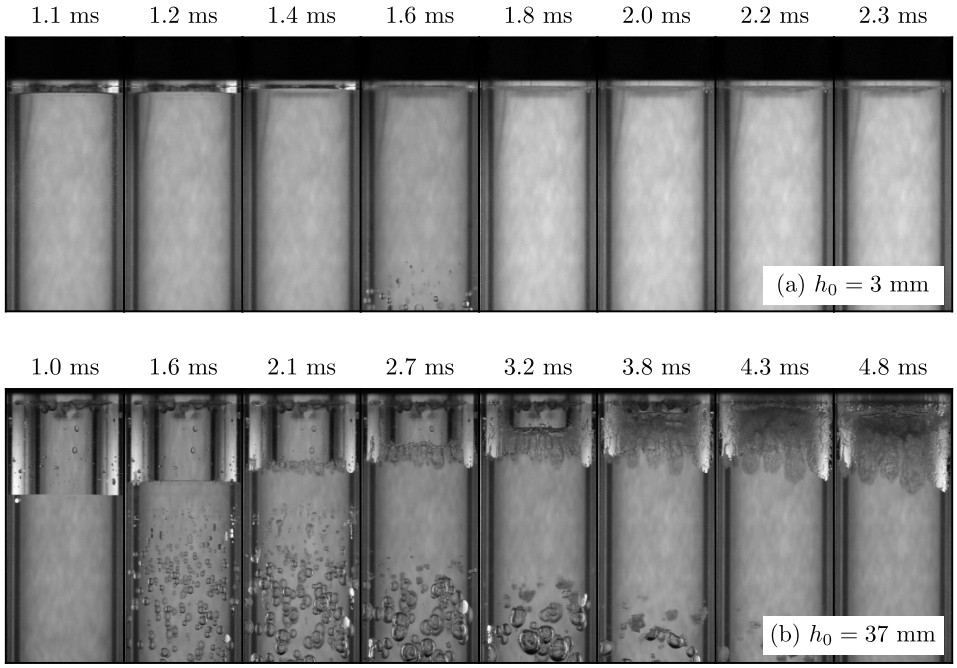

Figure 8: Images of air compression following the arrival of the primary compression wave for gas volume heights. (a) Test A024, $h_0 = 3 \pm 1$ mm, v_p = 6.61 m/s and (b) Test A011, $h_0 = 37 \pm 1$ mm, v_p = 6.5 m/s.

The corresponding pressure traces for the test cases shown in Fig. 8 are shown in Fig. 9. The peak pressures and waveforms shown in Fig. 9a are consistent with those in Fig. 7 and the measured projectile impact velocities. The overlap of the P_1 pressure profiles for the two cases demonstrates the repeatability of the impact process. For $h_0 = 37$ mm (red line in Fig. 9b) the maximum pressure reached in the gas during compression occurs at approximately 7-9 ms and is less than 1 MPa. For $h_0 = 3$ mm, the maximum pressure in the air is 15 MPa and occurs at 1.4 ms. Multiple high amplitude pressure spikes are observed in Fig. 9b for $h_0 = 3$ mm; we speculate that these correspond to the visual observations of the rapid oscillation of the air volume.

The effect of initial air volume height on the peak cell pressure is shown in Fig. 10. The line shown on the plot represents an inverse relationship between initial air volume height h_0 and peak pressure P. The inverse relationship of peak pressure and initial gas volume height is striking and intriguing. However, this eludes a simple explanation. For initial gas volume heights larger than 10 mm, this result is consistent with adiabatic compression of the gas volume and a fraction (30%) of the initial piston energy being converted to gas internal energy. The balance of the energy of the piston is apparently transferred into the liquid and the piping system. However, for gas volume initial heights less than 10 mm, much smaller fractions of the mechanical energy are converted into gas internal energy, the fraction decreases to 10% for h_0 = 3 mm. The instability of the liquid-gas surface and the cavitating flow in the liquid make it challenging to craft a first-principles explanation.

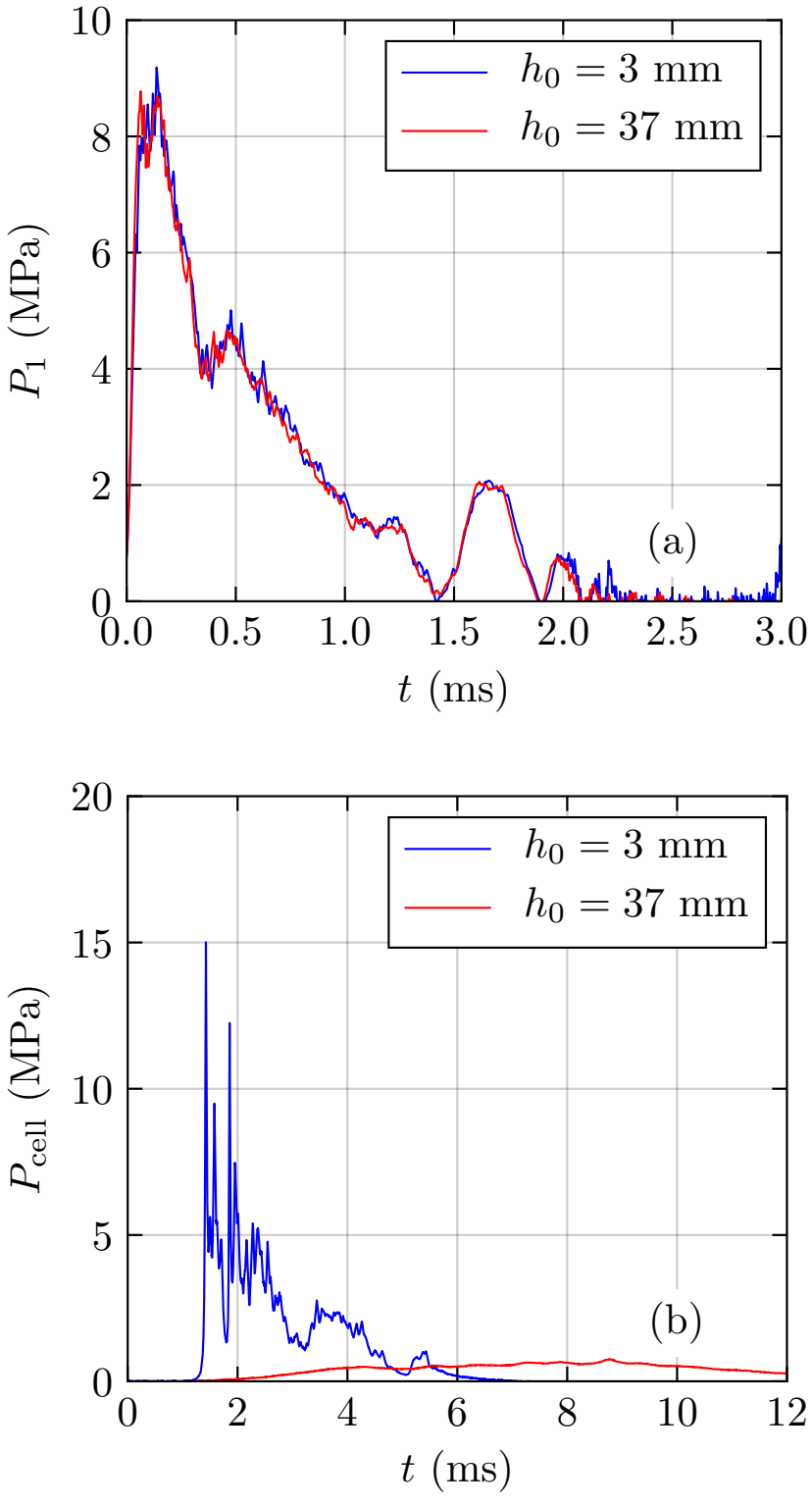

Figure 9: Pressure traces for (a) P_1 and (b) P_{cell} for the two cases shown in Fig. 8.

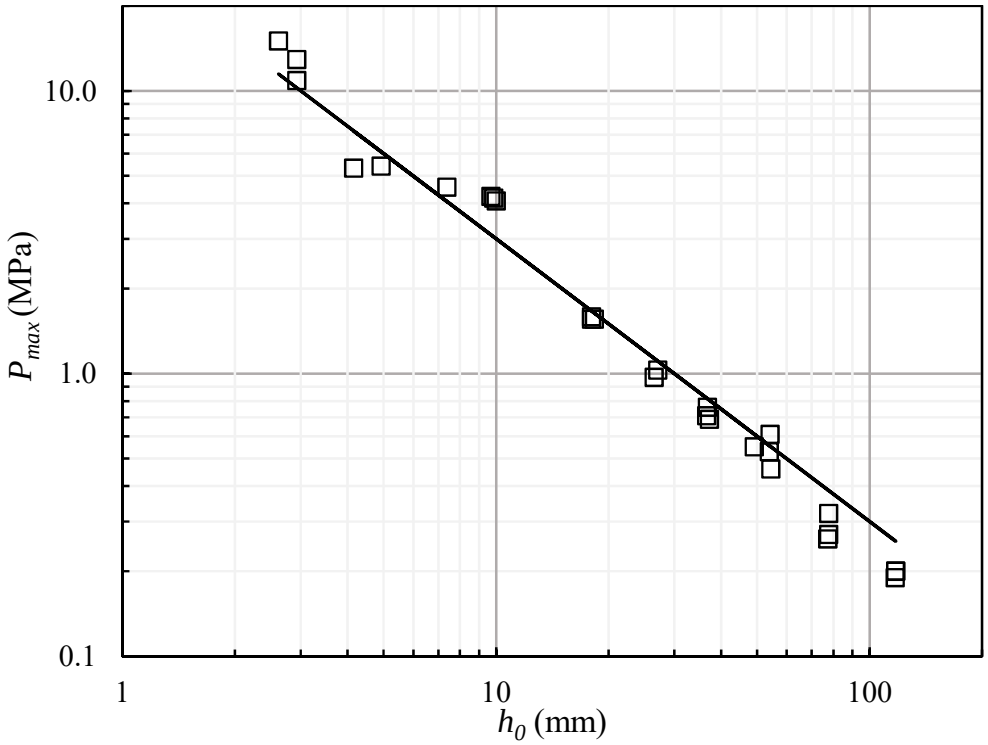

Figure 10: Experimental results of peak cell pressure as a function of initial gas height for $v_p = 6.5 - 6.7$ m/s.

3.2 Effect of projectile velocity

The relationship of projectile velocity to initial buffer velocity is shown in Fig 11a for initial air volume heights of 30 to 100 mm. On average, the buffer is initially accelerated to approximately $74 - 80\%$ of the projectile velocity and independent of the initial air volume, as expected because the projectile-buffer interaction time is much less that the round trip time of 2 ms for acoustic waves in the water. A perfectly inelastic collision between the projectile and buffer would result in a final velocity of 84% of the projectile velocity; elastic collision would result in even higher buffer velocities. The observed lower velocity is consistent with a finite time for the collision interaction between the projectile and buffer which causes an added mass effect due to the propagation of the acoustic waves into the water during the interaction time as discussed by Kojima et al. (2017). The finite interaction time is due to the wave propagation processes within the buffer and the projectile. The wave round trip times are on the order of 60 (projectile) to 200 (buffer) μs. The added mass needed to explain the observed velocity is between 0.15 and 0.3 kg, which corresponds to a water layer 75 to 150 mm thick, consistent with a 50-100 μs interaction time. The inelastic nature of the initial impact process can be seen in Fig. 4 in which it is observed that the buffer and projectile move together for the first 2.5 ms following contact.

Figure 11b shows the effect of the projectile velocity on the peak pressures P_1 and P_2 in the liquid and the peak cell pressure, P_{cell}, for $h_0 = 30$ mm. P_1 and P_2 are highly correlated with v_p and increasing linearly with the projectile velocity; the slope is consistent with an effective acoustic impedance of about $1.52 \pm 0.2 \times 10^9$ kg·m^{-2}·s^{-1}, 7% higher than the average value observed for the Case A tests with v_p = 6.5-6.7 m/s. This effective impedance is a consequence of wave interaction processes in the projectile-buffer-water interfaces during the initial impact process, and the fluid-structure interaction as discussed in Shepherd and Inaba (2010) and Kojima et al. (2017).

The close agreement between P_1 and P_2 for given projectile velocities indicates that there is only a modest (less than 10%) decay in wave amplitude between these locations. The peak cell pressure increases with increasing projectile velocity in a nonlinear fashion with significant test-to-test variation. The scatter can be attributed to multiple factors, most significantly the role of cavitation resulting from reflection of the pressure waves from the liquid-gas interface at the bottom of the test cell volume. This results in multiple, closely-spaced pressure peaks and oscillation of the gas volume, particularly at the higher impact velocities. Small variations in timing of these peaks results in substantial variation in the resulting gas peak pressures. Variations in initial gas content, impact velocity and cavitation at the buffer-water interface (Kojima et al., 2017) are also likely contributing factors to this variability.

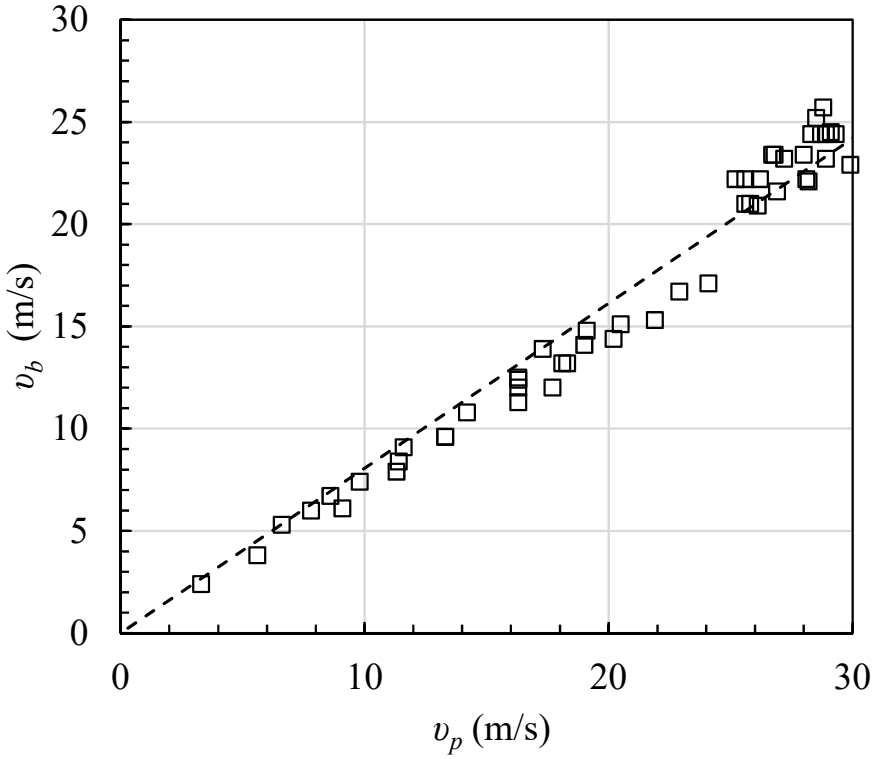

(a)

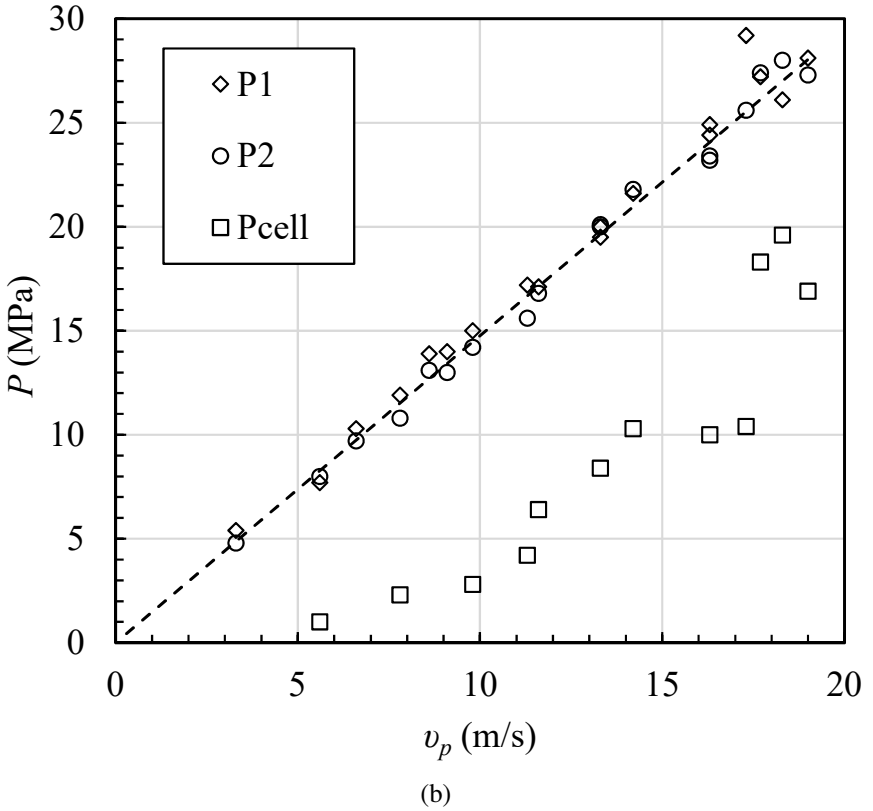

(b)

Figure 11: Experimental (a) buffer velocity as a function of projectile velocity for air volume heights of 30-100 mm; (b) peak pressure in the test cell and liquid column as a function of the buffer velocity for an initial gas volume height of 30 mm.

3.3 Suppression of interfacial instabilities

Several experiments were performed with the addition of a polypropylene disc, separating the gas from the liquid in the test cell, to suppress the interfacial instabilities (see Figs. 7b and 8b) that develop during compression of the gas volume. Example pressure traces of a disc and no disc configuration are shown in Fig. 12 for the compression of N_2 in the gas space. In both cases, the projectile velocity was approximately 29 m/s. Figure 12a shows comparable peak pressures at P_1 of $41 - 44$ MPa and similar pressure histories. Figure 12b shows the test cell reaching peak pressures of 16 MPa and 14 MPa, with and without a disc, respectively. The general trend of the gas pressure history does not appear to be significantly affected by the addition of a disc. This also confirms that the peak pressure recorded without the disc is due to the compression of the gas rather than the impact of the water jets on the pressure transducer.

Figure 13 shows the compression of the gas from 1.0-4.2 ms after arrival of the primary compression wave at P_1. Qualitatively, the rate of upward liquid column movement is not affected by the addition of a disc.

An overlay of the disc outline from Fig. 13b on the no disc images of Fig. 13a is shown in Fig. 14. The upward liquid movement occurs qualitatively at the same rate between the disc and no disc configurations until approximately 1.7 ms. At 2.0 ms, the top surface of the outer-liquid annulus begins to lag behind the disc and the inner-liquid jet structure begins to move ahead of the disc. This behavior continues until the inner jet structure impinges against the top wall at approximately 3.1 ms. At 3.1 ms, the top surface of the outer-liquid annulus and the disc have yet to reach the top wall. Figure 14 suggests that the onset of fluid instabilities in the absence of a disc results in the development of an unstable and growing, inner-liquid jet structure and outer-liquid wrinkled surface due to the interfacial instability between the liquid and gas.

3.4 Origin of interfacial instabilities

The origin of the interfacial instabilities was investigated by examining the time history of the mean interface motion. Because it is difficult to track the interface when there are instabilities, the tracking was performed in the tests carried out with the disc. The results of Fig. 12 show the pressure histories with and without the disc are sufficiently similar that we expect the mean interface motion to also be very similar. As mentioned in the Introduction, there is a potential for both Richtmyer-Meshkov and Rayleigh-Taylor instability due to the impulsive and continuous effects, respectively, of interface acceleration (Zhou, 2017). Using the data of test B044, illustrated in Figs. 12-14, the disc motion was tracked, smoothed and differentiated to obtain position, velocity and acceleration. The results are shown in Figs. 16-18. Following the impact of the pressure wave on the disc at t = 0, the disc accelerates within 0.5 ms to an upward velocity about -50 m/s with a peak acceleration of -3×10^5 m·s^{-2}. This is consistent with reflection process generating an interface velocity (3) of approximately twice the incident velocity of approximately 27 m·s^{-1}. Due to the rising pressure resulting from the compression of the gas, the disc immediately begins to decelerate until the disc comes to rest and reverses motion at about 3 ms. From 0.5 to 2 ms, the acceleration is on average about +1×10^4 m·s^{-2}, increasing to a peak value of +2×10^5 m·s^{-2} just before the direction of motion is reversed.

The initial impulsive acceleration of a non-planar interface by a pressure (shock) wave can lead to instability due to the impulse generation or deposition of vorticity at the interface by baroclinic torque, this is the Richtmyer-Meshkov mechanism (Zhou, 2017). If the interface has sinusoidal perturbations in elevation with initial wavelength λ and amplitude a_o (see Fig. 15), then at the very earliest times, the linear theory predicts and experiments show (Motl et al., 2009) that the amplitude a of the perturbation will grow linearly with time according to

$$\frac{\mathrm{d}a}{\mathrm{d}t} = kA\Delta V a_o \, . \tag{4}$$

The velocity change ΔV is due to the impulsive acceleration of the interface and A is the Atwood number

$$A = \frac{\rho_2 - \rho_1}{\rho_2 + \rho_1} \tag{5}$$

based on densities upstream (1) and downstream (2) of the interface when the shock wave is propagating from the upstream to downstream direction. The wavenumber of the interface perturbation with wavelength λ is defined as

$$k = \frac{2\pi}{\lambda} \, . \tag{6}$$

In the present case, $A \approx$ -1 for a water-gas interface and the velocity change imparted by the impulsive acceleration is ΔV. A negative value of A for positive ΔV indicates that the initial perturbation on the interface will be inverted and grow in the opposite direction to the original interface deflection from the mean level. It is important to note that the instability occurs for both positive and negative values of A and ΔV so that under impulsive acceleration all perturbed interfaces with a density difference will result in growth of the perturbations (this is not the case for continuous acceleration. In the present case, the initial interface shape is not known so even approximate values for the initial amplitude a_o and wavelength λ are unavailable. If we presume that the characteristic wavelengths are associated with capillary forces between water and air,[1] dimensional analysis gives a length scale of $\lambda \approx \sqrt{\sigma/\rho g}$ where σ is the interfacial tension between air and water, 7.5×10^{-2} N·m^{-1}, g = 9.81 m·s^{-2} is the acceleration of gravity and $\rho = 10^3$ kg·m^{-3} is the mass density of water. This gives λ = 2.76 mm and using ΔV = 50 m/s, the estimated initial growth rate is

$$\frac{1}{a_o}\frac{\mathrm{d}a}{\mathrm{d}t} = kA\Delta V \tag{7}$$

$$\approx -1.1 \times 10^5 \text{ s}^{-1} \tag{8}$$

or the characteristic time to double the disturbance amplitude is

$$\tau_{RM} = 8.8 \ \mu\text{s} \ . \tag{9}$$

About 60 doubling times elapse from the onset of the interface motion until significant deceleration of the interface at 0.5 ms suggesting that Richtmyer-Meshkov instability is a plausible mechanism of initiating the observed interfacial instabilities.

As shown on Fig. 18, following the initial acceleration of the interface the interface decelerates as the gas is being compressed. This continuous deceleration introduces the possibility of additional interfacial instability due to the continuous vorticity production at the interface by the Rayleigh-Taylor mechanism (Zhou, 2017). In this case, the linear theory of the dynamics of perturbations on the interface leads to exponential growth or decay in the perturbation amplitudes depending on the density differences and direction of the acceleration:

> "...this surface is stable or unstable according to whether the acceleration is directed from the heavier to the lighter fluid or vice versa." Taylor (1950)

Taylor's linear analysis gives the following evolution equation:

$$\frac{\mathrm{d}^2 a}{\mathrm{d}t^2} = g_i k A a \tag{10}$$

where g_i is the acceleration of the interface as measured by the motion in the same direction ($1 \rightarrow 2$) as the Atwood number is computed. Defining the interface velocity as

$$V = -\frac{\mathrm{d}h}{\mathrm{d}t} \tag{11}$$

the acceleration is

$$g_i = \frac{\mathrm{d}V}{\mathrm{d}t} = -\frac{\mathrm{d}^2 h}{\mathrm{d}t^2} \tag{12}$$

The product of g_i (< 0) and A (< 0) is positive during the period from 0.5 to 3 ms, so that the interface is Rayleigh-Taylor unstable and interface perturbations will grow in time. If the growth were linear during this time period (it is not!), then the increase in amplitude of a fixed wavelength perturbation under a constant acceleration g_i for time t will be

$$\frac{a(t)}{a_1} = \exp\left(\sqrt{kAg_i}\, t\right) \tag{13}$$

[1] The interfacial forces between polycarbonate and water are much smaller as evidenced by the contact angle of 75-82° at a water-polycarbonate-air interface

Using the same value for k as used in the Richtmyer-Meshkov estimate of growth rate and an average acceleration of $g_i = 1 \times 10^4$ m·s^{-2}, we obtain an exponential growth constant of

$$\sqrt{kAg_i} = 4.77 \times 10^3 \text{ s}^{-1} . \tag{14}$$

The characteristic e-folding times for the interface perturbations is

$$\tau_{RT} = 0.2 \text{ ms} . \tag{15}$$

About 12.5 e-folding times will elapse during 2.5 ms of the Rayleigh-Taylor instability phase.

These estimates are only correct for the linear stages of the instability and therefore only apply during the earliest stages of interface instability. These estimates do make it clear that the interface is highly unstable, consistent with the experimental observations.

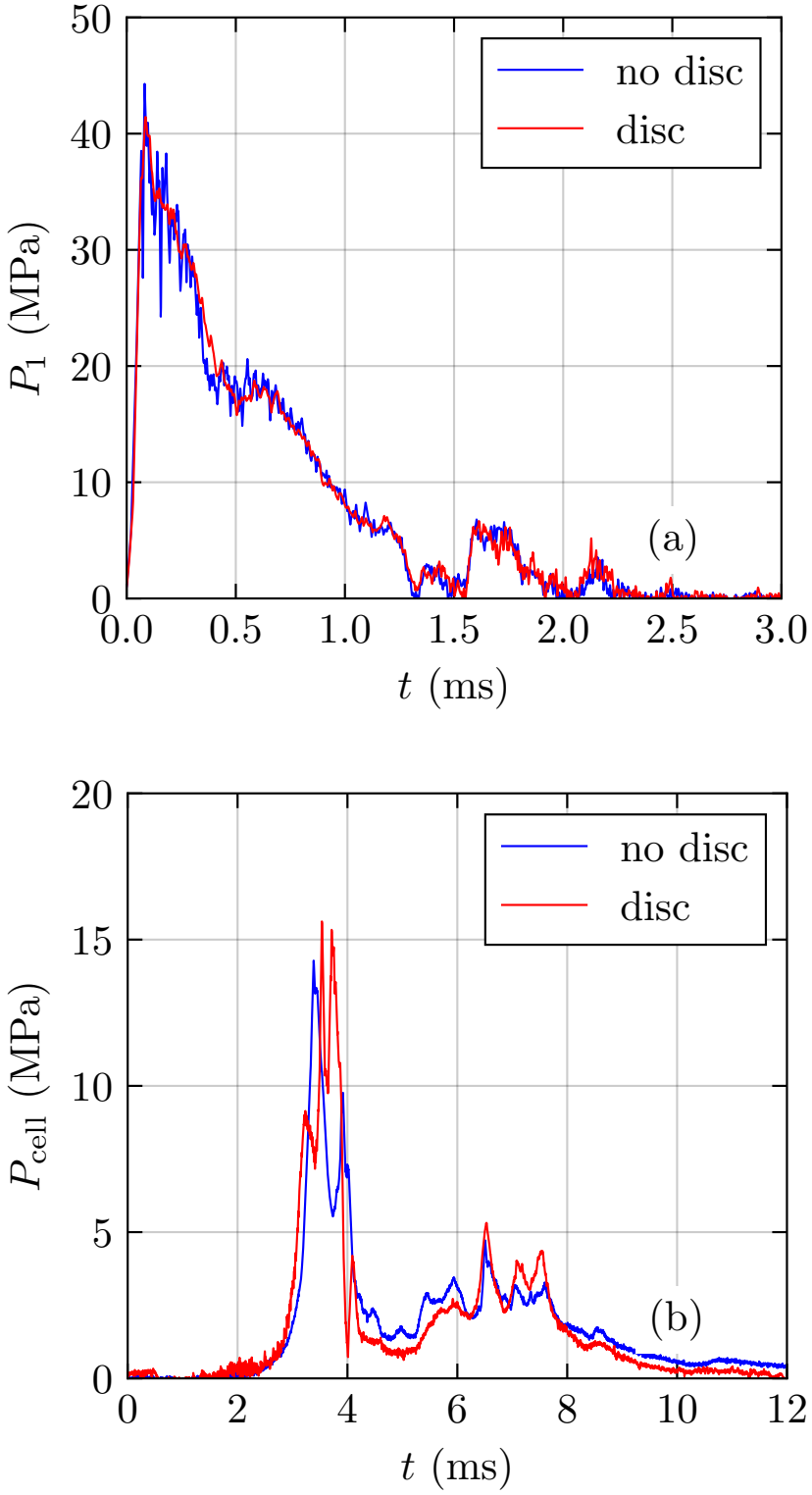

Figure 12: Pressure traces corresponding to (a) P_1 and (b) P_{cell} for $h_0 = 100 \pm 1$ mm (Test B044, v_p = 28.9 m/s, disc) and $h_0 = 103 \pm 1$ mm (Test B056, v_p = 28.8 m/s, no disc).

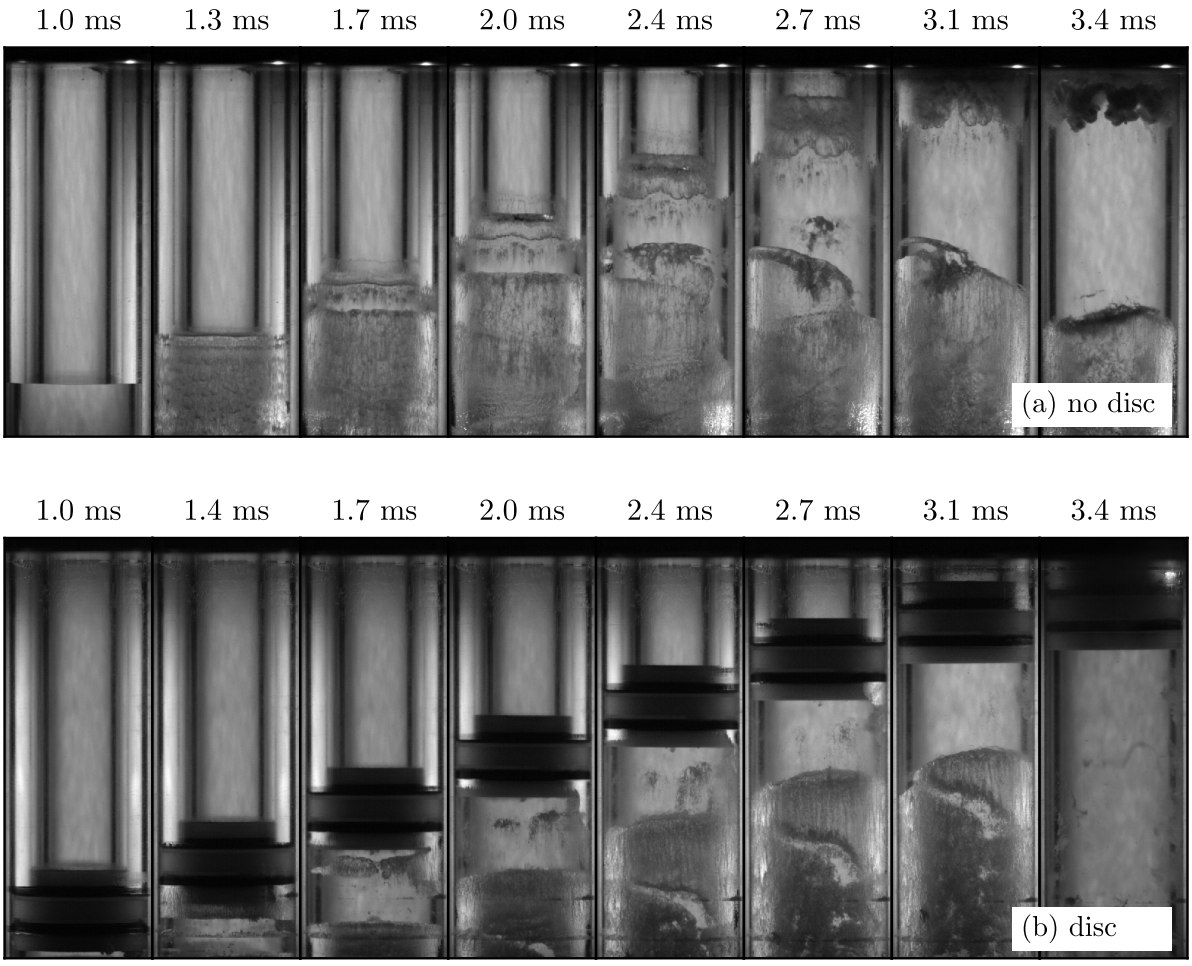

Figure 13: Images of gas compression following the arrival of the primary compression wave in the test cell (a) without and (b) with a disc. Tests are the same as in Fig. 12

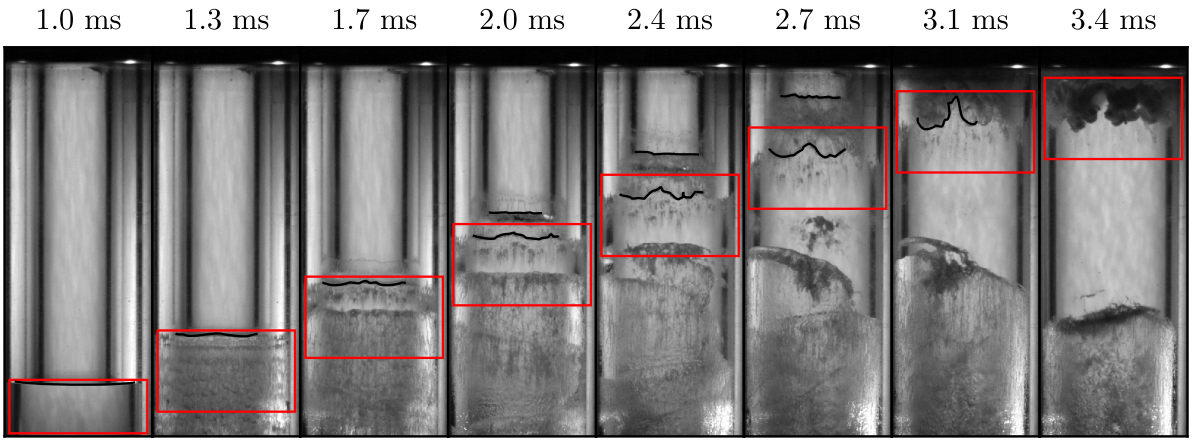

Figure 14: Overlay of disc from Fig. 13b onto Fig. 13a; the red rectangle represents the disc and the black line delineates the surface of outer-liquid annulus and inner-liquid jet structure.

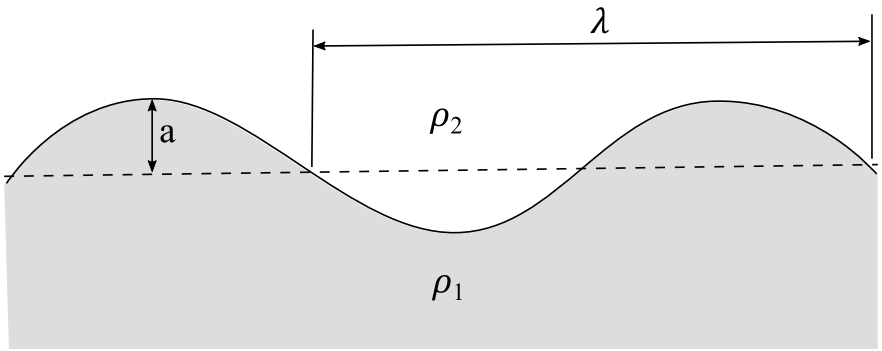

Figure 15: Schematic diagram of unstable interface with a sinusoidal perturbation of amplitude a and wavelength λ.

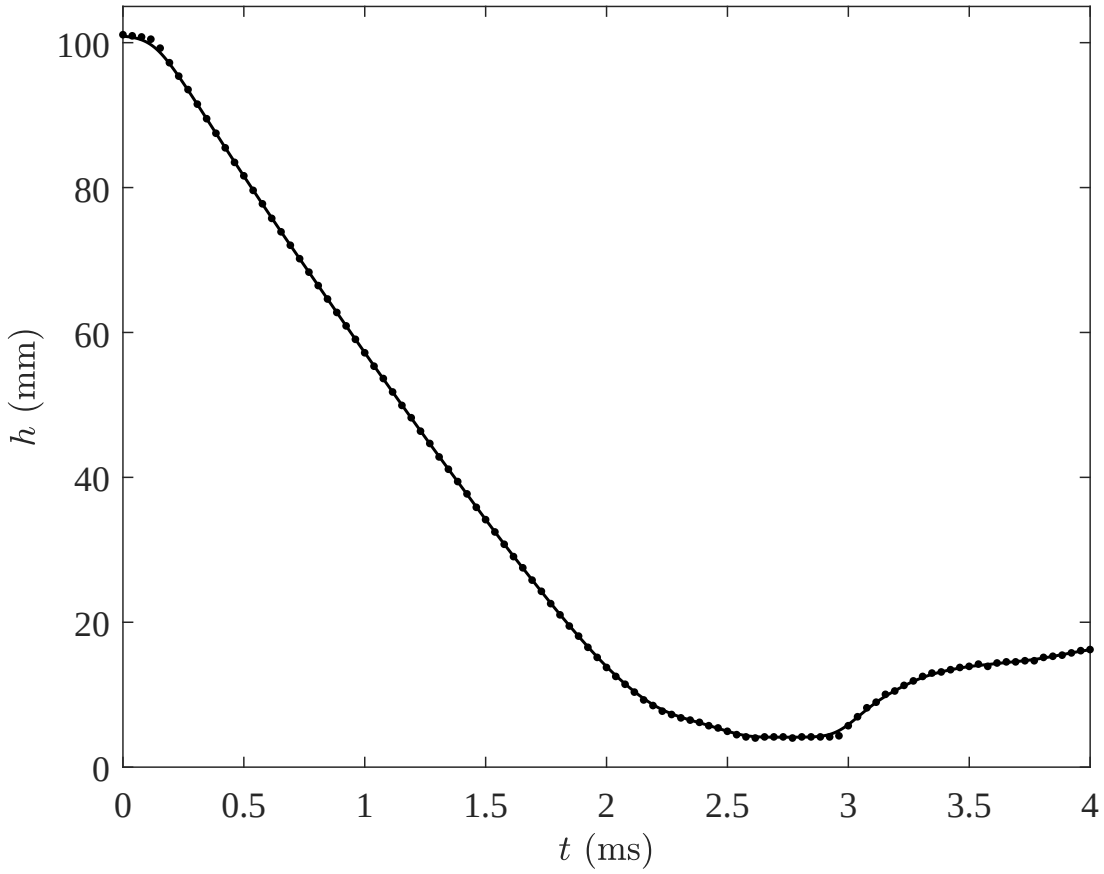

Figure 16: Height of gas volume $h(t)$ for test B044. Symbols are data from tracking the upper surface of the disc, the continuous line is a smoothed fit obtained by interpolating the original 197 data points to 6000 points using piecewise cubic Hermite interpolating polynomials and a Gaussian smoothing function over 300 points.

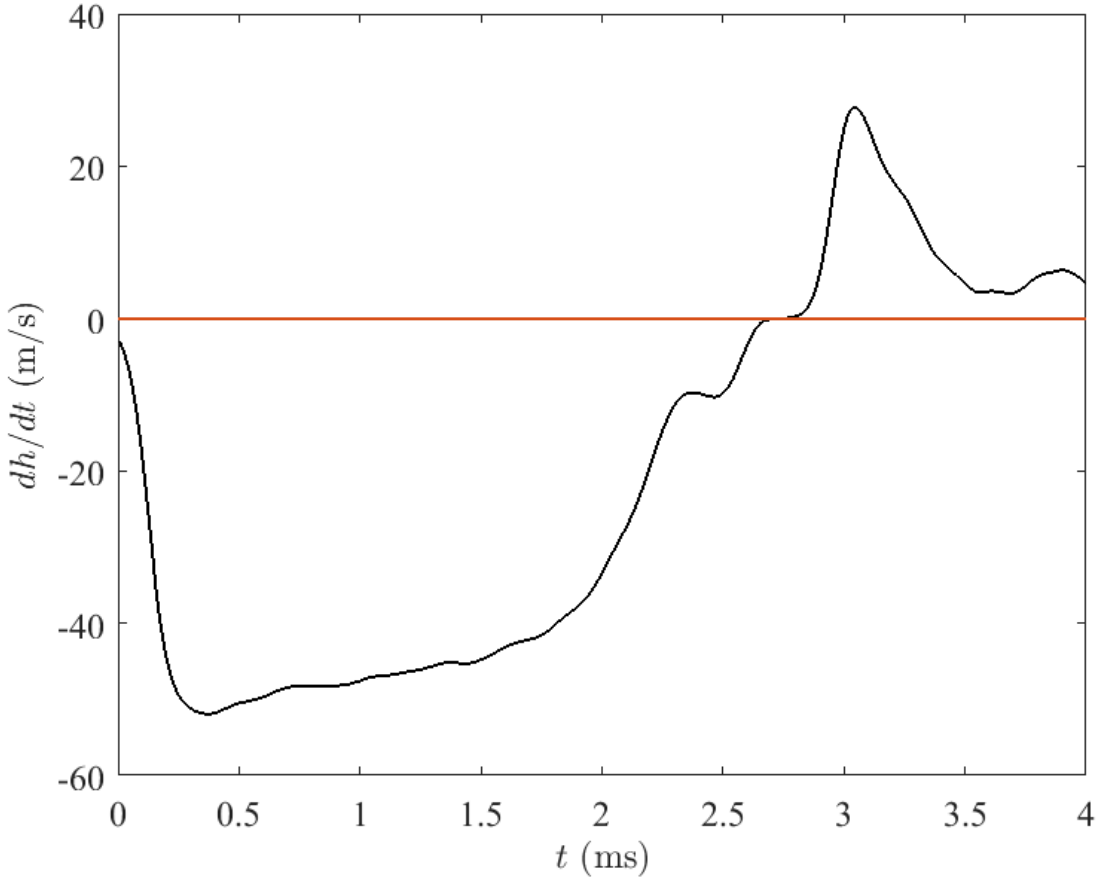

Figure 17: Derivative of the height of gas volume dh/dt for test B044. The derivative was obtained by processing the smoothed data shown in Fig. 16 using a 3rd-order Savitzky-Golay filter spanning 11 points.

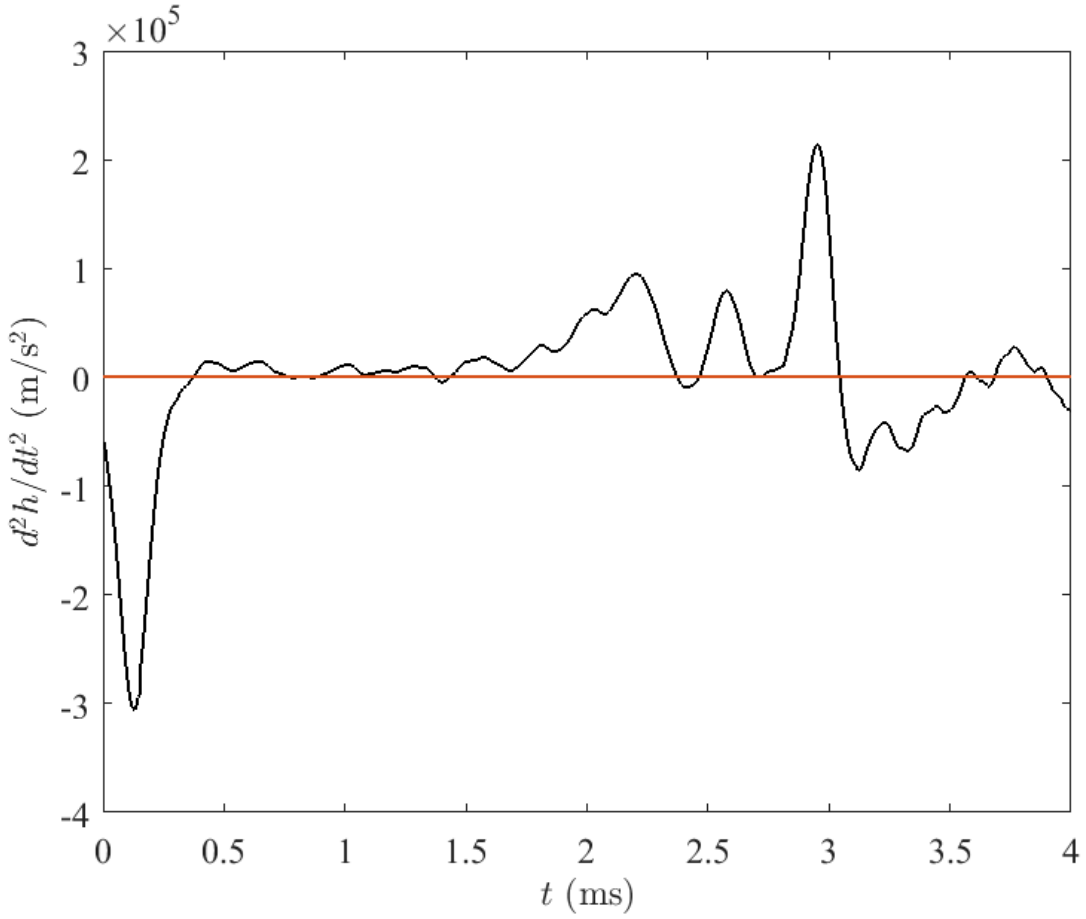

Figure 18: Acceleration of the height of gas volume d^2h/dt^2 for test B044. The second derivative was obtained by processing the smoothed data shown in Fig. 16 using a the same 3rd-order Savitzky-Golay filter spanning 11 points that was used to obtain the derivative shown in Fig. 17.

4 Estimating ignition thresholds

Previous studies in RCMs or free-piston compressors (Das et al., 2012, Lee and Hochgreb, 1998, Cain, 1997) have shown that explosive ignition of H_2-O_2 mixtures will be possible if temperatures of 950 to 1050 K can be obtained during compression and sustained sufficiently long for the chemical reactions to proceed to completion. In the present studies, the gas only remains compressed for a short time (1-5 ms) before the dynamics of the water hammer result in expansion. So there were two key issues that we had to address prior to performing experiments with reactive mixtures. First, we needed to determine if we could achieve sufficient compression to reach the necessary temperatures for ignition. Second, we needed to determine the effect on ignition of the rapid expansion following compression.

The first issue was addressed by estimating ignition time as a function of compression ratio (to account for the increase in both temperature and pressure). These estimates were done using constant volume explosion computations with a detailed chemical reaction mechanism that was validated against RCM data. These computations did not include the expansion phase of the present experiments and only addressed the issue of compression ratio. These computations predicted that a compression ratio (ratio of initial to final or minimum volume, $CR = V_0/V_{\text{min}} = h_0/h_{\text{min}}$) between 20 and 30 would result in sufficiently high temperatures so that the mixtures would ignite with a delay time of between 3.5 and 0.13 ms, respectively. Equivalently, the peak test cell pressure will have to be between 20 and 30 MPa if the initial pressure is one atmosphere in the test cell. The implications for our conditions are twofold. First, in our geometry, in order for combustion to propagate and be observable, the final gas height after maximum compression, h_{min}, should be on the order of 2-3 mm which means that the initial height, h_0, should be on the order of 50 to 100 mm. Second, the impact speed must be on the order of 15-30 m/s to achieve these compression ratios.

The second issue was the effect of the rapid expansion immediately following compression as observed in the nonreactive tests, e.g., Fig. 12. The key question to be addressed is the quenching effect of the rapid expansion. Previous work (Eckett et al., 2000, Radulescu and Maxwell, 2010, Maxwell and Radulescu, 2011, Mével et al., 2019) on rapid expansion following adiabatic compression has revealed that there is a critical decay rate for quenching. If the rate of change of volume exceeds a critical value then the reaction will be quenched. We expect that this will be the case when the compression pulse width is less than a critical value.

To address the second issue, a simple model of the type used to model RCM operation was used to simulate the compression and ignition of the gas volume between the water and the closed end. The model consists of an adiabatic, zero-dimensional, time-dependent energy (Eq. 16) and species equations (Eq. 17) with detailed chemical kinetics modeled with the open-source chemical kinetics software, Cantera (Goodwin et al., 2014). For a fixed mass of gas in the test cell with spatially uniform but time-varying thermodynamic state, a control volume analysis gives the following governing equations.

$$\frac{\mathrm{d}T}{\mathrm{d}t} = -\frac{1}{c_v}\left(\sum_i e_i \frac{\mathrm{d}Y_i}{\mathrm{d}t} + \frac{RT}{V}\frac{\mathrm{d}V}{\mathrm{d}t}\right) \quad \text{and} \quad P = \rho RT \tag{16}$$

$$\frac{\mathrm{d}Y_i}{\mathrm{d}t} = \frac{W_i \dot{\omega}_i}{\rho} \tag{17}$$

In Eqs. 16 and 17, T, P, V, and ρ are the temperature, pressure, volume, and mass density of the gas, respectively, c_v is the specific heat at constant volume, e_i, $\dot{\omega}_i$, and Y_i are the mass-specific internal energies, net molar generation rate per unit volume, and mass fraction of species i, respectively, and R is the gas constant for the mixture.

This model corresponds to treating the compressed gas as homogeneous, neglecting the heat loss to the walls and piston as well as other nonideal features such as multidimensional flow into any gaps or cervices within the test chamber. These are well-known issues (Goldsborough et al., 2017) and can lead to significant discrepancies between simulated and measured ignition delay time, particularly for hydrocarbon fuels at low temperatures. For our application to hydrogen at moderate to high temperatures, the validation study results discussed below indicate that the simplified model gives reasonable results. A detailed examination of the concept of critical decay rate and an in-depth discussion of the combustion chemistry aspects are reported in Shepherd (2019).

4.1 Reaction mechanism validation

Before applying the model to estimate the ignition delay time and critical pressure pulse width, a chemical reaction mechanism and associated rate constants must be selected. To accomplish this, several detailed chemical kinetic mechanisms were tested and compared against existing ignition delay time, τ, data for stoichiometric H_2-O_2-N_2-H_2O

mixtures obtained by Das et al. (2012) using a RCM. Das et al. (2012) provides experimental data of volume as a function of time for each test; the data serve as input into Eq. 16. The mechanisms evaluated were GRI-Mech 3.0 (Smith et al., 1999), Mével et al. (2009), Mével et al. (2011), Hong et al. (2011), Kéromnès et al. (2013), and the San Diego mechanism (SAN, 2016).

Figure 19 shows the experimental ignition delay times obtained by Das et al. (2012) and accompanying calculations using the Hong 2011 and Kéromnès 2013 mechanisms. Qualitatively, Fig. 19a indicates that the ignition delay time decreases with increasing pressure and Fig. 19b indicates that the ignition delay time decreases with increasing H_2O content. These results are consistent with the dominance of the HO_2 and H_2O_2 reaction pathways during the induction phase of the explosion as discussed by Lee and Hochgreb (1998), which we confirmed by examination of the species histories and reaction pathway analysis. Addition of H_2O decreases the reaction time at a fixed temperature due to the enhanced effectiveness of H_2O as a third body in the dissociation reaction $H_2O_2 + M \longrightarrow 2OH + M$ as discussed by Das et al. (2012).

The performance of each mechanism was evaluated across all the conditions tested experimentally by Das et al. (2012). The error, ε_τ, and mean error, $\bar{\varepsilon}_\tau$ are given by,

$$\varepsilon_\tau = \frac{\tau - \tau_{\text{exp}}}{\tau_{\text{exp}}} \text{ and } \bar{\varepsilon}_\tau = \frac{1}{N}\sum \varepsilon_\tau \tag{18}$$

where τ and τ_{exp} are the calculated and experimental ignition delay times, respectively. The mean error was calculated for a fixed pressure, H_2O content, and mechanism; the results are shown in Fig. 20. Qualitatively, GRI-Mech 3.0, Mével 2011, and San Diego mechanisms are not appropriate for use in the present study since their respective mean errors exceed 100% across all conditions evaluated. Hong 2011 has on average a lower mean error than Mével 2009 and Kéromnès 2013. Based on a mean error performance evaluation, Hong 2011 was chosen as the appropriate chemical kinetic mechanism for use in the present study.

4.2 Critical pulse width

Using the Hong et al. (2011) reaction mechanism, we have estimated the critical pulse width for ignition as a function of the compression ratio. The temperature, pressure and species history in the compressed gas volume were simulated using Eqs. 16 and 17. In these simulations, we used a Gaussian pulse for $V(t)$ that mimics both the rapid compression and expansion phases observed in water hammer testing.

$$\frac{V(t)}{V_o} = \left(1 - \frac{1}{CR}\right)\left[\frac{1 - \exp(-(t-t_m)^2/\tau_v^2)}{1 - \exp(-t_m^2/\tau_v^2)}\right] + \frac{1}{CR} \tag{19}$$

where t_m is the time to reach minimum gas volume and τ_v is the volume pulse width parameter. For computational purposes, t_m is chosen to be a multiple of τ_v so that V is sufficiently close to V_o at t = 0. In practice a value of t_m = $3\tau_v$ is adequately large. The total duration of a numerical simulation for the purpose of determining critical pulse length was selected to be $6\tau_v$ after a series of trial computations. The time derivative of the volume required as input to the energy equation can be computed analytically.

The critical pulse width parameter τ_v^* that separates ignition vs. nonignition cases was determined numerically as a function of CR through an iterative search. The uncompressed gas was initialized as a stoichiometric H_2-O_2 mixture at a temperature and pressure of 298.15 K and 101.325 kPa, respectively. Figure 21a illustrates the pressure-time history for a near-critical ($\tau_v \sim \tau_v^*$) ignition case and a subcritical ($\tau_v < \tau_v^*$) nonignition case with CR = 28, which results in a peak temperature of 1055 K and pressure of 10 MPa. This example shows the characteristic feature of all near-critical cases, ignition occurs after the compression peak and during the expansion phase of the volume.

Figure 21b illustrates the variation of adiabatic constant-volume explosion time τ_i^* and critical value of τ_v^* as a function of CR. The red-shaded region indicates the combinations of CR and τ_v^* that are predicted to result in ignition. Of course, this model completely neglects the effect of heat transfer to the facility and more importantly, the water, which we anticipate will have a very significant effect on ignition. Because of the simplified nature of the model, the results represent a lower bound on the compression ratios needed for ignition. The constant volume explosion time τ_i^* is approximately a factor of 10 smaller than the critical value of τ_v^* over the entire range of compression ratios studied.

A naive explosion criterion is that τ_v must be greater than τ_i^*; referring to Fig. 21b, for τ_v = 3 ms we find that this will be satisfied for $CR > 20$. A more realistic criterion is that τ_v must be greater than τ_v^*; referring to Fig. 21b, for τ_v = 3 ms we find that this will be satisfied for $CR > 26$. In our experiments, it is challenging to accurately measure

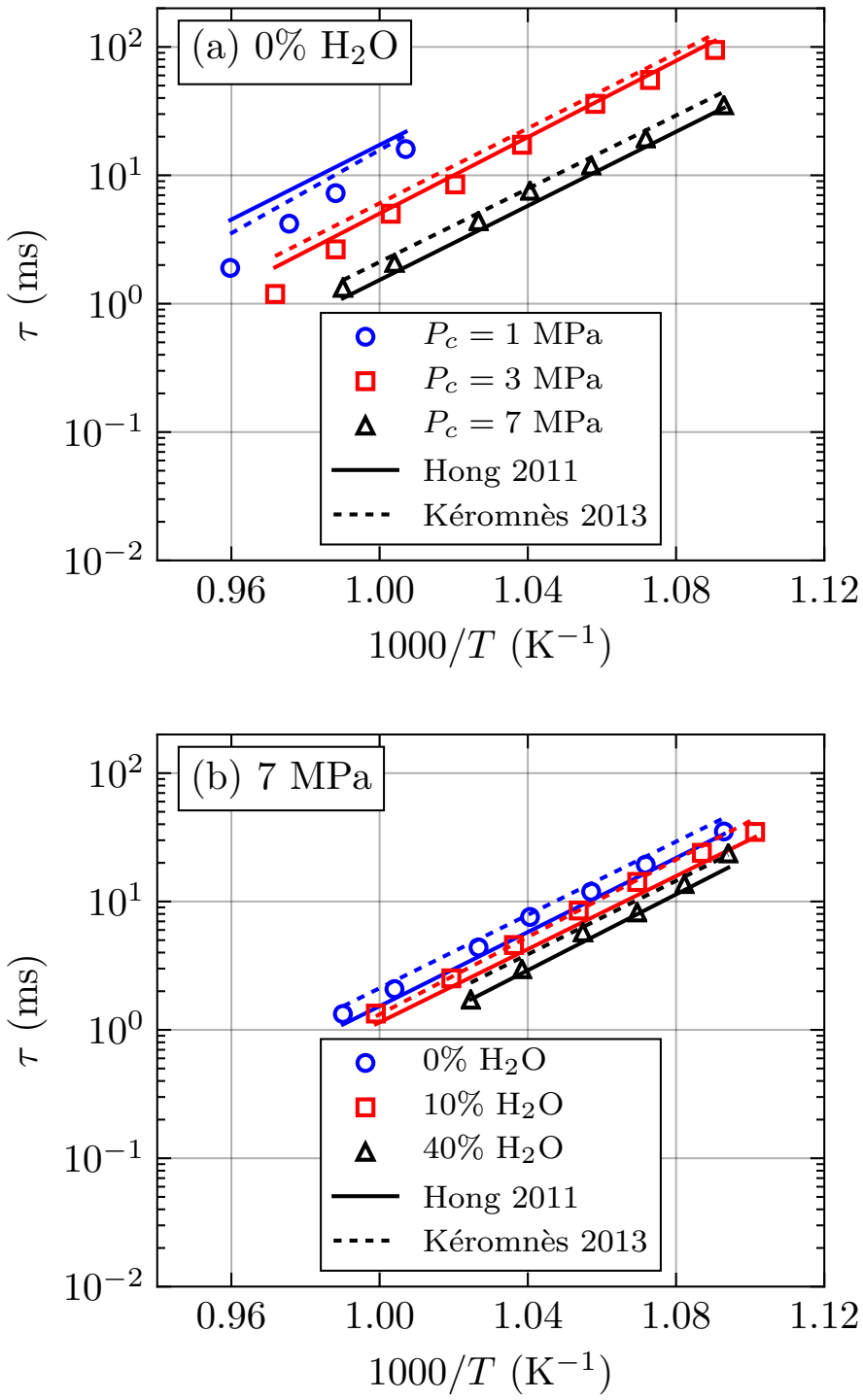

Figure 19: Experimental (Das et al., 2012) and calculated ignition delay times for stoichiometric H_2-N_2-O_2: (a) with 0% H_2O by volume and at (b) 7 MPa.

V/V_o for high compression ratios (CR = 30-50) needed for ignition so it is more reliable to use the measured P/P_o in evaluating the compression achieved in a test. In order to evaluate if a pressure pulse could result in ignition we need

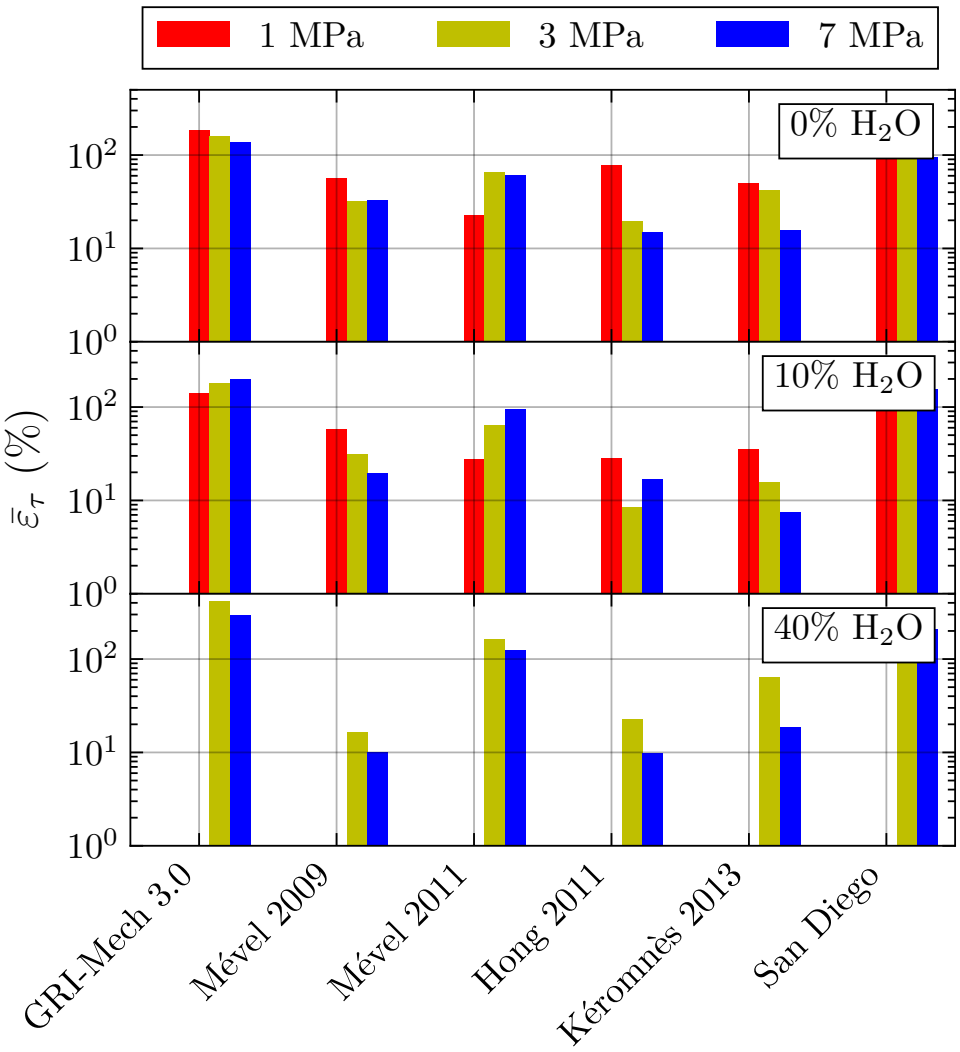

Figure 20: Mean error of predicted ignition delay times for the Das et al. (2012) experiments. Results for each mechanism at initial pressures of 1 MPa, 3 MPa, and 7 MPa, and mixture H_2O content of 0%, 10%, and 40% by volume.

to determine how the pressure pulse characteristic width is related to the volume pulse width parameter τ_v. We define $\tau_{p,1/2}$ to be the half-width of the pressure pulse measured at a pressure that is one-half of the peak value. Assuming that the pressure pulse is related to the volume pulse by isentropic compression, an approximate analytical relationship can be obtained (Shepherd, 2019) by using the perfect gas isentrope PV^γ = constant with a fixed value for the ratio of specific heat $\gamma \approx 1.4$ for gas mixtures in our experiments.

$$\tau_{p,1/2} \approx \left(\frac{2^{1/\gamma} - 1}{CR - 1} \right)^{1/2} \tau_v \ . \tag{20}$$

For a nominal value of $\gamma = 1.4$ and a compression ratio of 15, this is numerically

$$\tau_{p,1/2} \approx 0.20 \tau_v \ . \tag{21}$$

The constant of proportionality decreases with increasing CR and at CR = 60

$$\tau_{p,1/2} \approx 0.10\tau_v \ . \tag{22}$$

The critical values of the pressure pulse half-width $\tau^*_{p,1/2}$ will therefore be smaller than the critical values of the volume pulse width parameter τ^*_v by as much as a factor of 10. The role of critical pressure pulse characteristics in determining ignition thresholds is considered further in Section 5.3.

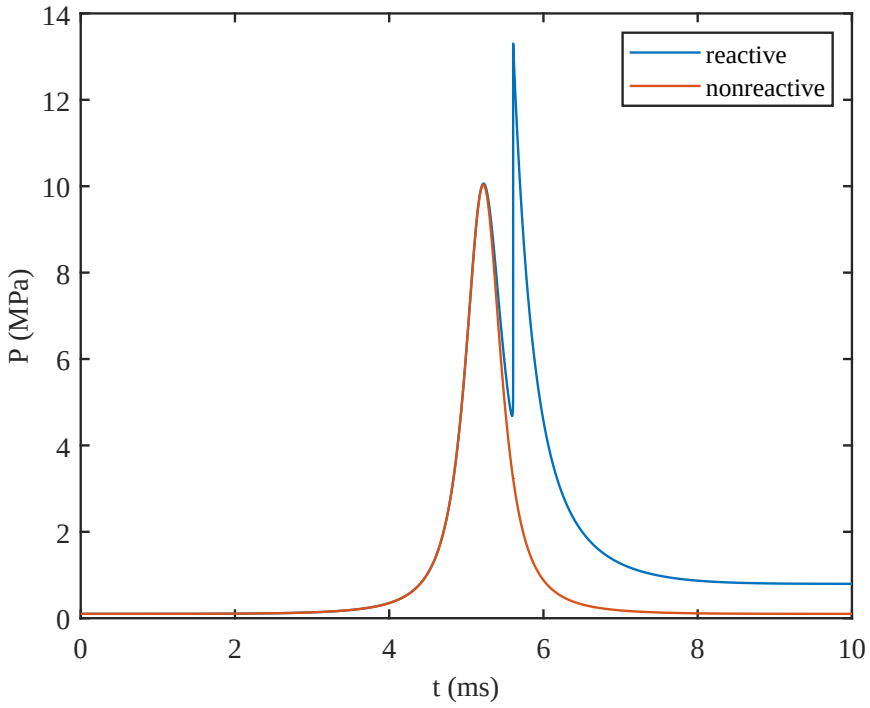

(a)

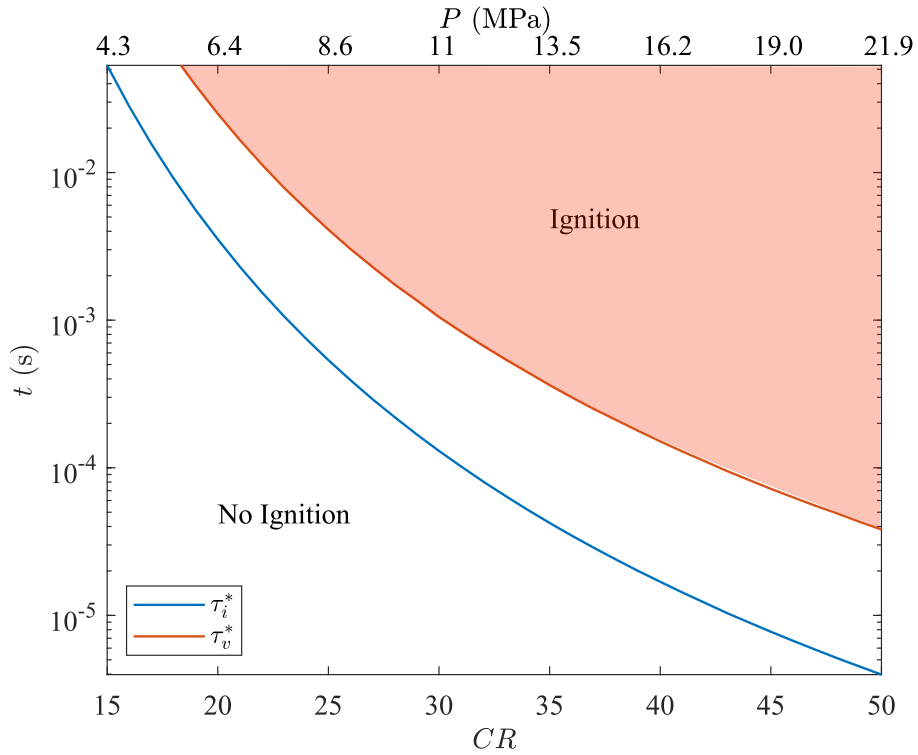

(b)

Figure 21: (a) Example of ignition close to the critical value of τ_v^* = 1.7 ms for CR = 28. (b) Critical pulse width parameter τ_v^* and adiabatic ignition time τ_i^*. The Gaussian volume pulse will initiate explosions if the pulse width parameter and compression ratio lie within the red-shaded region.

5 Reactive gas volume Results

A total of 32 tests, 18 with and 14 without a plastic disc at the gas-liquid interface were performed with stoichiometric hydrogen-oxygen mixtures. In several experiments, the mixture was diluted with nitrogen. Based on the experimental results obtained with air, the targeted nominal height for the reactive gas volume was 100 ± 3 mm. At this height, 7 tests were carried out with air (4 without a disc, 3 with a disc) to serve as a baseline. Conditions and key results for the tests are tabulated in Appendix B and an extensive set of plots is given in Appendix C.

Goals of these tests were to determine the ignition thresholds and characteristics of the resulting combustion events. There were two main issues to be addressed: a) the influence of the short compression pulse duration; b) the influence of the liquid-gas interface instability.

Comparison of the observed gas pressure pulse widths (Fig. 12) with the computed critical pulse widths (Fig. 21b) indicates that the quenching effect of the short pulses is a possibility. It is also clear from the visualization studies with nonreactive mixtures that the observed instability of the liquid-gas interface had the potential to significantly disrupt the initiation and progress of combustion due to the enhanced interfacial area and dispersion of water droplets into the gas phase. This could inhibit ignition, reduce the probability of ignition, result in partial burning of the mixture, and/or reduce the peak pressures and temperatures reached when ignition takes place.

In order to separate the potential interfacial instability effects from the possible quenching effects due to the short duration of the compression events, we completely suppressed the interfacial instability with the plastic disc. As shown in the previous nonreactive tests, Fig. 12, the pressure-time history in the gas is very similar with and without the disc, enabling an evaluation of the ignition thresholds without the potential confounding effects of interfacial instability. The tests with a disc will serve as a benchmark for comparison to no-disc tests and enable determination of the effects of interfacial instability.

5.1 Tests with a disc

The experiments reported in this subsection were performed with the 24 mm thick polypropylene disc between the gas and liquid, as shown in Fig. 2c. The disc is rigid and sealed with O-rings so that it acts like a piston to compress the gas and prevent water and gas from mixing. An example of the volume (measured by tracking the top surface of the disc in each image) as a function of time and the resulting measured and computed pressure (using the volume and isentropic relationship) are shown in Figure 22. The disc accelerates within 0.1 ms after the arrival of the pressure wave to an upward velocity of about 50 m/s which then decreases to zero at 3 ms, followed by a reversal of direction and acceleration of the disc downward. The initial deceleration of the disc is due to multiple factors, the triangular applied pressure from the liquid, the cavitation following wave reflection and the increase in gas pressure due to compression. The magnitude of the deceleration (estimated from numerical differentiation of $h(t)$) ranges from 7×10^3 m·s^{-2} at the start of the disc motion to 6×10^4 m·s^{-2} just before the minimum volume. We speculate that comparable velocity and acceleration histories occur in the tests without a disc but it was not possible to verify this quantitatively because we were unable to make sufficiently accurate measurements of the gas-liquid interface due to cavitation and instability. Irrespective of the actual magnitude, the sign of the interface acceleration during the compression phase of the no-disc cases is directed from the gas into the water; from the light into the heavy fluid, which is the criteria for Rayleigh-Taylor instability of the interface.

The computed pressure inferred from the volume is in general agreement with the measured pressure but misses the narrow pressure peaks between 2.5 and 3 ms as well as subsequent pressure peaks. This is due to difficulty in tracking the disc motion and accurately determining the gas volume near the minimum gas height (less than 6 mm). Examination of the individual frames of the video images of the test cell reveals that for high impact velocities, the peak pressure in the water beneath the disc was sufficiently high that the O-ring seals allowed water into the gas volume in some cases. The motion of the fixture due to the compliance of the supports was also a factor in some cases.

Multiple tests were performed with a reactive gas mixture. Three dilution levels were investigated: X_{N_2} = {0, 0.25, 0.50}, where X_{N_2} is the mole fraction of nitrogen; these dilution levels correspond to gas compositions of $2H_2 + O_2$, $2H_2 + O_2 + N_2$ and $2H_2 + O_2 + 3N_2$ respectively. The impact velocity of the projectile on the buffer was varied between 25.0 and 30.0 m/s, resulting in the production of a primary compression wave with amplitudes of 36.5 to 46.0 MPa in the liquid. In a non-reacting case this results in a peak cell pressure of 9.5 to 27.0 MPa. The modeling results obtained in Sec. 4 suggest the peak cell pressure is sufficiently large for ignition to occur if maintained for a sufficiently long time.

The results of the experiments performed with the disc are summarized in Fig. 23. The peak pressure on transducers

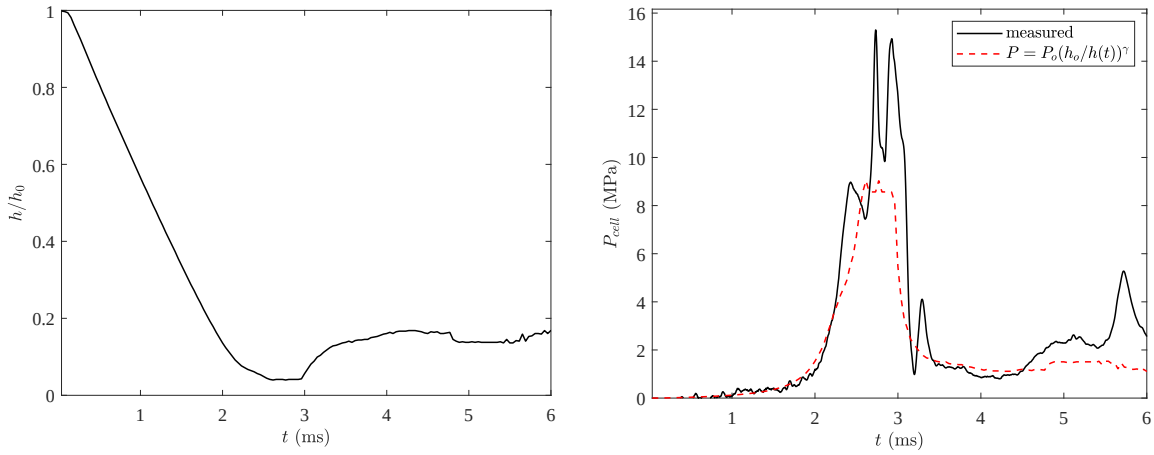

(a) (b)

Figure 22: Test B044 test cell volume (a) and pressure (b) histories. Air in test cell, h_0 = 102.2 mm and v_p = 28.9 m/s. The measured pressure history is compared with an estimate based on the measured volume and isentropic compression using γ =1.4.

P_1 and P_2 as well as the maximum pressure in the cell are shown as a function of the impact velocity of the projectile on the buffer. The symbols are coded according to the outcome of the compression event. The peak pressure and the luminosity of the combustion event were used to determine if ignition occurred.

Ignition was observed in 10 cases, 3 with X_{N_2} = 0.25 and 7 with X_{N_2} = 0. The ignition threshold appeared to be at v_p = 26 m/s corresponding to a peak gas pressure of 10 MPa. Ignition was not observed in the four tests with X_{N_2} = 0.5 and one low pressure (P_{cell} = 10 MPa) test with X_{N_2} = 0.25. In the ignition cases (red-filled markers in Fig. 23), the measured peak pressure in the cell is up to 4 times larger than for a non-reacting case and in 4 cases, comparable to or greater than the peak pressure in the initial liquid pressure wave.

We suspect that the actual peak pressures in the cell are larger than the peak pressure reported by the transducer: the pressure peaks resulting from the ignition events had an extremely short duration, and were likely not fully resolved in time. Furthermore, the O-ring used to create a seal between the cell and the top flange was not rated for such large pressures; there is evidence which suggests the cell leaks upon ignition. In some cases we observed a high velocity jet of hot steam exhaust leaking through a gap created between the top flange and the test cell body.

An example of an ignition event is Test B060 with a projectile impact velocity v_p = 26.8 m/s and undiluted stoichiometric mixture (h_0 = 100.1 mm) in the test cell. Analysis of the buffer video indicated contact between the projectile and buffer surfaces for approximately 2.5 ms, after which separation occurs. The pressure recorded in the straight section of the pipe located below the buffer (i.e., P_1 and P_2) and the pressure in the test cell (P_{cell}) are shown in Fig. 24 along with an inset of P_{cell} showing the variation immediately before and after ignition. Note that the pressure data from in the cell transducer is raw (unfiltered) in order display the sharp peak observed at ignition. The pressure in the cell is 10.0 MPa immediately before ignition, and has a peak value of 49.4 MPa immediately after ignition. Note that upon ignition the pressure rapidly increases to its peak value in less than 1 μs, similar to the response time of the pressure transducer. This suggests the pressure measurement in the cell could be temporally under-resolved. The rapid increase in pressure in the cell is followed by an equally rapid decay. A few milliseconds after the ignition event the pressure appears to become negative; this is an artifact due to thermal strains produced in the diaphragm of the sensor by the high temperature combustion products.

Figure 25 contains a sequence of images showing the test cell and the plastic disc for a short time before and after the ignition event. The times indicated are relative to the trigger event ($t = 0$). The first 6 images (1.015 ms to 3.399 ms) correspond to the upward motion of the plastic disc. The ignition event is observed at 3.399 ms. The remainder of the frames correspond to the downward motion of the plastic disc (i.e., relaxation of the pressure in the gas volume). The ignition and combustion of the reactive mixture create a substantial amount of chemiluminescence which saturates the sensor of the high-speed camera. Chemiluminescence is visible up to 6.0 ms after the ignition event.

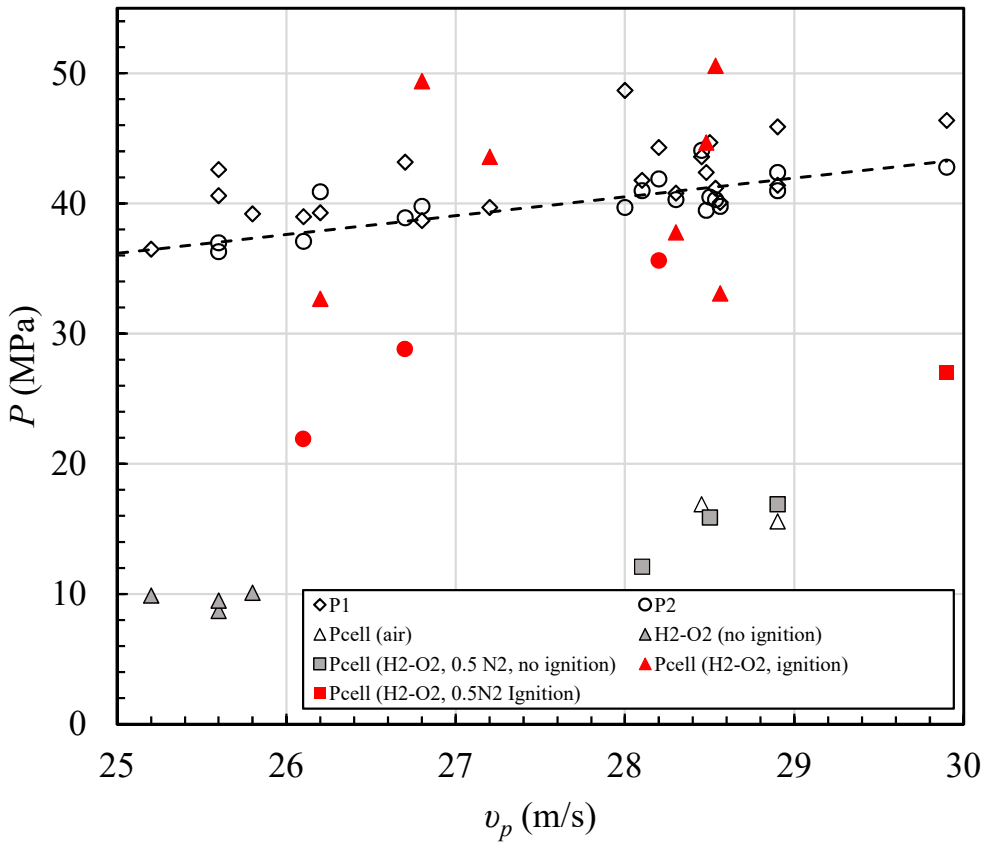

Figure 23: Disc configuration peak pressure and ignition results as a function of projectile velocity for stoichiometric ($2H_2$-O_2) mixtures with three N_2 dilution levels. The red filled circles are for a dilution level of X_{N_2} = 0.25, the gray-filled squares are for X_{N_2} = 0.5 and the red-filled triangles are undiluted mixtures, X_{N_2} = 0, the open triangles were nonreactive (air) mixtures.

Figure 26 contains a sequence of images for test B065. The experimental conditions of test B065 are very similar to those of test B060, but the exposure time of the camera was reduced to 0.38 μs; this is an exposure which is 24 times smaller than the exposure used in test B060. The frame rate of the high-speed camera was also increased. Accordingly, the field of view had to be reduced. The field of view is centered on a region which is very close to the top wall of the cell where ignition is observed. In this configuration it is not possible to distinguish the plastic disc or the test cell prior to the combustion event due to the low light conditions, but it is possible to observe more distinctively the ignition kernel and the flame front upon ignition. Based on the images in Fig. 26 we estimate the flame speed is 1000 ± 100 m/s.

The ignition events occurring when the plastic disc separates the reactive mixture from the water all create a substantial amount of chemiluminescence. An Ocean FX spectrometer which can detect light emission between 200 and 1025 nm was used to measure the emission spectrum of the chemiluminescence. The optical resolution of the instrument is 1.7 nm. A few emission spectra obtained during test B065 are shown in Fig. 27. The vertical scale corresponds to the relative intensity in arbitrary units. The integration time of each spectrum is 0.1 ms. There is an approximately 0.2 ms interval between consecutive spectra due to instrument limitations.

The emission spectrum of the chemiluminescence consists of strong emission lines superimposed over broadband emission. The light emission between 293 nm and 322 nm, with two distinctive peaks at 298.0 nm and 310.6 nm, is likely due to hydroxyl radicals. The strong peak at 593.3 nm is likely a doublet due to sodium; the resolution of the spectrometer is not sufficient to resolve both peaks. The doublet at 766.3 nm and 769.5 nm is likely due to potassium. Sodium and potassium are contaminants which are likely to be found in our test setup.

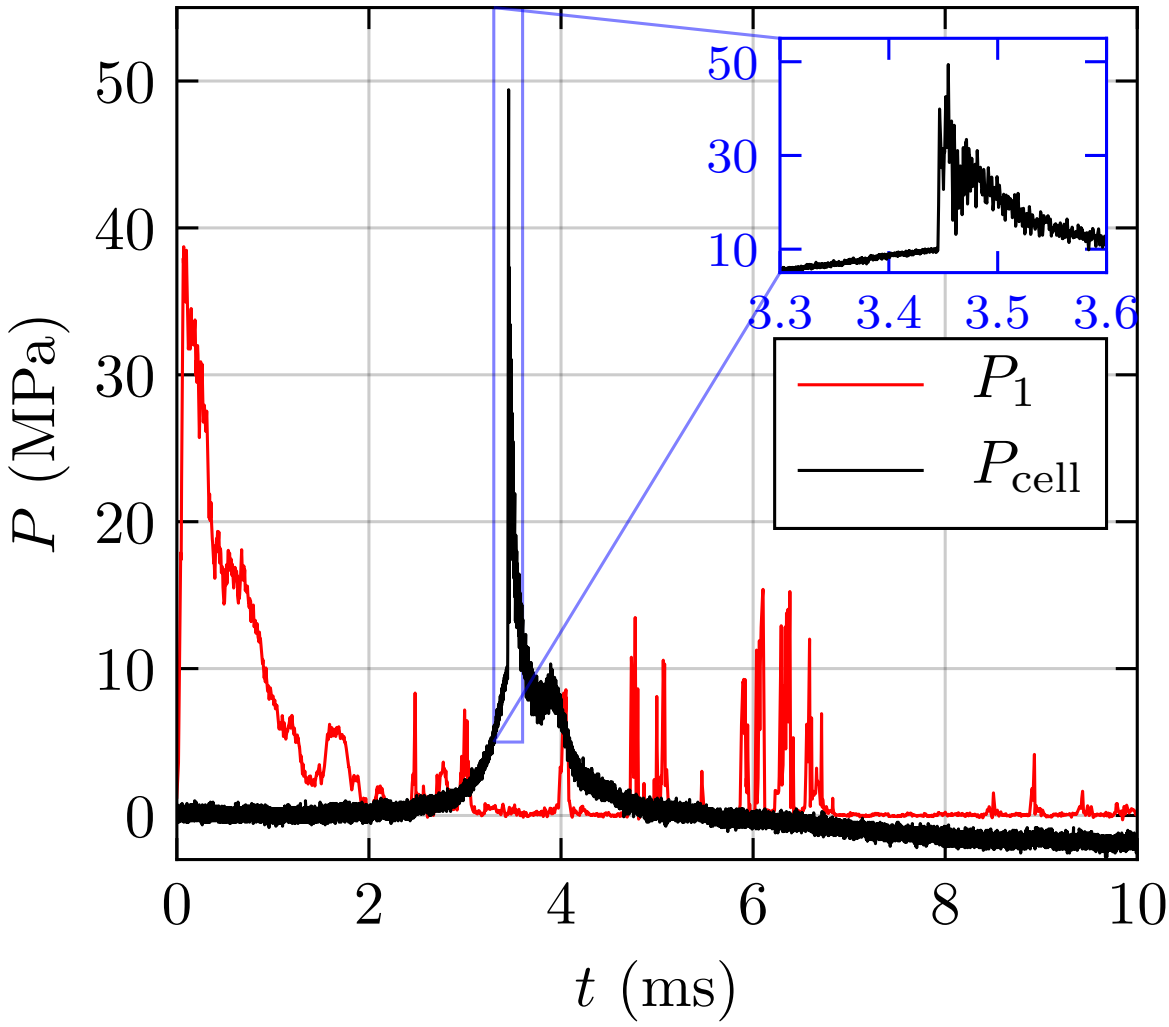

Figure 24: Pressure in the pipe and test cell during test B060.

In an attempt to explain the other peaks and broadband emission, we looked at the emission spectrum of other potential contaminants: polypropylene (plastic disc), paint from the flange, vacuum grease, rubber from the Buna O-rings, polycarbonate (test cell body material), and water. A small amount of each contaminant was added, one at a time, to a hydrogen-air diffusion flame burning at ambient conditions. The various emission bands we observed while burning those potential contaminants did not match the emission bands observed during test B065. This suggests that none of those potential contaminants considered were burning during test B065.

5.2 Tests without a disc

An undiluted stoichiometric mixture was used in 13 tests performed without a plastic disc separating the reactive gas from the water. One test was carried out with 50% N_2 dilution. All cases had a nominal gas volume height of 100 mm and projectile impact velocities between 20 and 35 m/s. A summary of the tests performed without a plastic disc is shown in Fig. 28 which can be directly compared to the disc results shown in Fig. 23.

Ignition was determined in these tests by examining the high-speed video for evidence of the characteristic luminosity of combustion and the pressure traces for evidence of the short-duration, high-pressure spikes, both of which

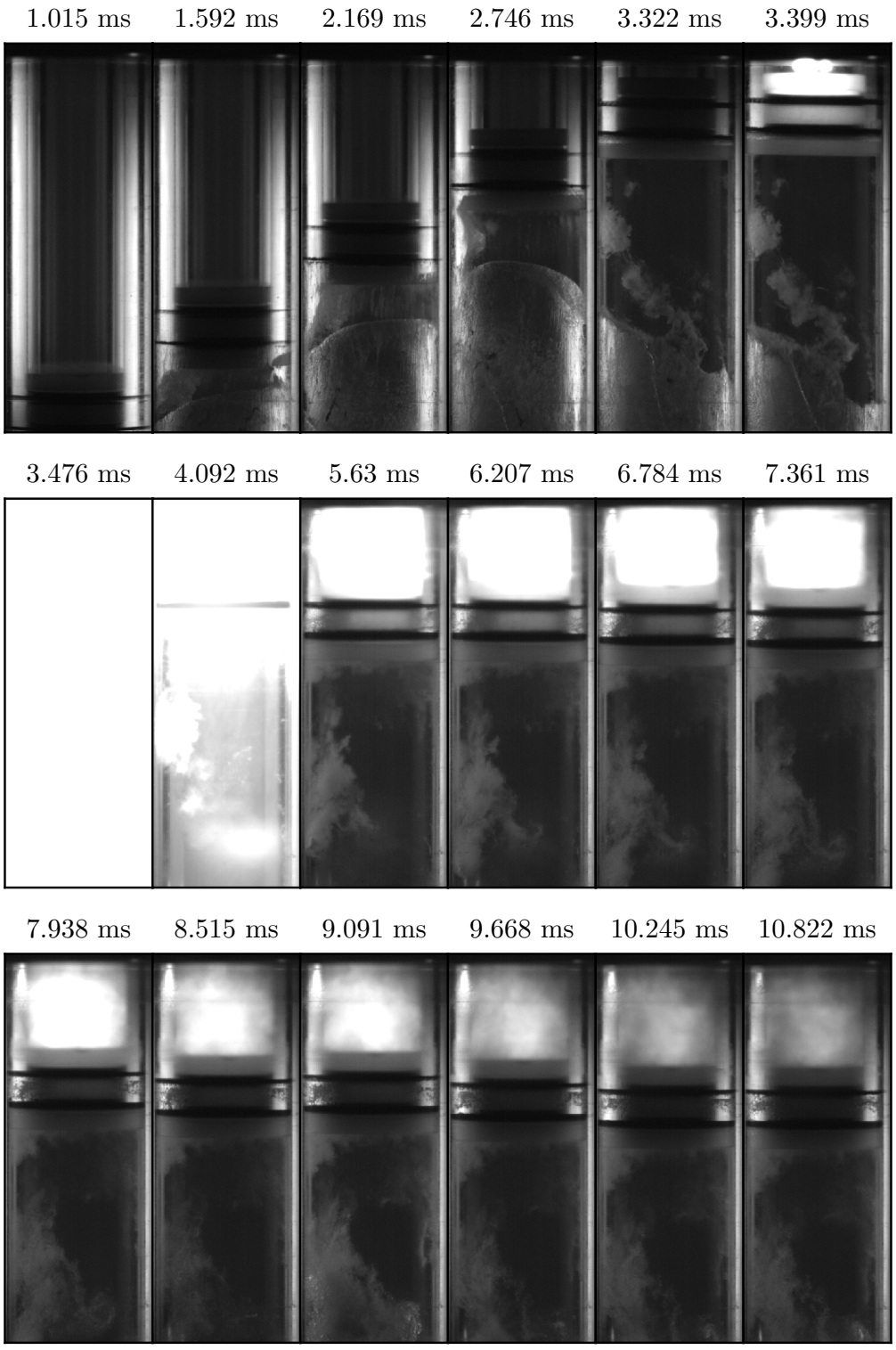

Figure 25: Sequence of images of the test cell for test B060.

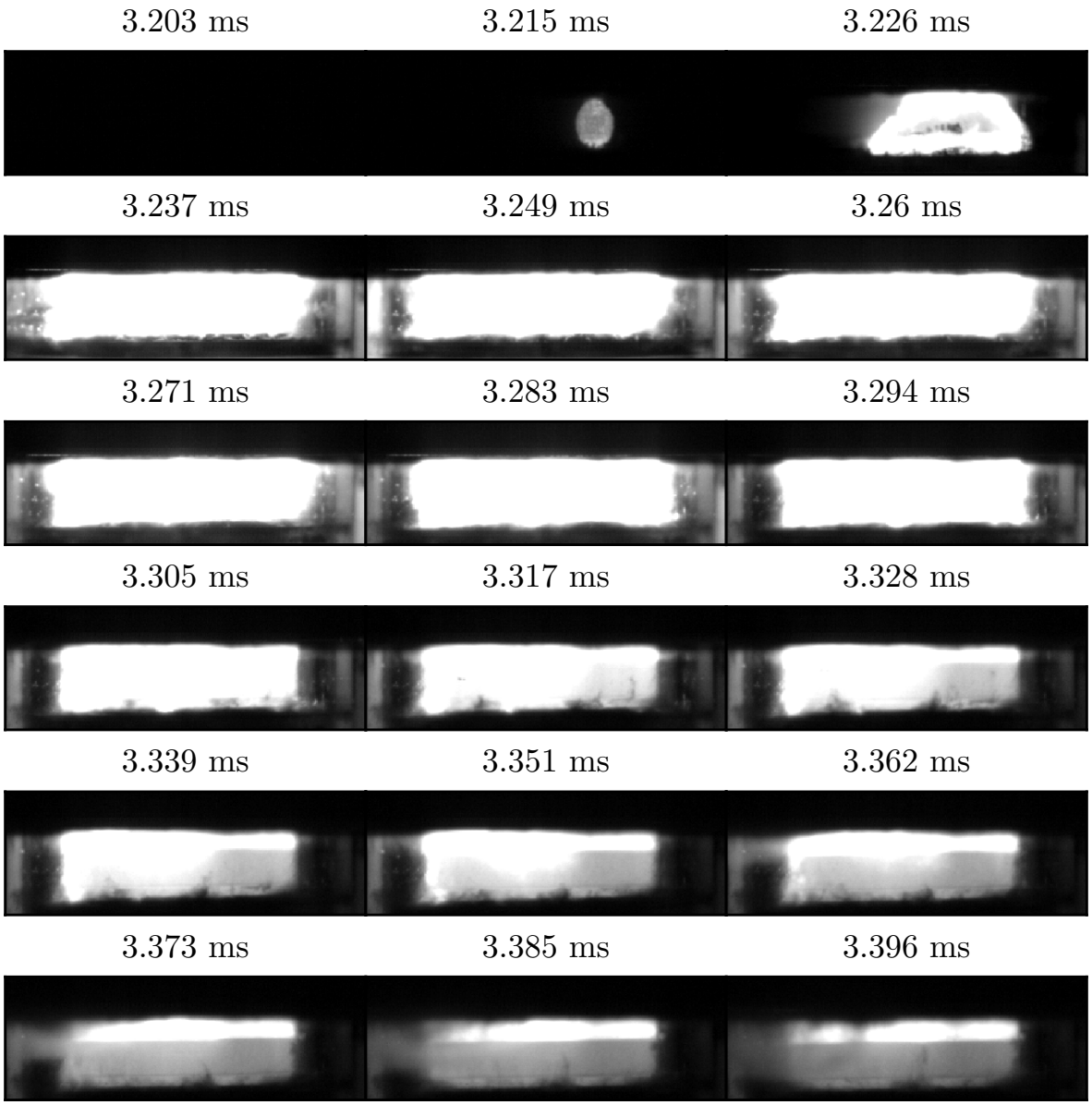

Figure 26: Sequence of images of the top portion of the test cell for test B065.

were observed in the tests with a disc that had successful ignition. Figure 28 indicates that ignition was observed in five of the tests performed without a plastic disc when the projectile velocity was greater that 29 m/s and the peak gas pressure was greater than 20 MPa. No ignition occurred in 9 tests including three repeat tests at 31 m/s impact velocity.

Both ignition and nonignition were observed in tests with projectile velocities between 29 and 31 m/s. This overlap indicates that there is some variability in the ignition process and ignition probability is more appropriate for describing ignition likelihood than a simple threshold. Based on the testing results with a disc, no effort was attempted to ignite diluted mixtures which would have likely required even higher impact velocities than are possible with the present experimental setup.

Tests without the disc show two striking differences from the tests with a disc. First, the ignition threshold for undiluted mixtures increased from an impact velocity of 26 (with disc) to 29 m/s (without a disc). Second, the high-

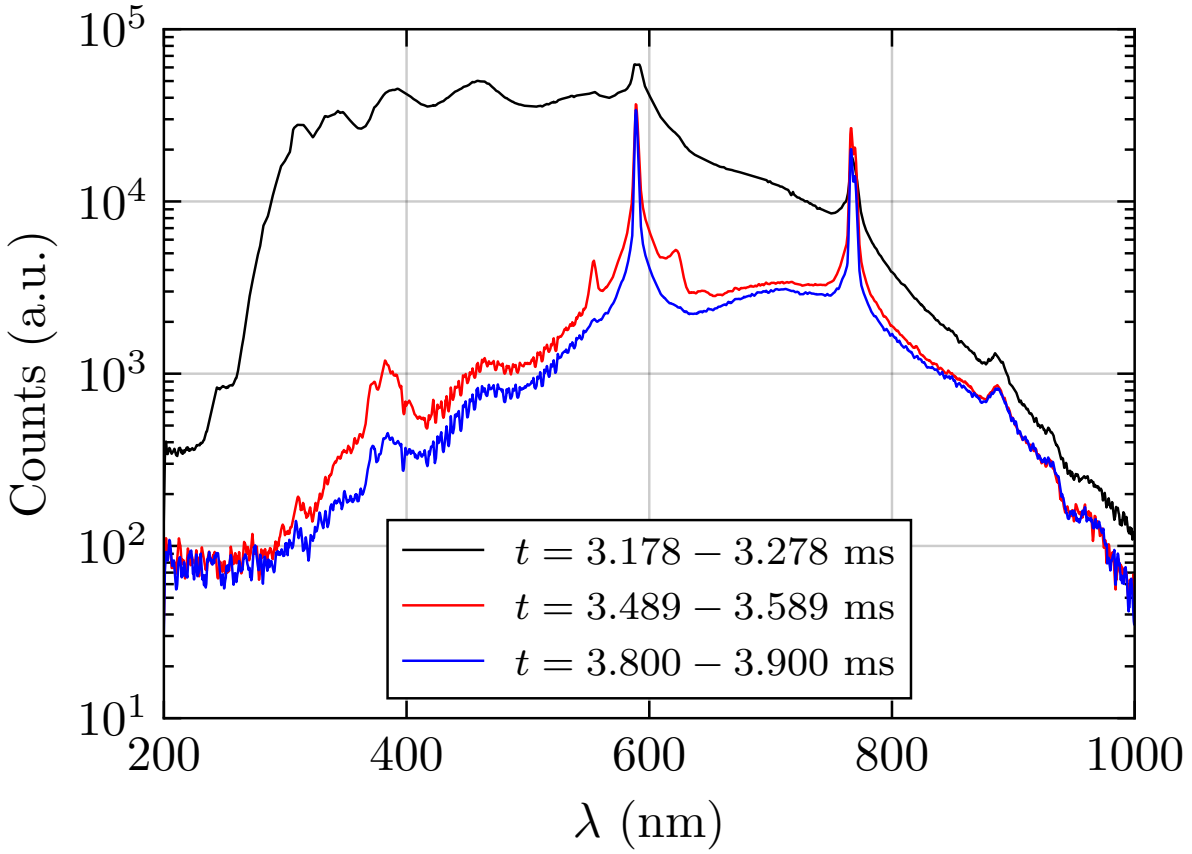

Figure 27: Spectra of the chemiluminescence for test B065.

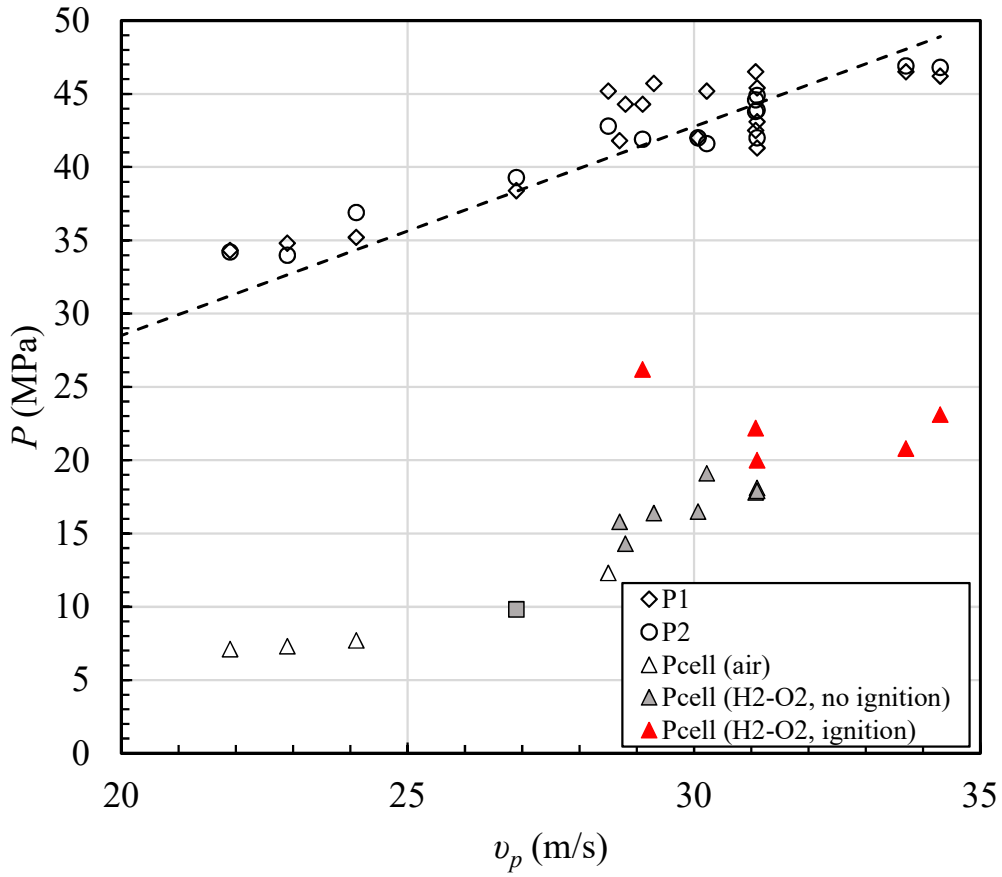

Figure 28: No disc configuration peak pressure and ignition results as a function of projectile velocity. The symbols have the same meaning as in Fig. 23.

pressure peaks observed in the tests with a disc (Fig. 23) were completely absent in the tests without a disc (Fig. 28). The highest peak pressure observed without a disc was 26.2 MPa at an impact velocity of 29.1 m/s. With a disc, the peak pressures ranged from 32 to 50 MPa at comparable impact velocities. The ignition events without a disc resulted in very low levels of luminosity in comparison to those with a disc. Instead of the entire gas region emitting light, emission is very localized and in some regions, entirely absent.

An ignition event without the disc is shown in Fig. 29 which contains a sequence of images of the test cell for test B059. The exposure, frame rate, and field of view of the camera is the same as for test B060. The ignition event is observed at 3.188 ms. A small amount of chemiluminescence is visible for 38 μs, or one frame. This is in extreme contrast to the results obtained with a disc, where the chemiluminescence was visible throughout the cell and persisted for several milliseconds.

The chemiluminescence visible in Fig. 29 is confined to a relatively small toroidal region adjacent to the test cell wall. We believe this is a direct consequence of the instabilities forming at the interface between the gas and the liquid which result in the formation of a central jet. This jet pushes the reactive mixture to the side of the test cell. With a disc separating the liquid and the reactive mixture the chemiluminescence was observed across the width of the test cell. The images from Fig. 29 and the small pressure increase also suggest that only a fraction of the reactive mixture initially contained in the cell ignites and burns since a flame was unable to propagate to the left-hand-side of the test cell. Because of the surface instabilities, the reactive mixture appears to be distributed within several pockets which are isolated from one from another.

Although ignition occurred within reactive pockets in the liquid-gas region, the ignition event was still discernible in the test cell pressure traces. Figures 30 and 31 show two different ignition cases corresponding to ignition pressures of 15.4 MPa and 19.6 MPa, respectively. In Fig. 30, the pressure rise due to heat release from the combustion event is

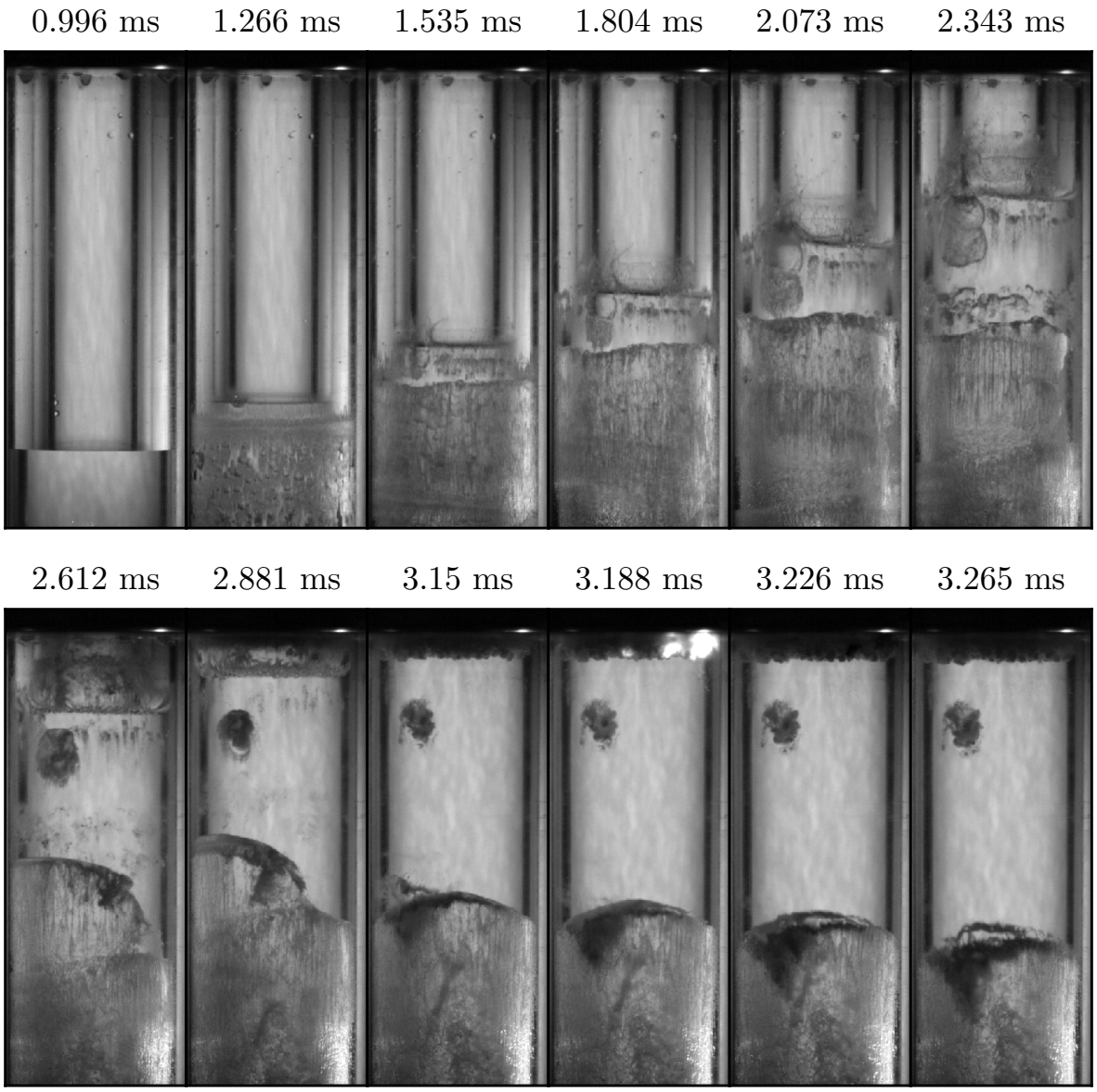

Figure 29: Sequence of images of the test cell for test B059.

approximately 13 MPa; however, a relatively smaller pressure rise of approximately 2 MPa is observed in Fig. 31.

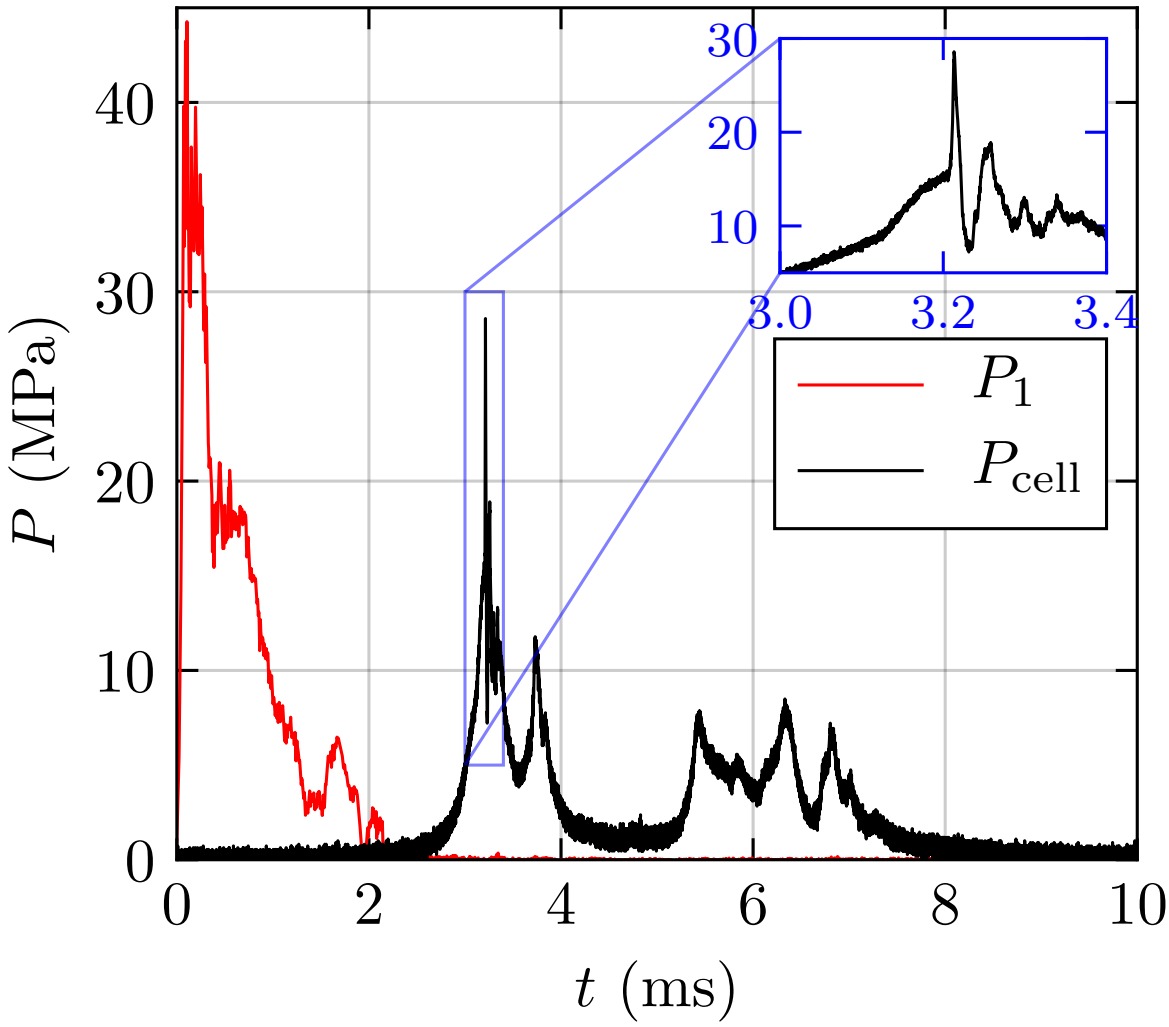

Figure 30: Pressure in the pipe and test cell during test B059.

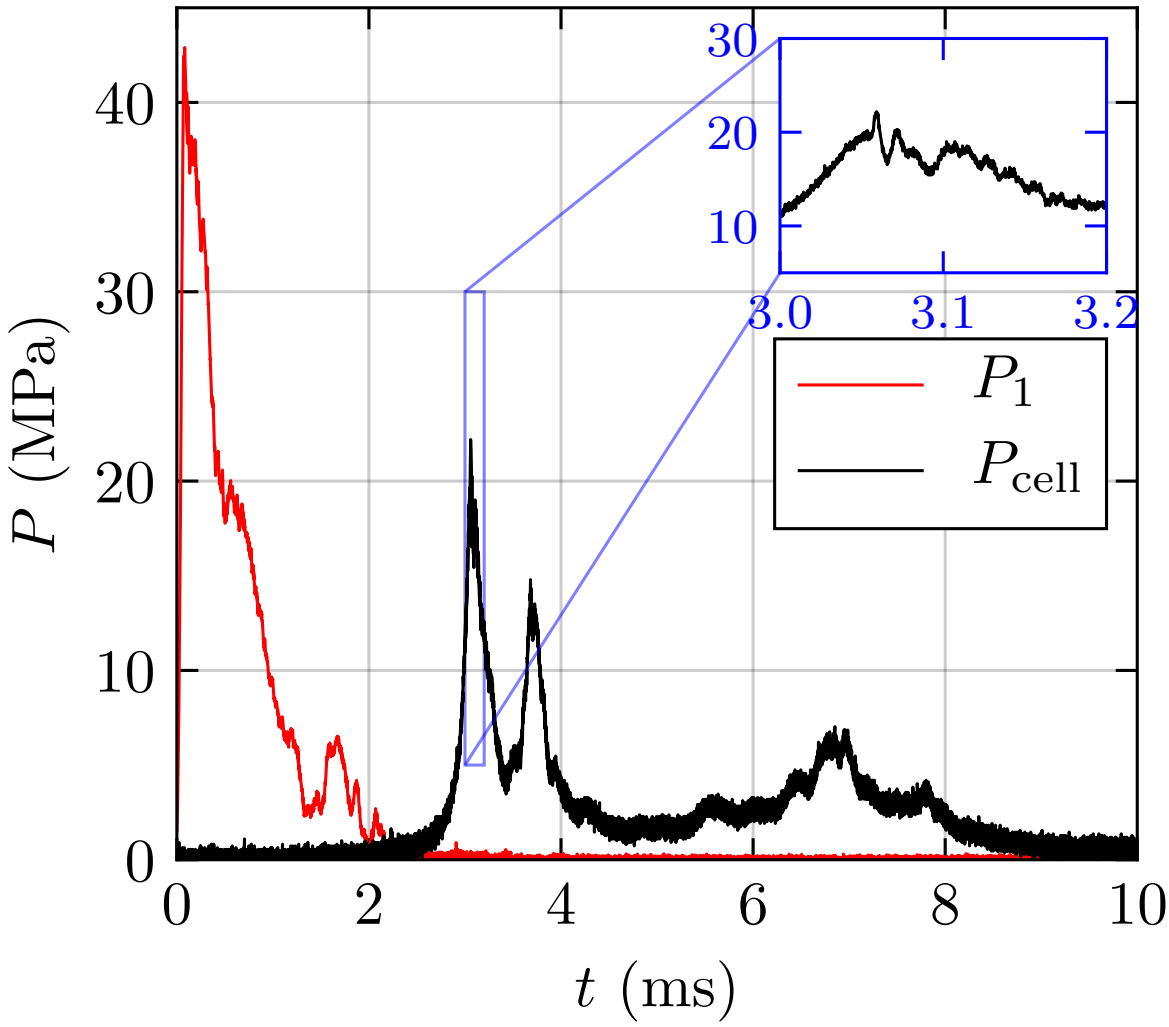

Figure 31: Pressure in the pipe and test cell during test B068.

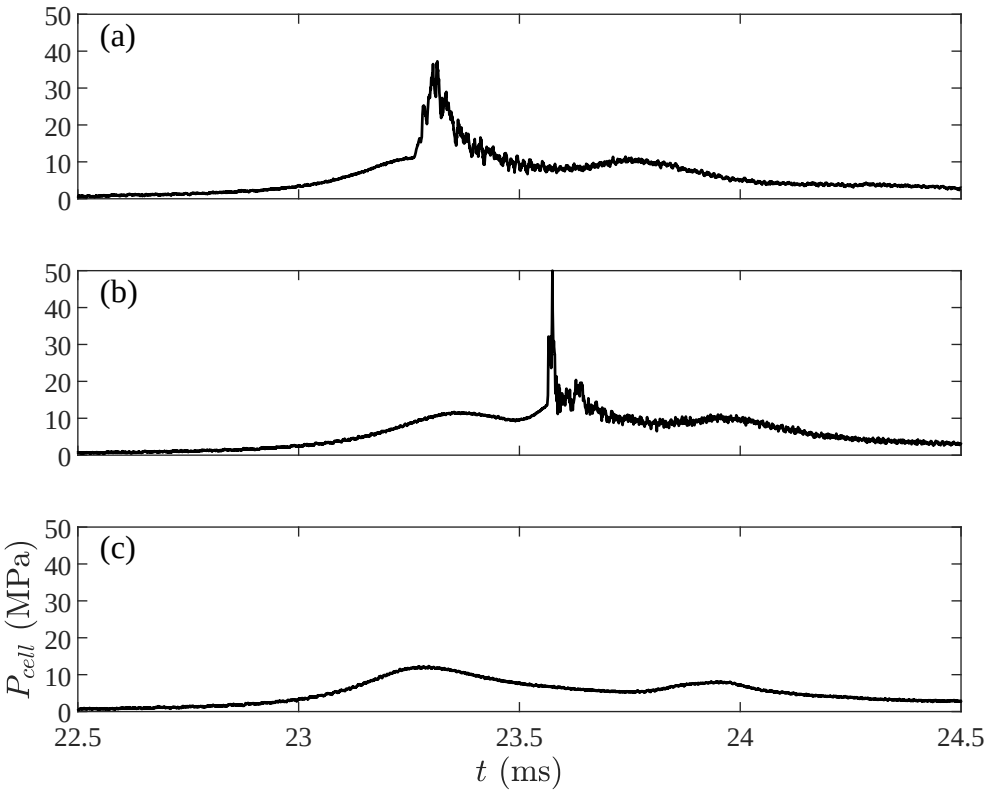

Figure 32: Comparison of three disc tests with similar impact velocities and gas volume heights but different amounts of N_2 dilution. a) Test B062, 0% dilution $2H_2 + O_2$, v_p = 28.3 m/s, h_0 = 100.5 mm. b) Test B047, 25% dilution $2H_2 + O_2 + N_2$, v_p = 28.2 m/s, h_0 = 103.2 mm. c) Test B046, 50% dilution $2H_2 + O_2 + 3N_2$, v_p = 28.1 m/s, h_0 = 100.3 mm.

5.3 Effect of N_2 dilution

Three (B042, B045, B046) of the four cases with 50% N_2 dilution did not obviously ignite (there was no flash of luminosity and the peak pressures were consistent with air compression) in the disc configuration despite using projectile impact velocity velocities up to 29 m/s and peak pressures of 17 MPa. Test B041, with v_p = 30 m/s, may have ignited; although there was no flash of luminosity, the peak pressure was 27 MPa, much higher than expected based on air compression tests. The combustion event in test B041 may have been masked by the obvious leakage of water past the O-ring seals and into the gas space during the compression phase.

The three 25% N_2 cases with projectile impact velocities greater than 26 m/s (peak pressures greater than 10 MPa) as well as all of the 0% N_2 cases all obviously ignited. Isentropic compression computations show that the addition of N_2 has a negligible effect on the pressure and temperature as a function of compression ratio because the specific heat capacity of both diluted and undiluted mixtures is nearly identical. The cell pressure histories (until initiation of explosion in the undiluted or air cases) for diluted and undiluted cases are also very similar for the same projectile velocities. An example is shown in Fig. 32 with nearly identical test parameters with the exception of gas composition. Explosions are observed for 0 (Fig. 32a) and 25% N_2 (Fig. 32b), but no ignition is observed for 50% N_2 (Fig. 32c). Of particular note is that the explosion is initiated during the compression phase for the most sensitive mixture (Fig. 32a), after the pressure peak and during the expansion for the less sensitive mixture (Fig. 32b) and not at all for the least sensitive mixture (Fig. 32c). This is consistent with the numerical simulations (Shepherd, 2019) of the Gaussian pulse which show that the ignition location recedes from the beginning to the end of the pulse with increasing ratio of induction time to pulse width parameter and ultimately, for sufficiently long induction time, ignition does not take place.

Given that the thermodynamic conditions and the cell pressure histories are not influenced by dilution we seek an explanation in terms of the effect of dilution on the critical pulse width τ_v^* and adiabatic ignition time τ_i^* . Due to the

lower energy content of the diluted mixtures, the self-heating effect (feedback between chemical energy release and reaction rates) is smaller for diluted than undiluted mixtures all other factors being the same. This means that both τ_i^* and τ_v^* will be longer in diluted than in undiluted mixtures.

It is challenging to directly measure τ_v and CR from the experiments, instead we use the characteristics of the pressure pulse: the half-width at half-maximum pressure $\tau_{p,1/2}$ and peak pressure P_m. We carried out computations (Shepherd, 2019) of critical pressure half-width parameters $\tau_{p,1/2}$ as a function of P_m for a Gaussian pressure pulse. The results for the nitrogen-diluted cases examined in the present study are shown in Fig. 33. The effect of dilution is to increase the critical pulse width required for ignition. For example at a peak pressure of 15 MPa, the critical pulse width is larger than the undiluted value by a factor of 1.3 for 25% N_2 dilution and 2.0 for 50% N_2 dilution. We speculate that the increase in $\tau_{p,1/2}^*$ with increasing dilution is what prevents ignition from taking place.

The experimental pressure-time histories measured for h_0 = 100 mm exhibit (see the pressure traces in Appendix C) multiple pressure peaks with a wide range of values for $\tau_{p,1/2}$ and peak cell pressures P_m. It is challenging to extract unique values of the pulse parameters and a simple parametric representation of the observed pressure pulses is not realistic. For example, in test B044 (Fig. 22), the broad pressure pulse between 2 and 3 ms, corresponds approximately to a Gaussian pulse with a half-width of 400 to 500 μs and peak pressure of 10 MPa with superimposed narrow (10-30 μs) pulses with peak pressures up to 15 MPa.

The observed peak pressures and pulse widths in the disc tests are shown in the shaded region on Fig. 33 and span the range of critical values for both diluted and undiluted mixtures. The estimated parameters characterizing the main pressure pulses observed in the tests of Fig. 32 are also shown on Fig. 33. The position of these parameters relative to the critical values for ignition is in accord with the experimental observations: Test B062 lies well above the critical curve of 0% N_2, test B047 is well above the critical curve for 25% N_2 and test B046 is close to the critical curve.

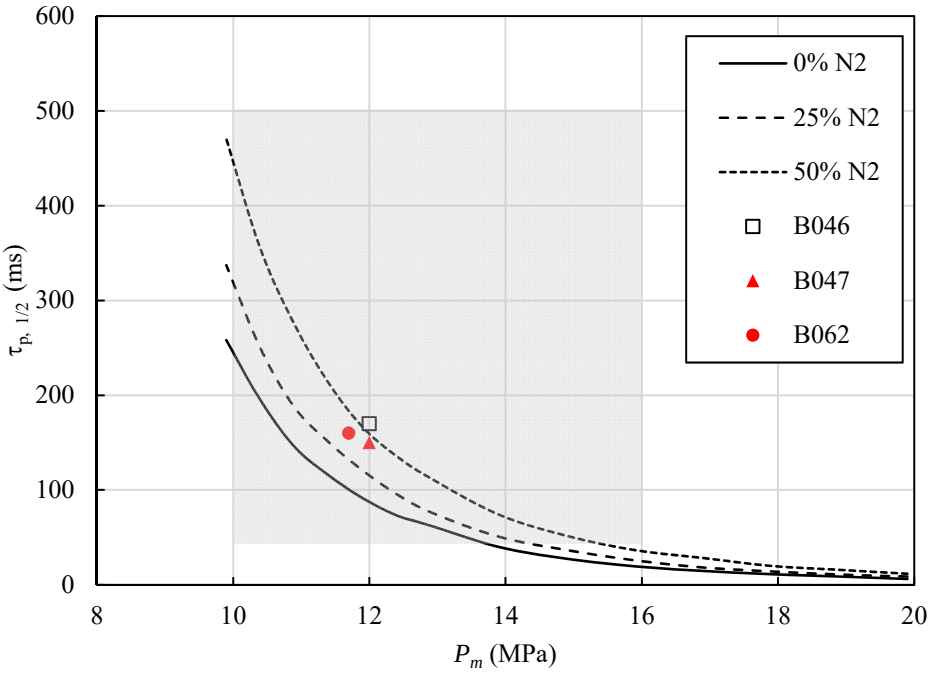

Figure 33: Critical pressure pulse parameter $\tau_{p,1/2}$ for a Gaussian pressure pulse as a function of the peak pressure rise P_m. The shaded region shows the range of observed values in the current tests.

6 Conclusions

One of the two key findings of our study is that the interaction of the liquid pressure wave with the liquid-gas interface results in rapid growth of disturbances on the initially planar interface and dispersion of the water into the gas. By separating the water from the gas with a rigid disc, we were able to demonstrate that the dispersion of the water into the gas significantly influences the ignition threshold and combustion process, suppressing the pressure rise generated by combustion. The other key finding is that short duration liquid pressure pulses result in a highly transient gas compression event and create the potential for quenching of combustion by rapid expansion that immediately follows compression, even in the cases where the dispersion of water is eliminated. This was examined in tests with N_2-diluted mixtures and analyzed using a simple model of the ignition process.

We attribute the observed interfacial instability to a combination of the impulsive acceleration of the interface (Richtmyer-Meshkov mechanism) and the continuous deceleration of the interface (Rayleigh-Taylor mechanism) occurring during the compression of the gas pocket. These instabilities as well as the cavitation region in the liquid adjacent to the liquid-gas interface result in a large increase in interfacial (water-gas) area and ultimately the breakup of the liquid water into a spray or mist that is dispersed into the gas volume.

The role of surface instabilities is to greatly increase the gas-water interfacial area, as well as create a spray or mist that mixes with the gas in the pocket. The increase in interfacial area will increase the heat transfer rate, and if the area is large enough and/or a fine spray is created, vaporization will be a significant heat transfer mode that competes with energy release and radical formation that is essential to the ignition process. We detect combustion by light emission (camera and spectroscopy) and pressure rise. When the mixing is suppressed by the disc, we are able to clearly observe the initiation of combustion as a luminous kernel of gas that rapidly expands to consume the gas mixture; in the most extreme case we observed a pressure rise of 40 MPa within 1 μs. Without the disc, mixing of water with the gas masks both pressure and luminosity signals making it challenging to determine the onset of combustion in all cases. However, it is clear that when combustion does occur, the pressure rise is suppressed.

Ignition was possible only when the projectile used to create the water hammer pressure pulse exceeded a threshold velocity of about 26 m/s (suppressing mixing with the disc) to 28 m/s (with mixing). The corresponding threshold peak pressures in the gas were 12 and 20 MPa at the onset of combustion. If we model the compression as isentropic, the peak temperature will be 1100 K at a peak pressure of 12 MPa. The transient nature of the compression pulse results in significant competition between chemical reaction and decrease of temperature in the expansion phase of the compression pulse so that the duration of the pulse has to be significantly longer than the constant-volume induction time at that temperature and pressure.

We interpret this in terms of critical conditions for ignition due to competition between chemical reaction, thermal energy exchange with the water and work done in the expansion phase of the compression pulse. Even when eliminating the mixing between gas and water, there is a threshold for ignition due to the transient nature of the compression pulses. We propose a simple model to account for the competition of energy release and expansion work during the compression transient. The model used an adiabatic variable-volume zero-dimensional formulation with a detailed chemical reaction mechanism and realistic thermochemistry that was validated against rapid compression machine experimental data. Critical conditions for ignition were computed in terms of limiting pressure or volume pulse widths as a function of the peak pressure or compression ratio.

The results of our tests have served to identify a number of important issues in experimental testing and computational modeling of ignition by water hammer. The key issue of interfacial instability and dispersion of water to create a multi-phase (gas-water) mixture has already been highlighted and will be a significant challenge for computational studies. These challenges include the prediction of the dispersion of water into jets and droplets as a consequence of the instability as well as exchange of mass and thermal energy between liquid and gas during the compression and ignition process. Reflection of the liquid pressure waves from the gas volume results in tension (negative pressure) and cavitation in the liquid, which may play a significant role in both the gas compression process as well as the dispersion of water into the gas phase. Although the cavitation in piping systems has been extensively studied over the past century, as with many aspects of multiphase flow, the computation treatment relies on empirical methods requiring substantial experimental calibration.

There are some significant limitations in generalizing the present results to evaluate the potential for reactive gas volume ignition due to water hammer in industrial facilities. We have examined only one configuration of the gas volume and one method of generating the pressure pulse. We used projectile impact for simulating water hammer pressure wave with peak pressures up to 50 MPa and an approximately triangular waveform with a total duration of 2-3 ms. These waves propagated through a 1.5 m long water-filled piping system connected to a vertical test section

filled with gas and compressed a 200 mL gas volume sufficiently to achieve gas pressures of up to 20 MPa. Clearly our system size is small in comparison to industrial facilities and our method of producing pressure pulses creates a limited range of pressure histories. The magnitude and duration of the pressure pulses are key factors in determining the potential for ignition and industrial situations will have to be evaluated on an individual basis. Finally, industrial facilities such as nuclear power plants have much higher operating pressures and temperatures which have to be taken into account in evaluating the critical conditions for ignition. Exploratory computations (Shepherd, 2019) using the higher initial pressures and temperatures indicate that initial temperature has the greatest effect on ignition thresholds.

Despite the significant differences in scale and pressure pulse parameters between our tests and industrial facilities, we anticipate that some of our findings will be universally applicable. Surface instabilities as well as the resulting mixing are well-known features that always occur when impulsively or rapidly accelerating an interface between fluids of different density. These instabilities are ubiquitous physical phenomena that are observed over an enormous range of length and time scales (Zhou, 2017) in many technological and natural situations. We expect that any realistic analysis of the potential ignition hazards of combustible gas pockets by water hammer must take these instabilities and the associated dispersion of water into the gas phase into account. Another aspect of our study that we anticipate is broadly applicable is the existence of critical time scales for pressure pulses to be effective in ignition. The concept of competition between chemical energy release and work done by expansion is valid for a wide range of situations and has to be taken into consideration in any evaluation of ignition thresholds during transient compression.

Acknowledgments

J.-C. Veilleux and S. A. Coronel contributed equally to this work. This work was carried out in the Explosion Dynamics Laboratory of the California Institute of Technology and was partially supported by the US Nuclear Regulatory Commission under Contract NRC-HQ-60-16-T-001.

References

Chemical-kinetic mechanisms for combustion applications. http://web.eng.ucsd.edu/mae/groups/combustion/mechanism.html, 2016. 28

A. Besov, V. Kedrinskii, J. Vries, and M. Kloosterman. Cavitation Thresholds, Free Surface and Cavity Cluster Dynamics in Liquids at Shock Wave Reflection. In A. R. Imre, H. J. Maris, and P. R. Williams, editors, *Liquids Under Negative Pressure*, pages 255–270. Springer Netherlands, Dordrecht, 2002. 2

Alfred E Beylich and Ali Gulhan. Waves in Reactive Bubbly Liquids. In GEA Meier and PA Thompson, editors, *Adiabatic Waves in Liquid-Vapor Systems*, pages 39–48, Goettingen, 1990. Springer Verlag Berlin Heidelberg. 1

L.R. Boeck, R. Mével, and T. Sattelmayer. Models for shock-induced ignition evaluated by detailed chemical kinetics for hydrogen/air in the context of deflagration-to-detonation transition. *Journal of Loss Prevention in the Process Industries*, 49:731–738, September 2017. 1

CE Brennen. *Cavitation and Bubble Dynamics*. Oxford University Press, 1995. 1, 9

T.M. Cain. Autoignition of hydrogen at high pressure. *Combustion and Flame*, 111(1-2):124–132, October 1997. 27

Apurba K. Das, Chih-Jen Sung, Yu Zhang, and Gaurav Mittal. Ignition delay study of moist hydrogen/oxidizer mixtures using a rapid compression machine. *International Journal of Hydrogen Energy*, 37(8):6901–6911, 2012. 27, 28, 29, 30

C. A. Eckett, J. J. Quirk, and and J. E. Shepherd. The role of unsteadiness in direct initiation of gaseous detonations. *Journal of Fluid Mechanics*, 421:147–183, 2000. 27

Fabio Ferrero, Ronald Meyer, Martin Kluge, Volkmar Schröder, and Tom Spoormaker. Self-ignition of tetrafluoroethylene induced by rapid valve opening in small diameter pipes. *Journal of Loss Prevention in the Process Industries*, 26(1):177–185, January 2013. 1

S.S. Goldsborough, S. Hochgreb, G. VanHove, M. Woolridge, H.J. Curran, and C-J. Sung. Advances in rapid compression machine studies of low- and intermediate-temperature autoignition phenomena. *Prog. Energy Combust. Sci.*, 63:1–78, 2017. 1, 27

David G. Goodwin, Harry K. Moffat, and Raymond L. Speth. Cantera: An object-oriented software toolkit for chemical kinetics, thermodynamics, and transport processes. http://www.cantera.org, 2014. Version 2.3. 27

K. P. Grogan and M. Ihme. Identification of governing physical processes of irregular combustion through machine learning. *Shock Waves*, 28(5):941–954, September 2018. 1

T. Hasegawa and T. Fujiwara. Detonation in oxyhydrogen bubbled liquids. *Symposium (International) on Combustion*, 19(1):675–683, January 1982. 1

J. Hershkowitz and B. M. Dobratz. Compendium of Nitromethane Data Relevant to the Tactical Explosive System (TEXS) Program:. Technical report, Defense Technical Information Center, Fort Belvoir, VA, April 1989. 1

Zekai Hong, David F. Davidson, and Ronald K. Hanson. An improved H2/O2 mechanism based on recent shock tube/laser absorption measurements. *Combustion and Flame*, 158(4):633–644, 2011. Special Issue on Kinetics. 28

K. Inaba and J. E. Shepherd. Dynamics of Cavitating Flow and Flexural Waves in Fluid-Filled Tubes Subject to Structural Impact. In *Proceedings of the ASME Pressure Vessels and Piping Conference. July 18-22, Bellevue, WA*, 2010. 10

Kazuaki Inaba and Joseph E. Shepherd. Plastic Deformation and Vibration in a Fluid-Filled Tube Subject to Axial Impact. In *ASME 2009 Pressure Vessels and Piping Conference*, volume 4: Fluid-Structure Interaction, Prague, Czech Republic, 2009. doi: 10.1115/PVP2009-77821. 3

Eric Johnsen and Tim Colonius. Shock-induced collapse of a gas bubble in shockwave lithotripsy. *The Journal of the Acoustical Society of America*, 124(4):2011–2020, October 2008. 1

V. K. Kedrinskii. *Hydrodynamics of Explosions: Experiment and Models*. High-Pressure Shock Compression of Condensed Matter. Springer, Berlin ; New York, 2005. 1

V.K. Kedrinskii. Surface Effects from an Underwater Explosion (Review). *J. Applied Mechanics and Technical Physics*, 19(4):474–491, 1978. 2

Alan Kéromnès, Wayne K. Metcalfe, Karl A. Heufer, Nicola Donohoe, Apurba K. Das, Chih-Jen Sung, Jürgen Herzler, Clemens Naumann, Peter Griebel, Olivier Mathieu, Michael C. Krejci, Eric L. Petersen, William J. Pitz, and Henry J. Curran. An experimental and detailed chemical kinetic modeling study of hydrogen and syngas mixture oxidation at elevated pressures. *Combustion and Flame*, 160(6):995–1011, 2013. 28

H. Kleine. Filming the invisible – time-resolved visualization of compressible flows. *Eur. Phys. J. Special Topics*, 182:3–34, 2010. 2

Tomohisa Kojima, Kazuaki Inaba, Kosuke Takahashi, Farid Triawan, and Kikuo Kishimoto. Dynamics of Wave Propagation Across Solid–Fluid Movable Interface in Fluid–Structure Interaction. *Journal of Pressure Vessel Technology*, 139(3):031308, January 2017. 16

D Lee and S Hochgreb. Hydrogen autoignition at pressures above the second explosion limit (0.6-4.0 MPa). *International Journal of Chemical Kinetics*, 30(6):385–406, June 1998. 27, 28

R.A Leishear. A Hydrogen Ignition Mechanism for Explosions in Nuclear Facility Piping Systems. *J. Pressure Vessel Technol.*, 135:054501, October 2013. 1

B.M. Maxwell and M.I. Radulescu. Ignition limits of rapidly expanding diffusion layers: Application to unsteady hydrogen jets. *Combustion and Flame*, 158(10):1946–1959, October 2011. 27

R. Mével, S. Javoy, F. Lafosse, N. Chaumeix, G. Dupré, and C.-E. Paillard. Hydrogen–nitrous oxide delay times: Shock tube experimental study and kinetic modelling. *Proceedings of the Combustion Institute*, 32(1):359–366, 2009. 28

R. Mével, S. Javoy, and G. Dupré. A chemical kinetic study of the oxidation of silane by nitrous oxide, nitric oxide and oxygen. *Proceedings of the Combustion Institute*, 33(1):485–492, 2011. 28

R. Mével, J. Melguizo-Gavilanes, and D. Davidenko. Ignition of hydrogen-air mixtures under volumetric expansion. *Proceedings of the Combustion Institute*, 37(3):3503–3511, 2019. 27

K. Mitropetros, H. Hieronymus, and J. Steinbach. Single bubble ignition after shock wave impact. *Chemical Engineering Science*, 61(2):397–416, January 2006. 1

K. A. Mørch. Cavitation inception from bubble nuclei. *Interface Focus*, 5(5):20150006, October 2015. 9

Bradley Motl, Jason Oakley, Devesh Ranjan, Chris Weber, Mark Anderson, and Riccardo Bonazza. Experimental validation of a Richtmyer–Meshkov scaling law over large density ratio and shock strength ranges. *Physics of Fluids*, 21(12):126102, December 2009. 18

M. Naitoh, F. Kasahara, R. Kubota, and I. Ohshima. Analysis on Pipe Rupture of Steam Condensation Line at Hamaoka-1, (II) Hydrogen Combustion and Pipe Deformation. *J. Nucl. Sci. Technol.*, 40(12):1041–1051, 2003a. 1

M. Naitoh, F. Kasahara, T. Mitushashi, and I. Ohshima. Analysis on Pipe Rupture of Steam Condensation Line at Hamaoka-1, (I) Accumulation of Non-condensable Gas in a Pipe. *J. Nucl. Sci. Technol.*, 40(12):1032–1040, 2003b. 1

Kiyonobu Ohtani and Toshihiro Ogawa. Expansion wave and cavitation bubble generation by underwater shock wave reflection from the interface. *Mechanical Engineering Journal*, 3(6):16–00298–16–00298, 2016. 2

Pinaki Pal, Mauro Valorani, Paul G. Arias, Hong G. Im, Margaret S. Wooldridge, Pietro P. Ciottoli, and Riccardo M. Galassi. Computational characterization of ignition regimes in a syngas/air mixture with temperature fluctuations. *Proceedings of the Combustion Institute*, 36(3):3705–3716, 2017. 1

AV Pinaev and AI Sychev. Effects of Gas and Liquid Properties on Detonation-Wave Parameters in Liquid-Bubble Systems. *Combustion Explosion and Shock Waves*, 23(6):735–742, Nov-Dec 1987. 1

Matei I. Radulescu and Brian M. Maxwell. Critical ignition in rapidly expanding self-similar flows. *Physics of Fluids*, 22(6):066101, June 2010. 27

M. W. Ringer. Detonation tests and response analyses of vessels and piping containing gas and aerated liquid. *Plant/Oper. Progress*, 4(1):26–47, 1985. 1

H Schulz, A Voswinkel, and H Reck. Insights and Lessons Learned from the Brunsbüttel Piping Failure Event. In *Eurosafe-Forum*, page 7, 2002. 1

J. E. Shepherd and K. Inaba. Shock Loading and Failure of Fluid-Filled Tubular Structures. In A. Shukla, G. Ravichandran, and Y. Rajapakse, editors, *Dynamic Failure of Materials and Structures*, pages 153–190. Springer, 2010. 8, 9, 16

Joseph E. Shepherd. Ignition Modeling and the Critical Decay Rate Concept. GALCIT Report EDL2019.002, California Institute of Technology, Pasadena, CA 91125, August 2019. 27, 30, 44, 45, 47

H.H. Shi and Q.-W. Zhuo. Shock wave induced instability at a rectangular gas/liquid interface. In *Shock Waves*, volume 2, pages 1211–1216. Springer, 2009. 2

Gregory P. Smith, David M. Golden, Michael Frenklach, Nigel W. Moriarty, Boris Eiteneer, Mikhail Goldenberg, C. Thomas Bowman, Ronald K. Hanson, Soonho Song, William C. Gardiner, Jr., Vitali V. Lissianski, and Zhiwei Qin. GRI-Mech 3.0. http://www.me.berkeley.edu/gri_mech/, 1999. 28

G. I. Taylor. The instability of liquid surfaces when accelerated in a direction perpendicular to their planes. I. *Proc. R. Soc. Lond. A*, 201(1065):192–196, March 1950. 19

D.H. Trevena. *Cavitation and Tension in Liquids*. Adam Hilger, 1987. 9

Jean-Christophe Veilleux and Joseph E. Shepherd. Impulsive Motion in a Cylindrical Fluid-Filled Tube Terminated by a Converging Section. *J. Pressure Vessel Technol*, 141(2):021302, February 2019. 10

Xiao-Liang Wang, Motoyuki Itoh, Hong-Hui Shi, and Masami Kishimoto. Experimental Study of Rayleigh–Taylor Instability in a Shock Tube Accompanying Cavity Formation. *Jpn. J. Appl. Phys.*, 40(Part 1, No. 11):6668–6674, November 2001. 2

PR Williams and RL Williams. Cavitation and the tensile strength of liquids under dynamic stressing. *Molecular Physics*, 102(19-20):2091–2102, 2004. 9

E. Wylie and V. Streeter. *Fluid Transients in Systems*. Prentice Hall, Englewood Cliffs, NJ, 1993. 1, 9

Ye Zhou. Rayleigh–Taylor and Richtmyer–Meshkov instability induced flow, turbulence, and mixing. I. *Physics Reports*, 720-722:1–136, December 2017. 2, 18, 19, 47

A Test Series A

Table 2: Series A test conditions and key results. The initial gas (air) volume height is h_0, peak pressures rises are given for all transducers. Projectile impact velocity was 6.5 to 6.7 m/s for all cases. Nominal initial conditions in the gas volume was 101 kPa and 298 K.

Shot	h_0 (mm)	P_1 (MPa)	P_2 (MPa)	P_3 (MPa)	P_4 (MPa)	P_{cell} (MPa)
3	49.1	9.11	9.12	4.70	4.60	0.55
4	54.4	9.07	8.55	4.15	4.16	0.46
5	54.1	9.24	8.41	5.85	6.50	0.61
9	53.8	7.27	6.74	6.45	6.25	0.53
10	37.2	8.63	8.53	8.26	8.31	0.69
11	36.8	8.78	8.79	8.42	8.42	0.76
12	36.6	8.63	8.37	8.11	8.04	0.71
14	27.1	8.91	8.20	7.89	7.84	1.03
15	26.5	9.22	8.44	8.18	8.11	0.97
16	18.3	8.66	8.41	7.98	7.89	1.56
17	18.0	9.17	8.83	8.41	8.30	1.56
18	18.0	8.82	8.15	7.89	7.83	1.59
19	10.0	9.26	8.39	7.93	7.91	4.09
20	9.8	9.16	8.28	8.06	8.03	4.18
21	9.7	8.78	8.46	8.18	8.03	4.23
22	2.9	8.88	8.31	7.92	7.76	10.9
23	2.9	8.79	8.26	7.97	7.85	12.9
24	2.6	9.19	8.30	8.03	8.99	15.01
25	117.2	9.56	9.35	2.16	2.36	0.19
26	117.5	8.78	8.43	2.13	2.18	0.20
27	117.5	9.39	8.95	2.65	2.92	0.20
28	77.6	8.86	7.97	3.97	3.69	0.32
29	77.3	7.72	7.11	2.86	2.88	0.26
30	77.6	7.37	6.52	3.34	3.37	0.27
31	4.9	9.14	8.04	4.50	4.50	5.41
32	4.2	9.14	8.10	5.33	5.05	5.33
33	7.4	8.87	8.10	6.60	7.01	4.57

B Test Series B

Table 3: Series B test conditions and key results. The initial gas (air) volume height is h_0; projectile and buffer velocity are v_p and v_b; peak pressures are given for transducers 1, 2 and the cell. The *Ignition* entry is blank for a nonreactive test, 0 for a reactive test that did not ignite, 1 for a reactive test that did. The *Disc* entry is blank if no disc was used and 1 if a disc was present at the liquid-gas interface. Nominal initial conditions in the gas volume was 101 kPa and 298 K for all cases.

Shot	h_0 (mm)	v_p (m/s)	v_b (m/s)	P_1 (MPa)	P_2 (MPa)	P_{CELL} (MPa)	*Ignition*	*Gas* air	*Disc*
9	29.4	9.1	6.1	14.0	13.0	0.2		air	
10	29.0	16.3	12.0	24.9	23.2	0.4		air	
11	29.6	13.3	9.6	20.0	20.0			air	
12	29.7	3.3	2.4	5.4	4.8			air	
14	29.4	6.6	5.3	10.3	9.7	0.3		air	
15	29.7	8.6	6.7	13.9	13.1	0.2		air	
16	30.1	11.4	8.4	17.7	17.1			air	
17	29.3	9.8	7.4	15.0	14.2	2.8		air	
18	29.6	11.6	9.1	17.1	16.8	6.4		air	
19	29.0	13.3	9.6	19.5	20.1	8.4		air	
20	29.7	14.2	10.8	21.6	21.8	10.3		air	
21	29.4	16.3	12.5	24.4	23.4	10.0		air	
22	29.4	7.8	6.0	11.9	10.8	2.3		air	
23	28.8	17.3	13.9	29.2	25.6	10.4		air	
24	29.6	5.6	3.8	7.7	8.0	1.0		air	
25	30.0	19.0	14.1	28.1	27.3	16.9		air	
26	29.1	11.3	7.9	17.2	15.6	4.2		air	
27	29.6	18.3	13.2	26.1	28.0	19.6		air	
28	29.4	17.7	12.0	27.2	27.4	18.3		air	
29	48.4	16.3	11.3	24.1	24.3	6.5		air	
30	49.6	16.3	12.4	25.1	25.1	5.4		air	
31	49.7	18.1	13.2	27.6	27.4	6.5		air	
32	49.0	19.1	14.8	28.6	29.3	8.2		air	
33	48.8	20.2	14.4	30.4	31.3	9.2		air	
34	49.7	20.5	15.1	32.8	31.2	9.3		air	
35	99.5	21.9	15.3	34.3	34.2	7.1		air	
36	99.8	22.9	16.7	34.8	34.0	7.3		air	
37	100.2	24.1	17.1	35.2	36.9	7.7		air	
38	101.4	26.9	21.6	38.4	39.3	9.8	0	$2H_2$+O_2+$3N_2$	
39	101.5	28.5	25.2	45.2	42.8	12.3		air	
40	96.5	28.5		43.6	44.1	16.9		air	1
41	97.5	29.9	22.9	46.4	42.8	27.0	0	$2H_2$+O_2+$3N_2$	1
42	98.5	28.6		44.7	40.5	15.9	0	$2H_2$+O_2+$3N_2$	1
43	102.2	28.0	23.4	48.7	39.7			air	1
44	101.1	28.9	23.2	41.4	41.0	15.6		air	1
45	100.3	28.9	24.4	45.9	42.4	16.9	0	$2H_2$+O_2+$3N_2$	1
46	100.3	28.1	22.2	41.8	41.0	12.1	0	$2H_2$+O_2+$3N_2$	1
47	103.2	28.2	22.1	44.3	41.9	35.6	1	$2H_2$+O_2+N_2	1
48	97.4	26.7	23.4	43.2	38.9	28.8	1	$2H_2$+O_2+N_2	1
49	98.2	25.6	21.0	42.6	36.3	8.7	0	$2H_2$+O_2+N_2	1
50	97.4	26.1	20.9	39.0	37.1	21.9	1	$2H_2$+O_2+N_2	1
51	98.8	27.2	23.2	39.7		43.6	1	$2H_2$+O_2	1
52	98.2	25.2	22.2	36.5		9.9	0	$2H_2$+O_2	1
53	102.2	26.2	22.2	39.3	40.9	32.7	1	$2H_2$+O_2	1

Shot	h_0 (mm)	v_p (m/s)	v_b (m/s)	P_1 (MPa)	P_2 (MPa)	P_{CELL} (MPa)	*Ignition*	*Gas* air	*Disc*
54	97.7	25.6	22.2	40.6	37.0	9.5	0	$2H_2$+O_2	1
55	99.4	25.8	21.0	39.2		10.1	0	$2H_2$+O_2	1
56	102.8	28.8	25.7	44.3		14.3	0	$2H_2$+O_2	
57	103.1	29.3	24.4	45.7		16.4	0	$2H_2$+O_2	
58	101.1	28.7	24.4	41.8		15.8	0	$2H_2$+O_2	
59	99.7	29.1	24.5	44.3	41.9	26.2	1	$2H_2$+O_2	
60	100.6	26.8	23.4	38.7	39.8	49.4	1	$2H_2$+O_2	1
61	100.0	27.3		41.7	39.1	57.5	1	$2H_2$+O_2	1
62	100.5	28.3	24.4	40.8	40.3	37.8	1	$2H_2$+O_2	1
63	100.0	28.5		42.4	39.5	44.7	1	$2H_2$+O_2	1
64	100.0	28.6		40.1	39.8	33.1	1	$2H_2$+O_2	1
65	100.0	28.5		41.2	40.3	50.6	1	$2H_2$+O_2	1
66	98.8	30.2		45.2	41.6	19.1	0	$2H_2$+O_2	
67	100.8	30.1		42.0	42.0	16.5	0	$2H_2$+O_2	
68	101.8	31.1		42.5	43.8	22.2	1	$2H_2$+O_2	
69	99.1	31.1		43.1	43.9	18.1	0	$2H_2$+O_2	
70	100.8	31.1		41.3	42.0	20.0	1	$2H_2$+O_2	
71	100.0	31.1		45.4	44.9	17.9	0	$2H_2$+O_2	
72	101.7	31.1		46.5	44.6	17.8	0	$2H_2$+O_2	
73	100.0	34.3	28.0	46.2	46.8	23.1	1	$2H_2$+O_2	
74	100.0	33.7	29.2	46.5	46.9	20.8	1	$2H_2$+O_2	

C Plots for Test Series B

This appendix provides data plots for most of the most of the tests in Series B. For most tests, two plots are given: a composite plot of pressure vs time for the transducers that provided valid signals and a plot of the projectile and buffer trajectories. Due to issues with the data acquisition and image analysis, not at all pressure signals or trajectories were processed.

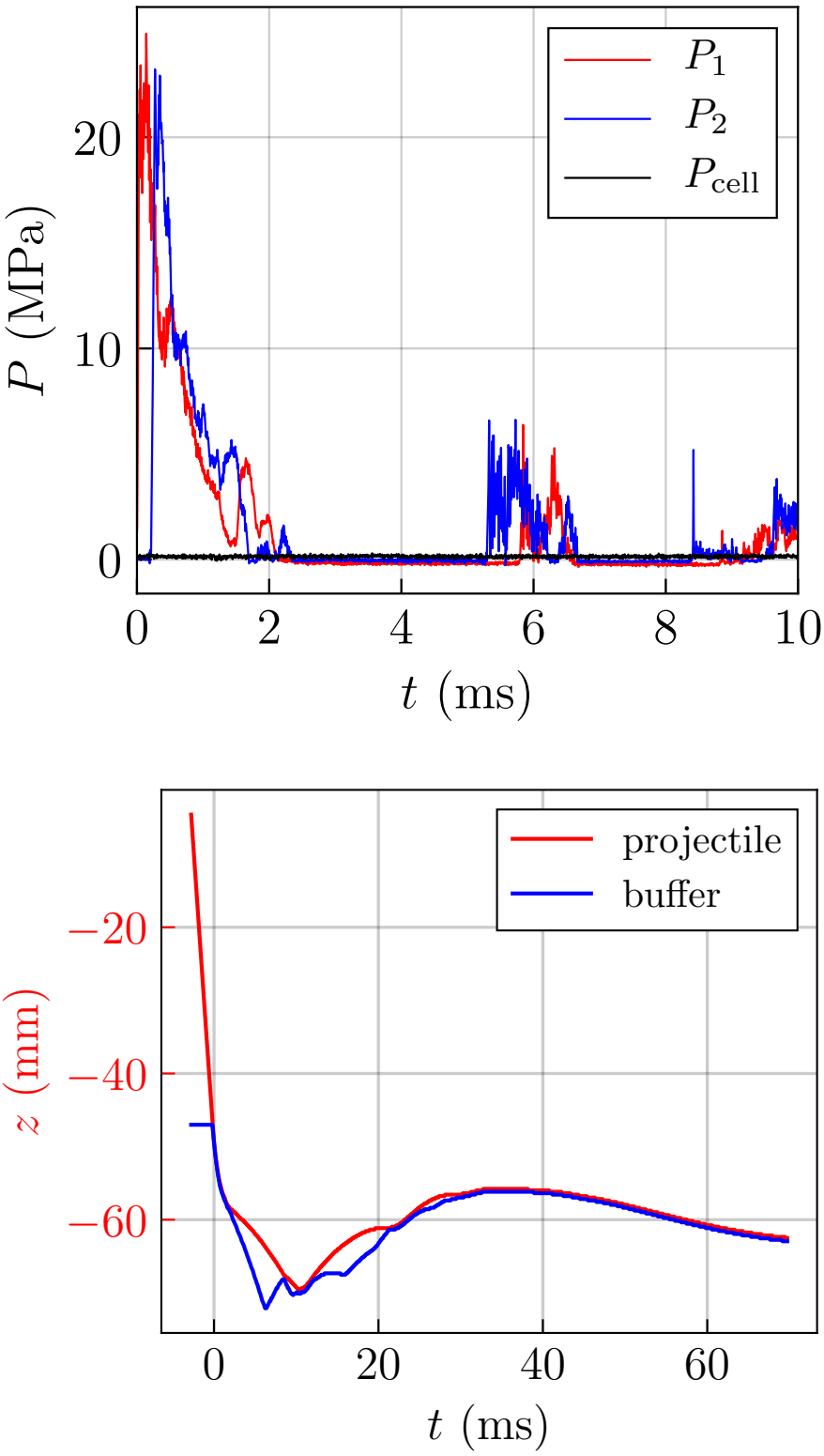

Figure 34: Test B010

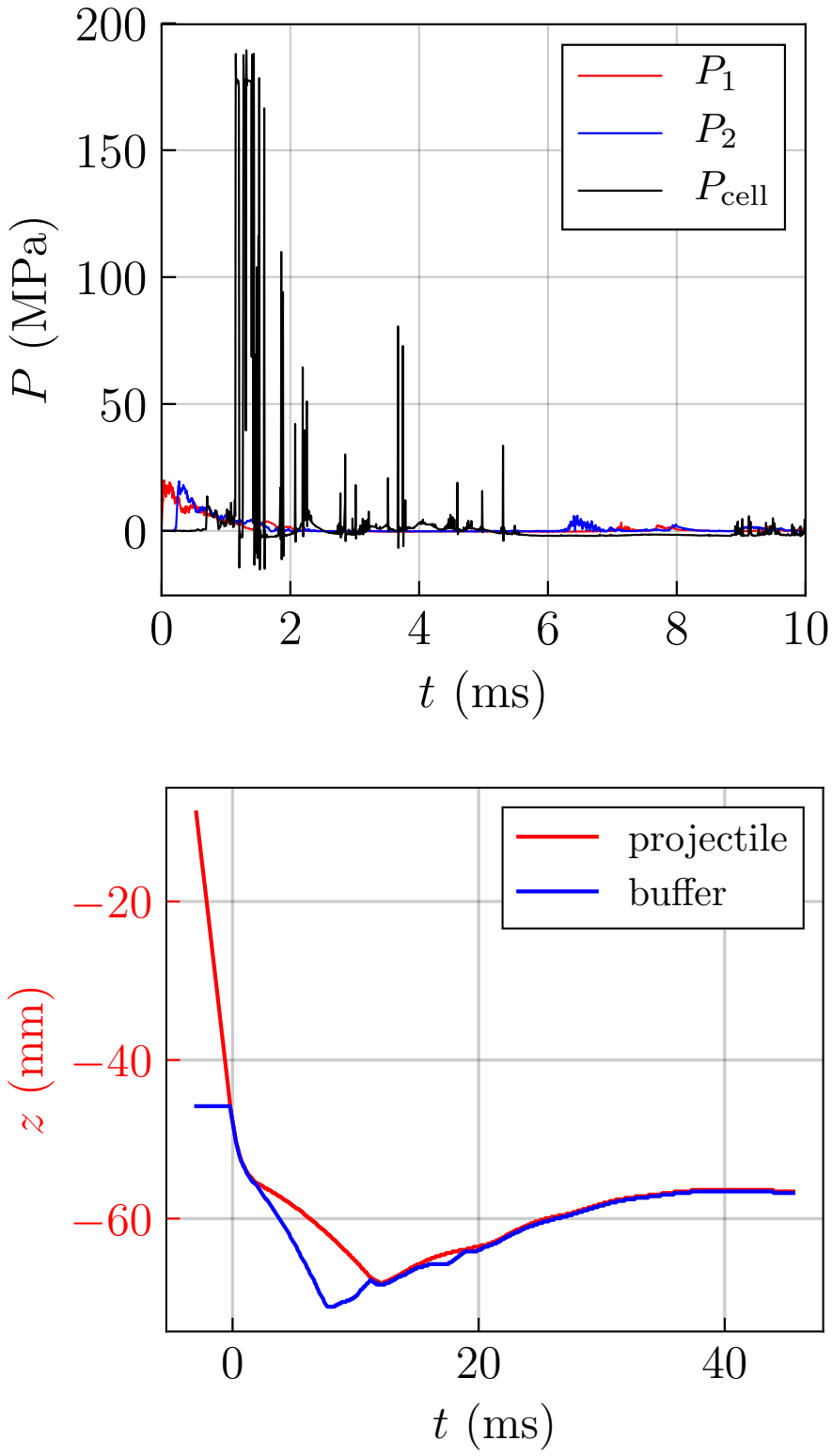

Figure 35: Test B011

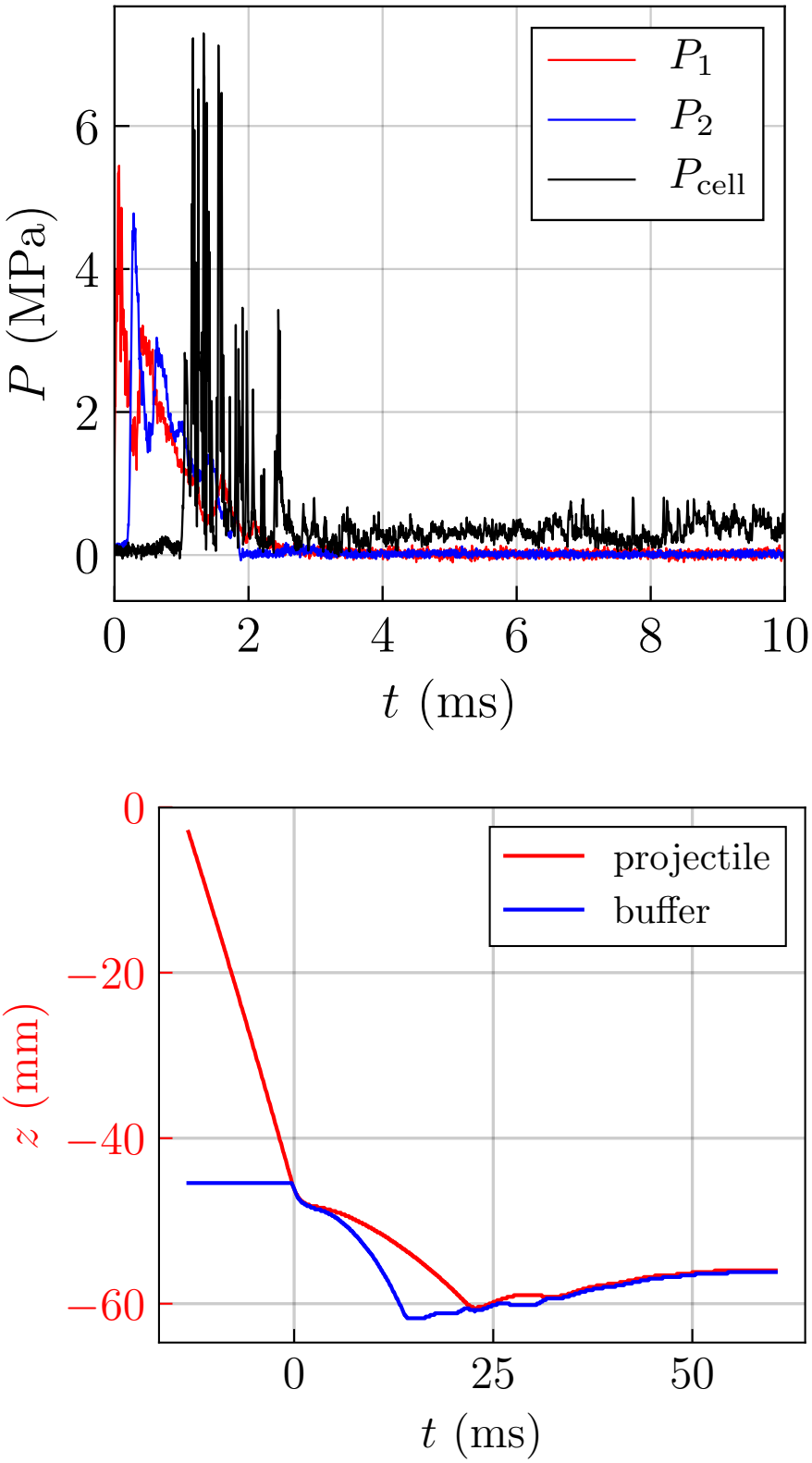

Figure 36: Test B012

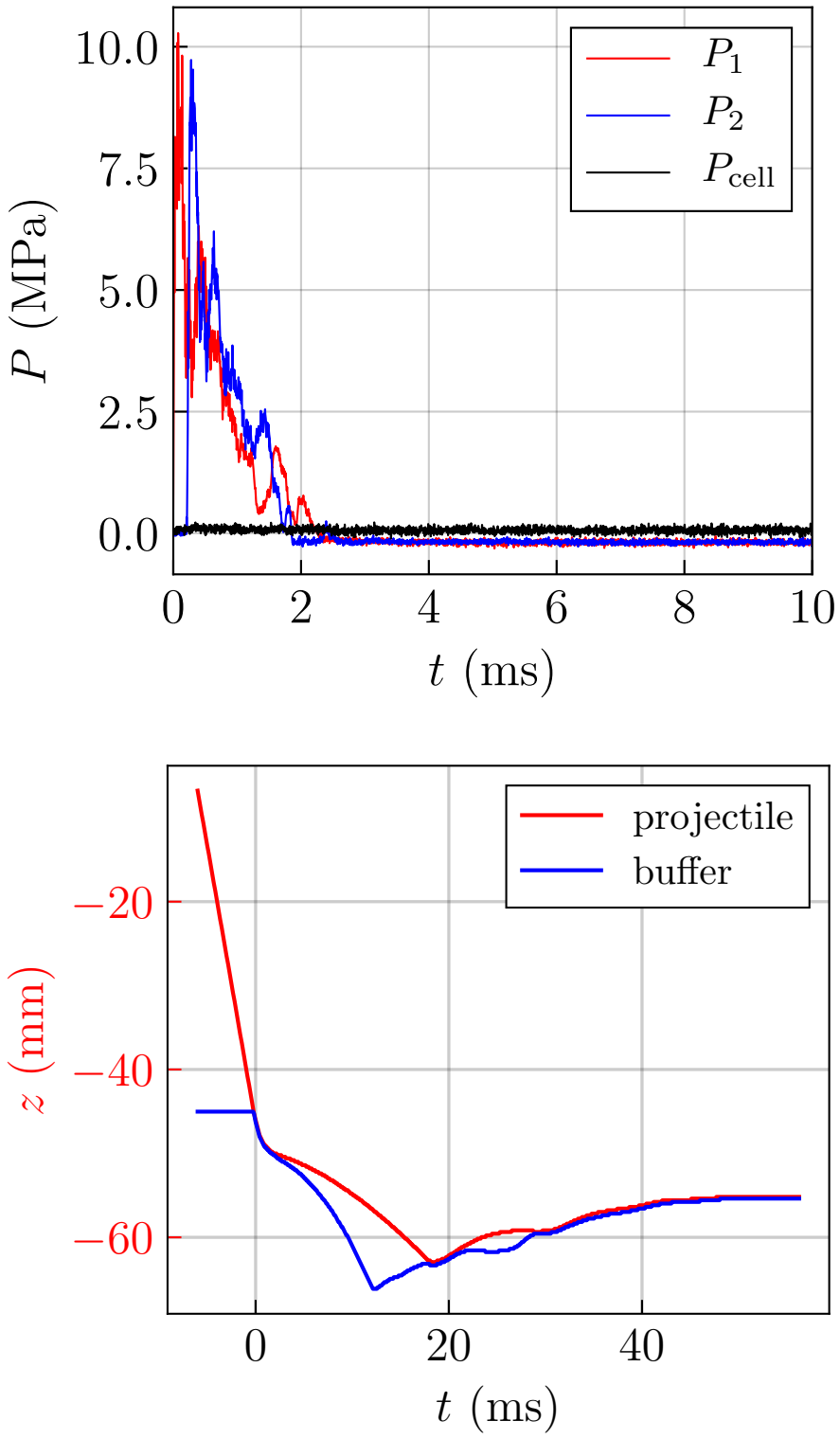

Figure 37: Test B014

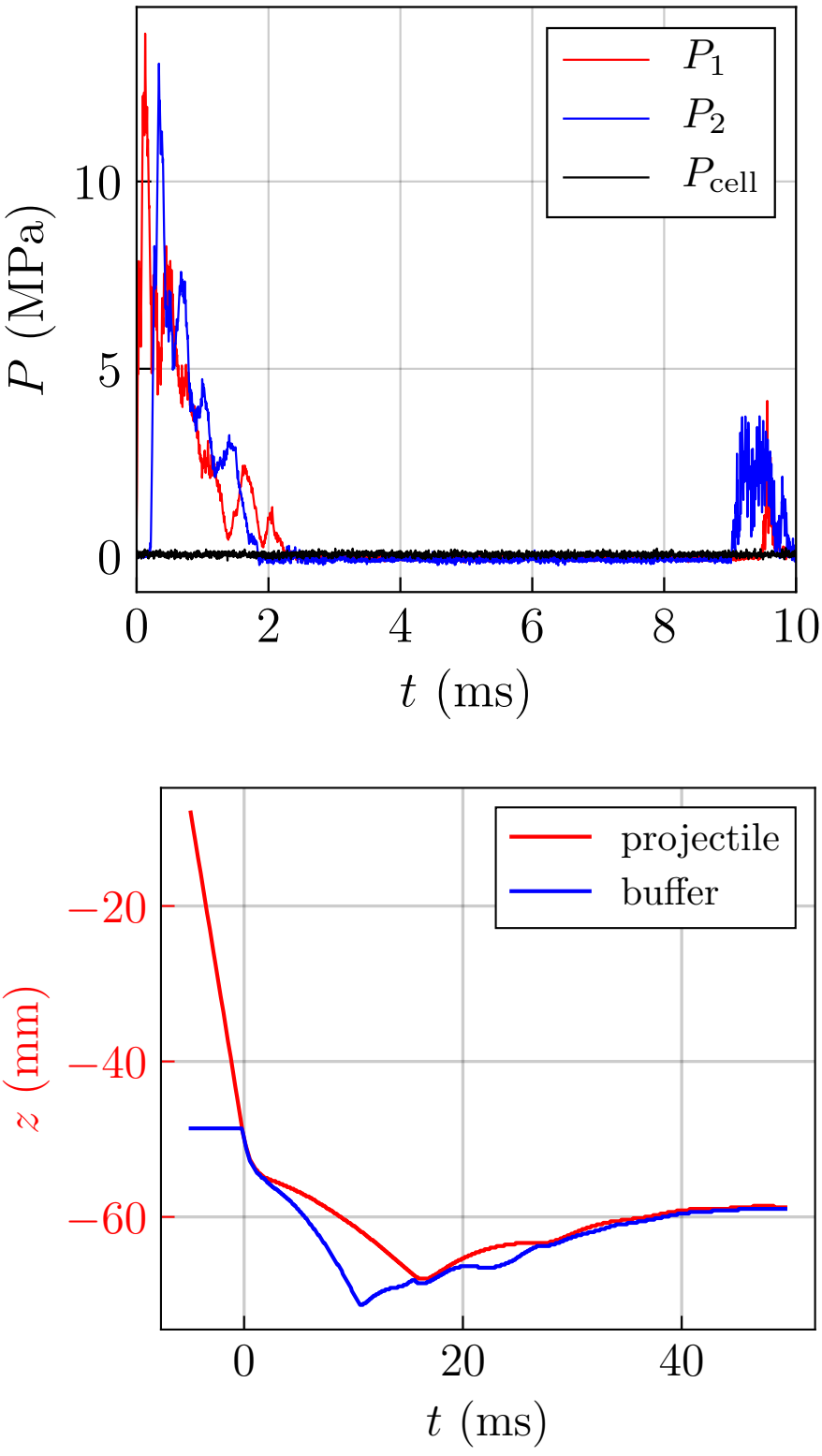

Figure 38: Test B015

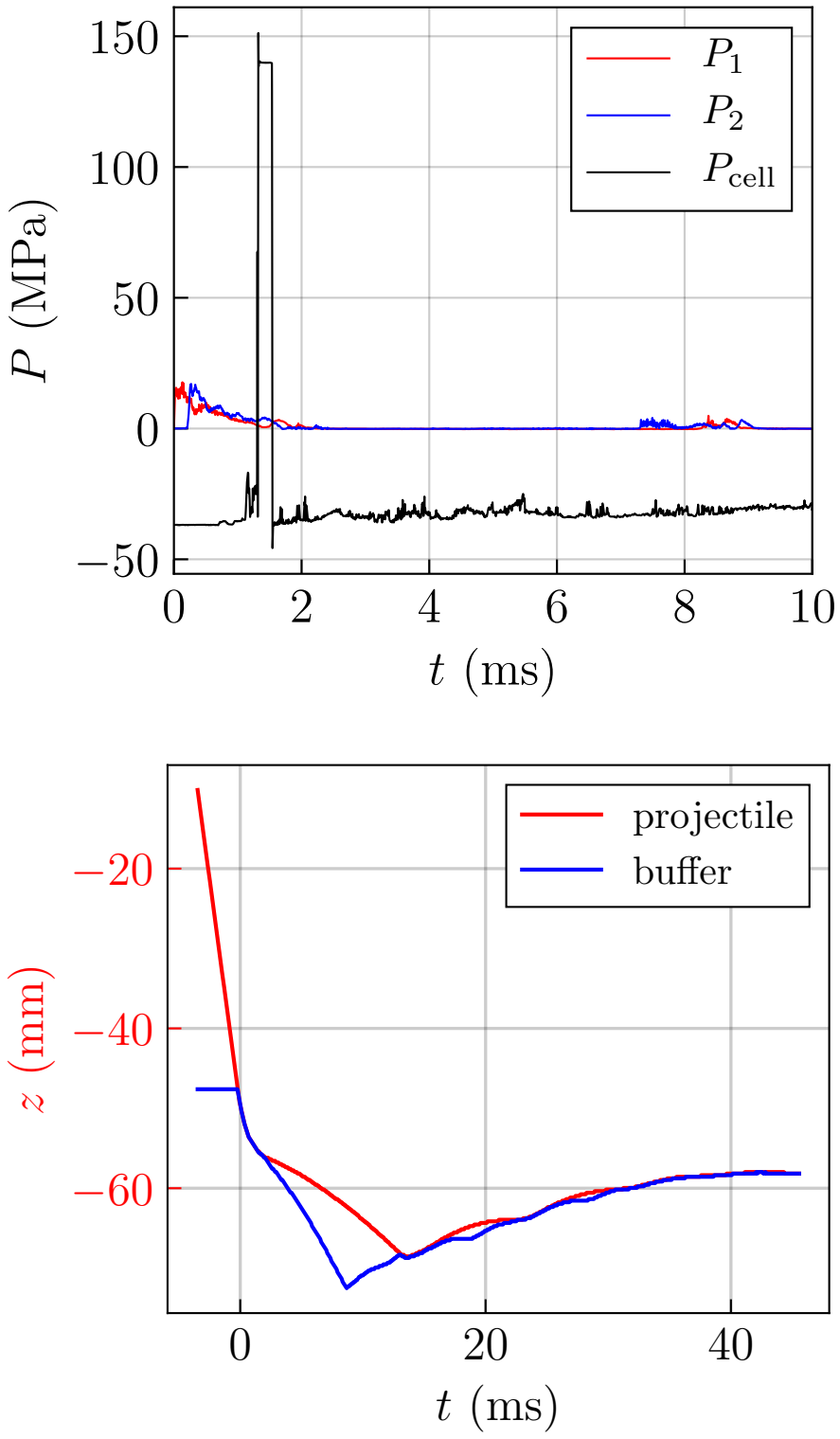

Figure 39: Test B016

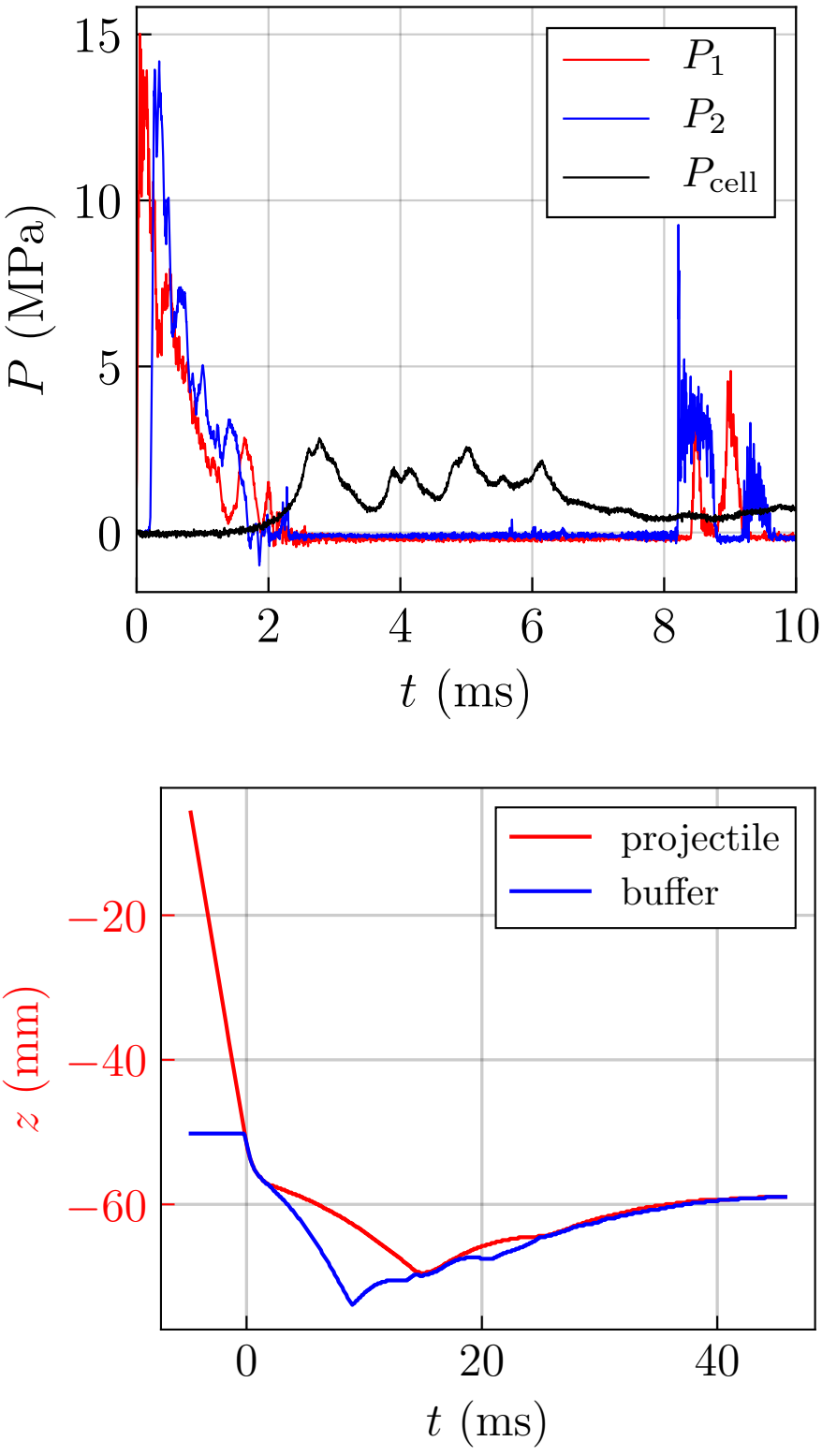

Figure 40: Test B017

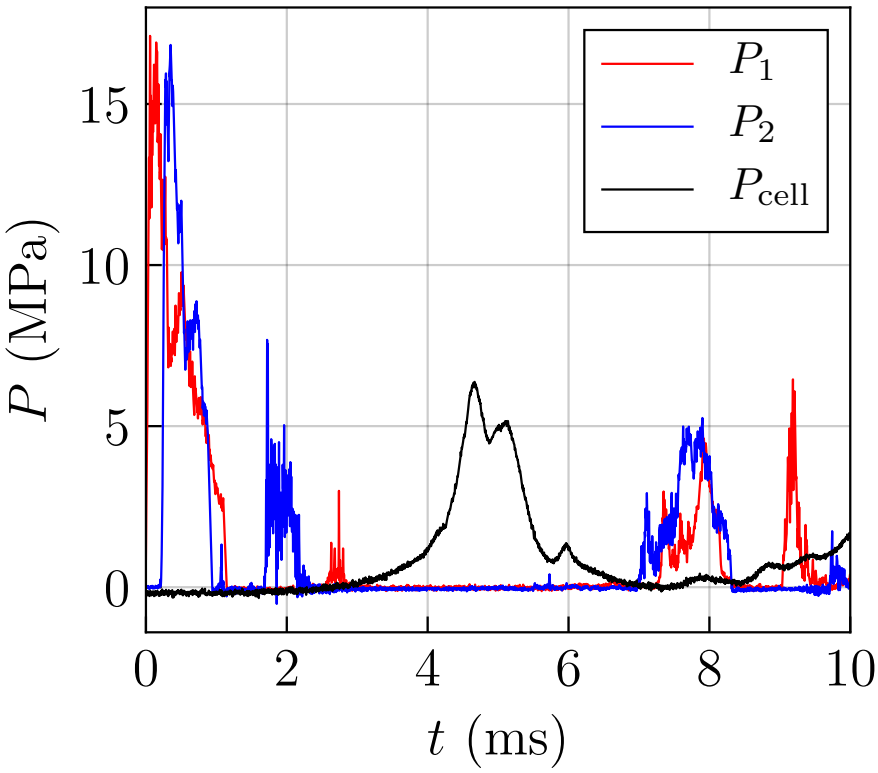

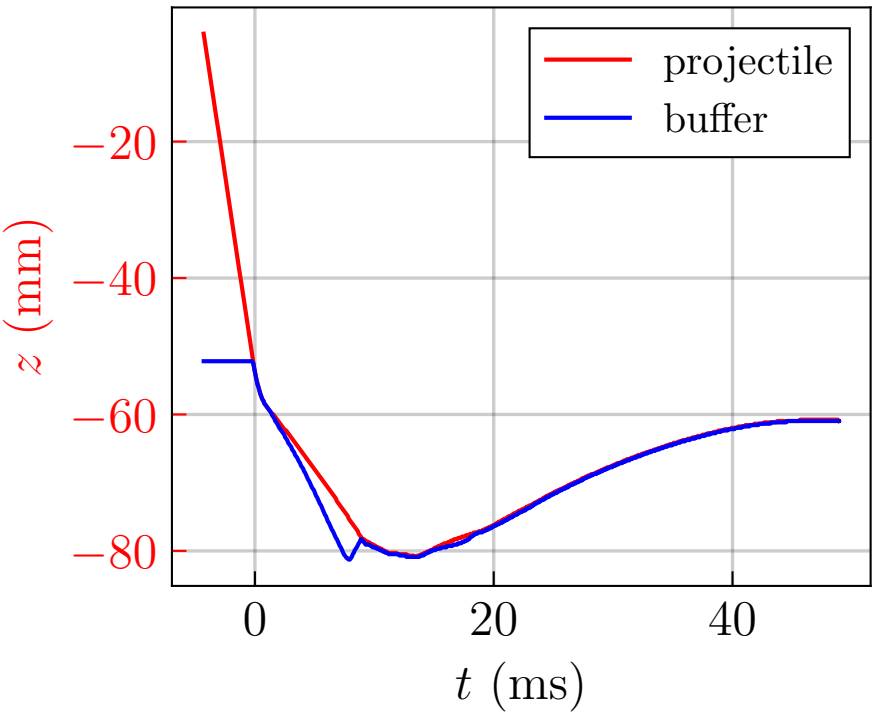

Figure 41: Test B018

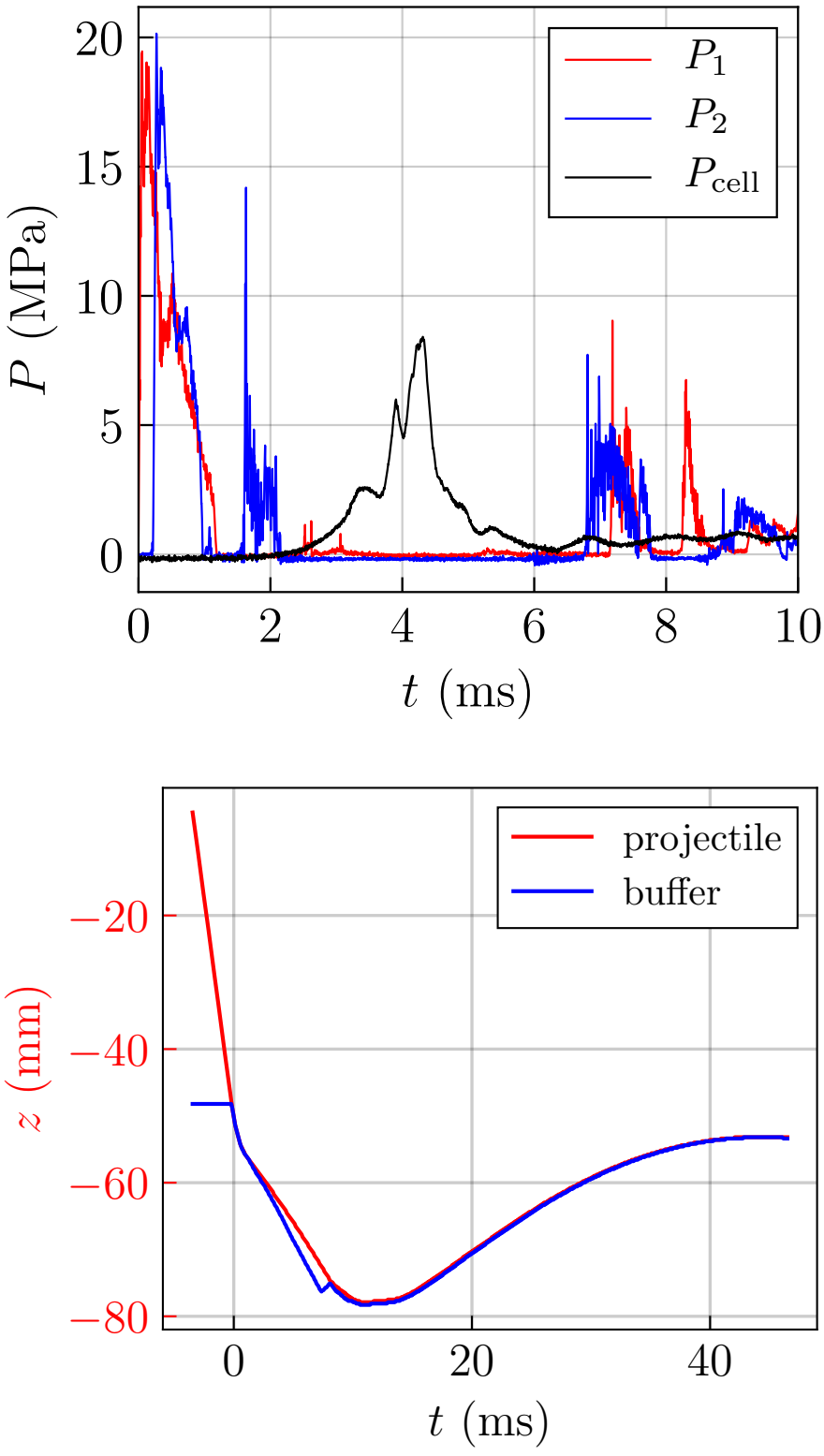

Figure 42: Test B019

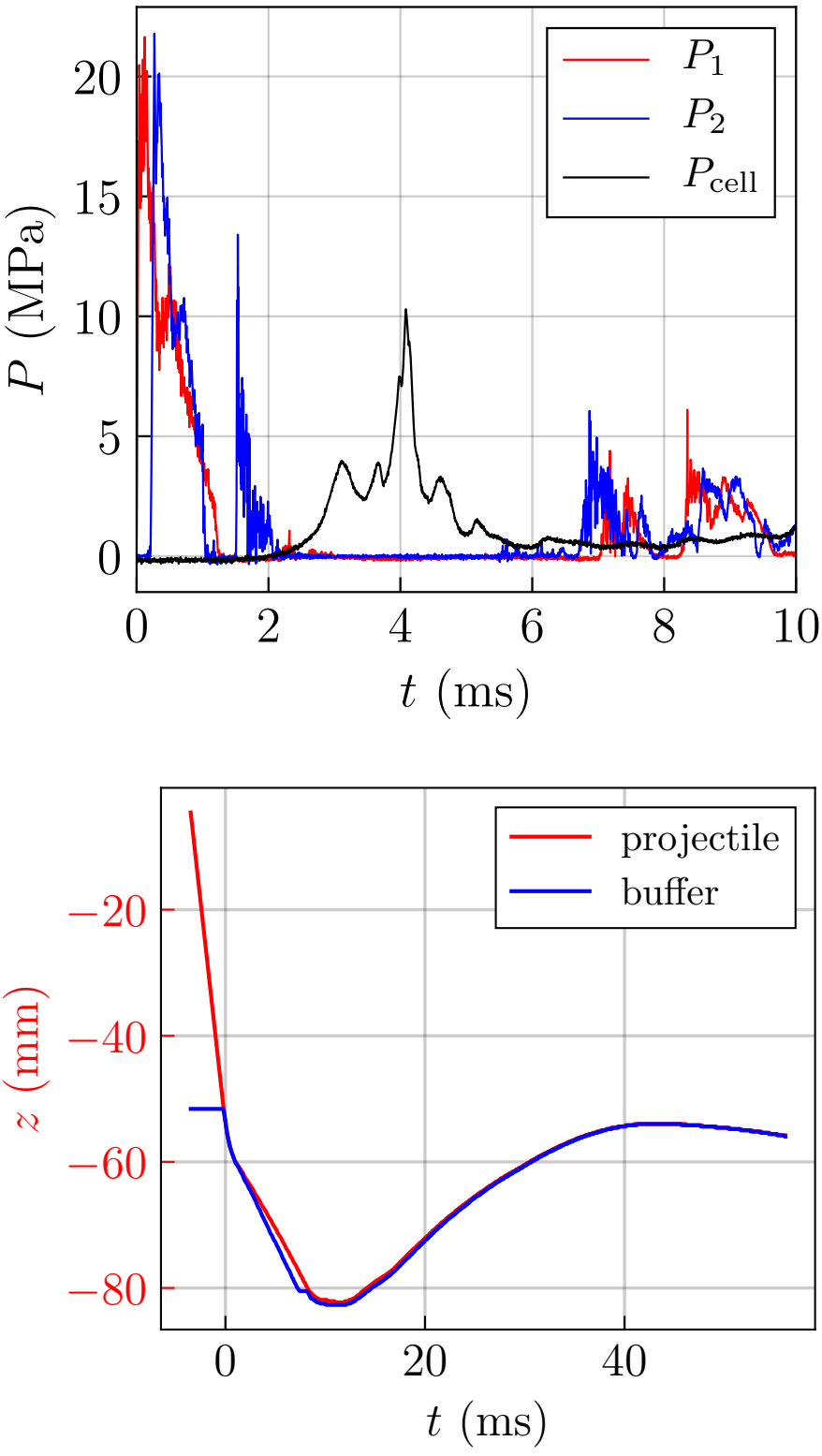

Figure 43: Test B020

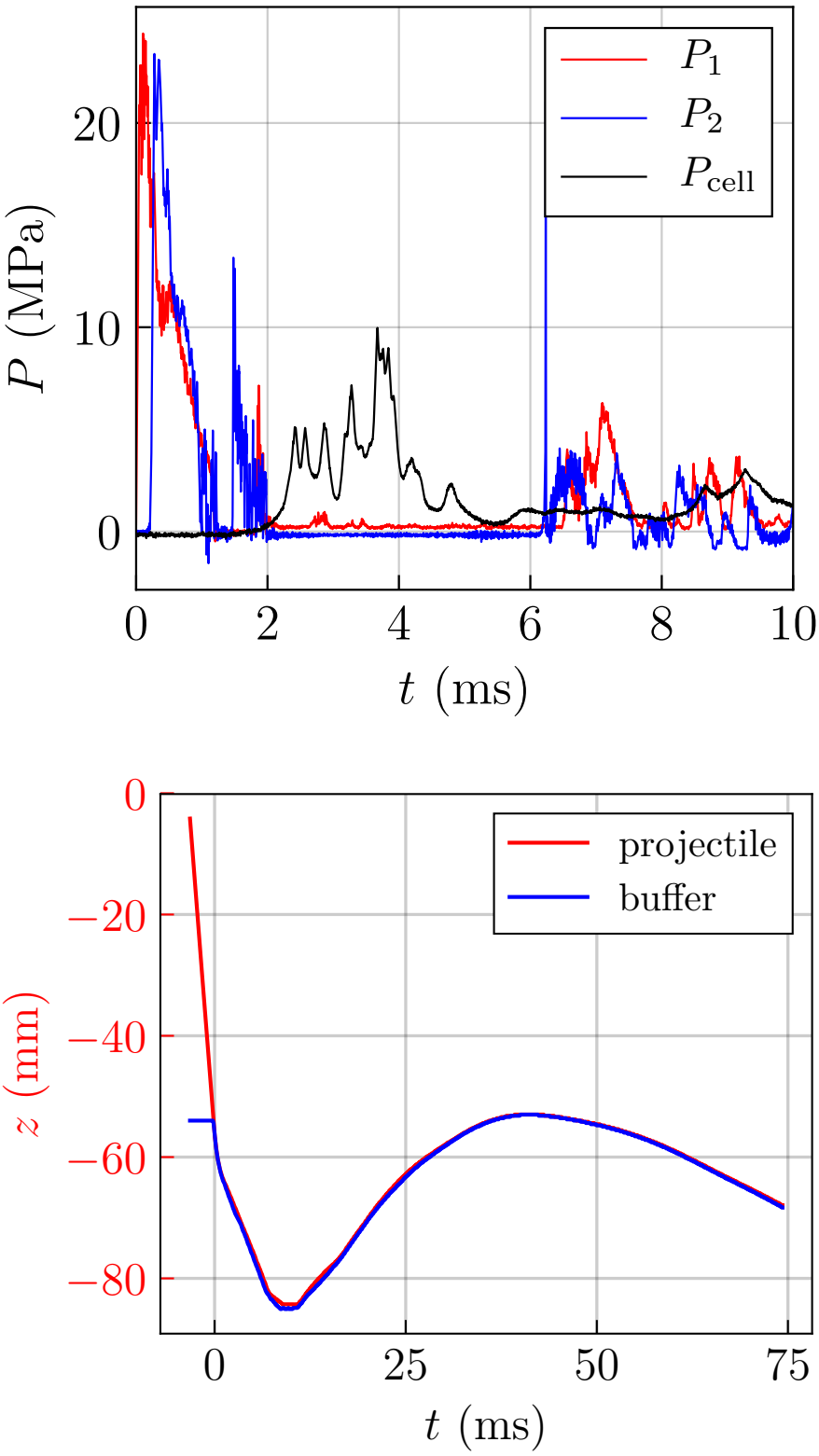

Figure 44: Test B021

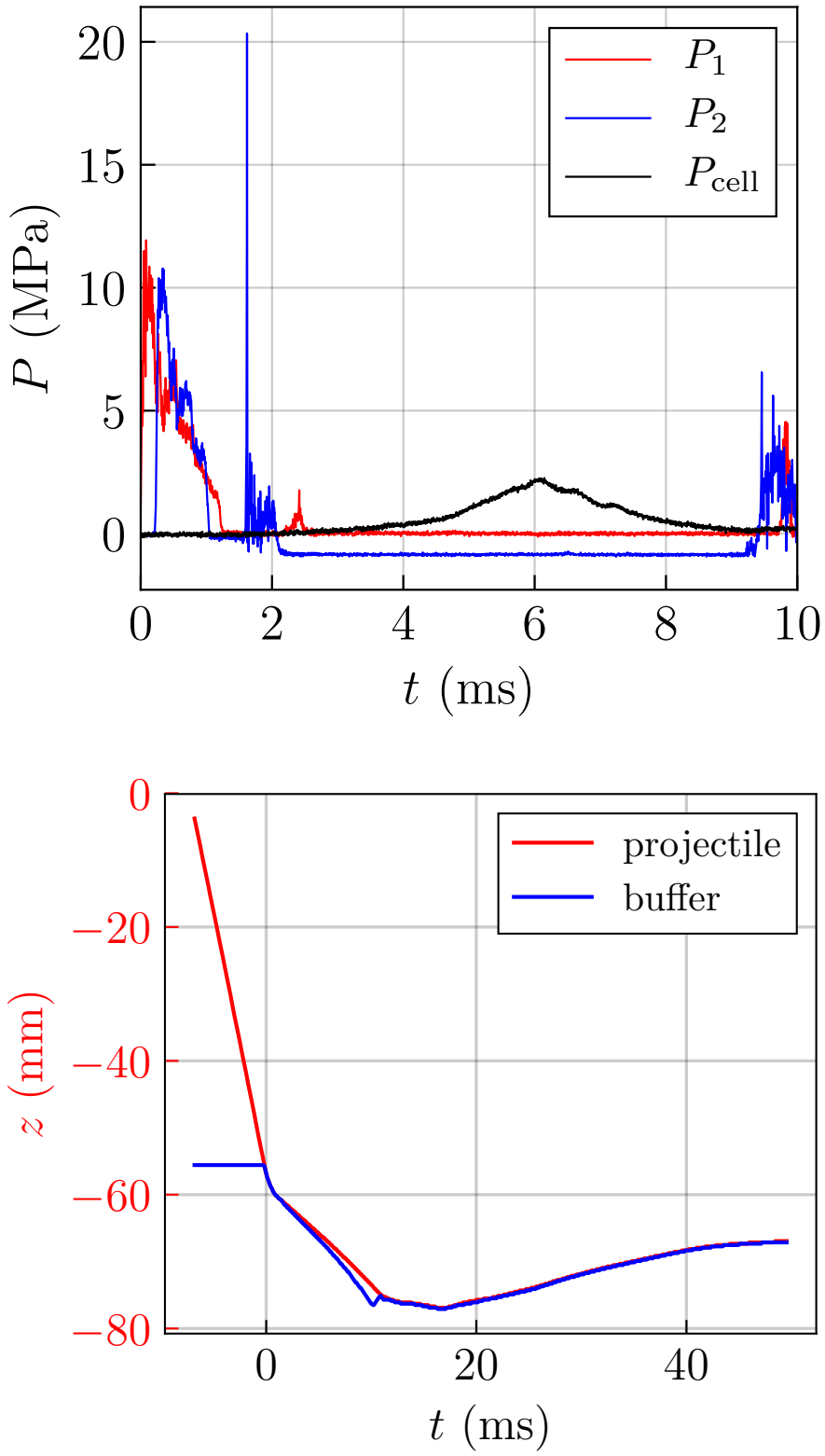

Figure 45: Test B022

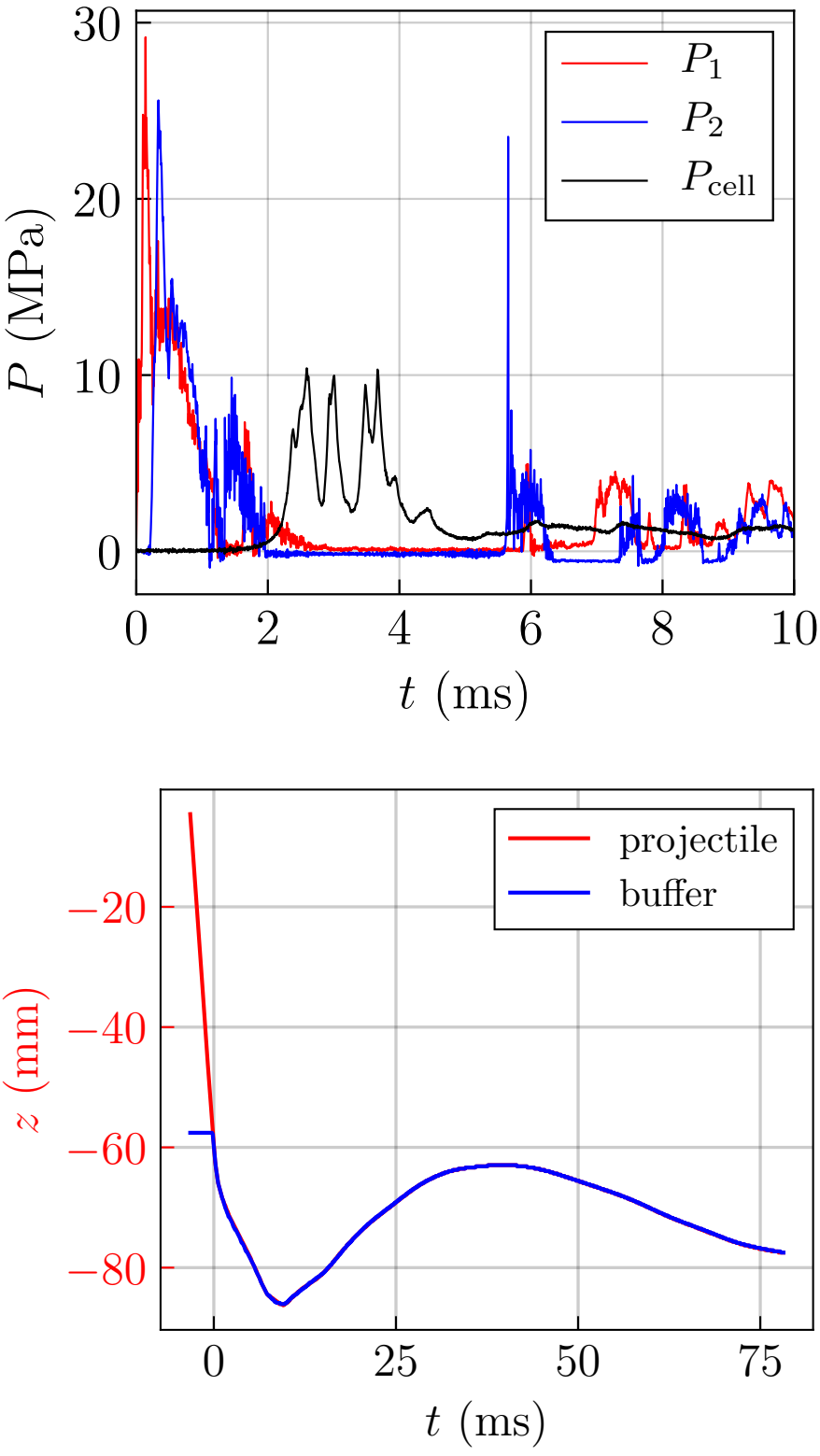

Figure 46: Test B023

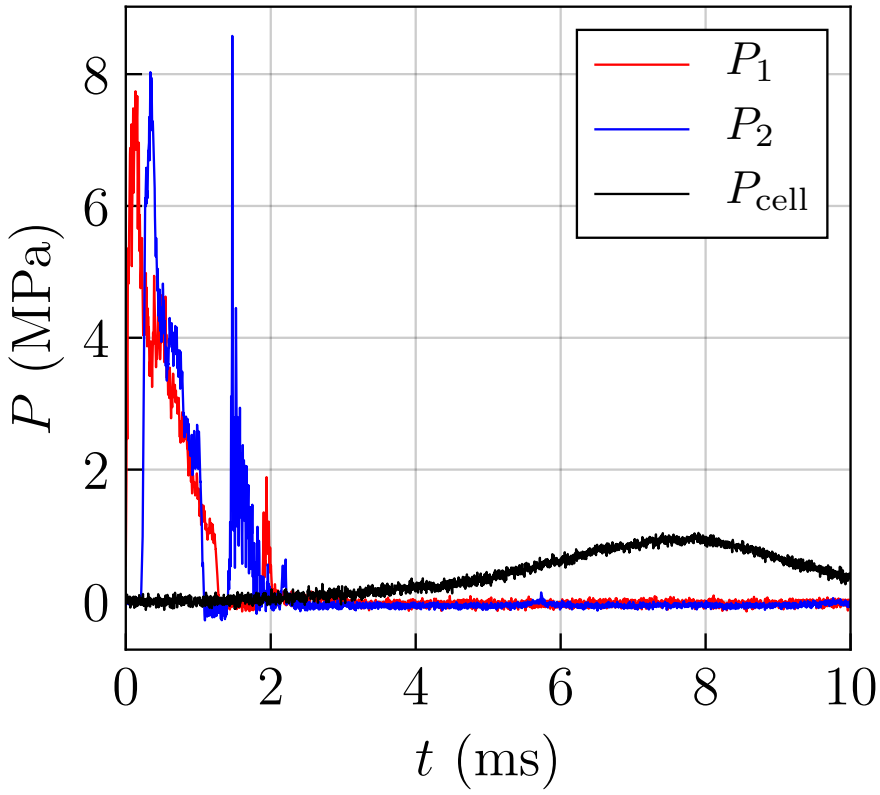

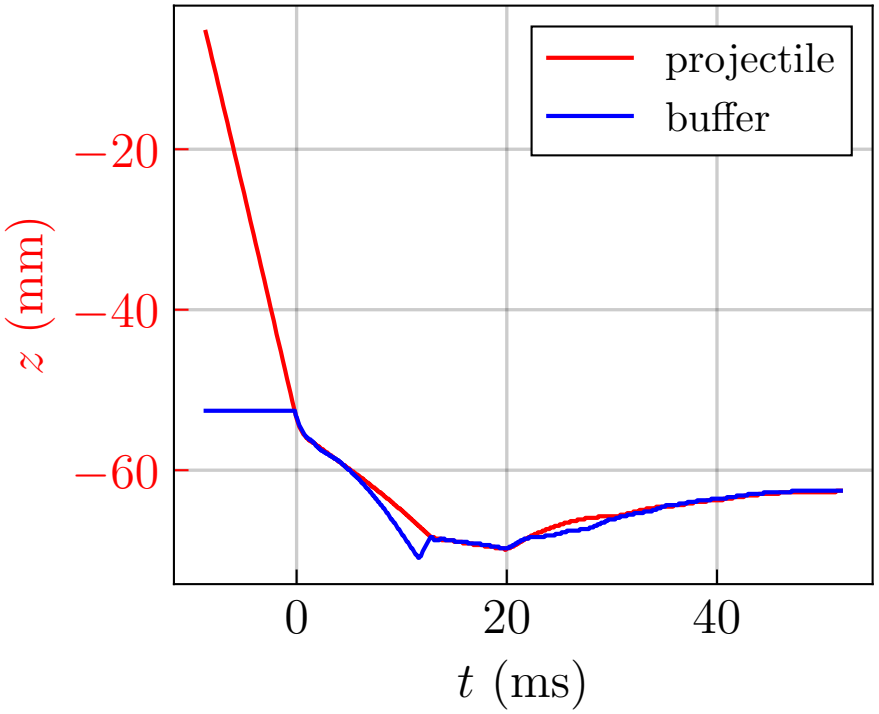

Figure 47: Test B024

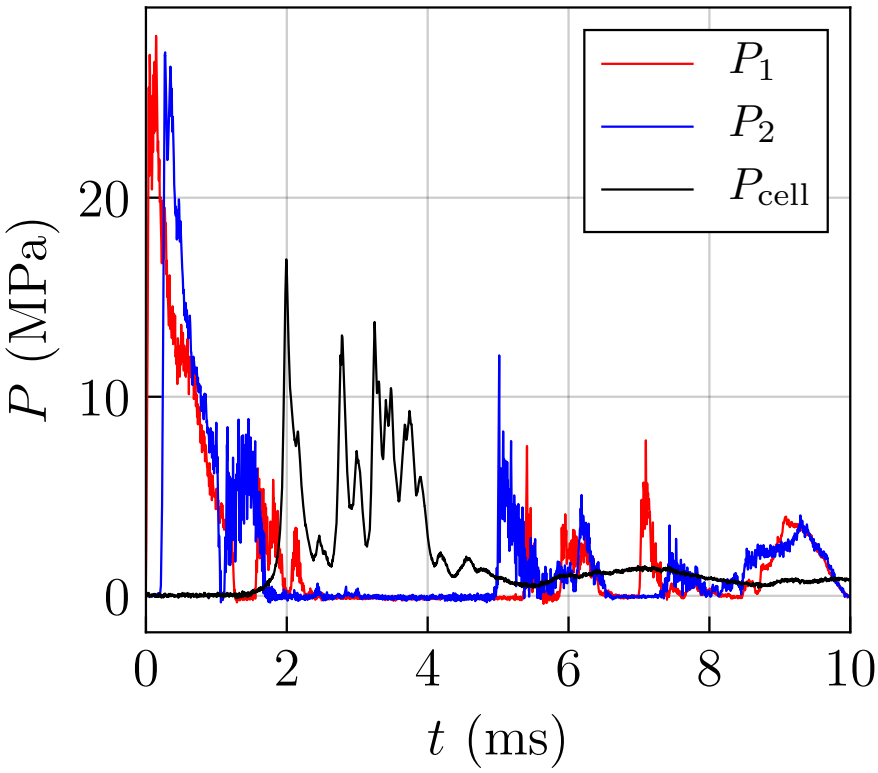

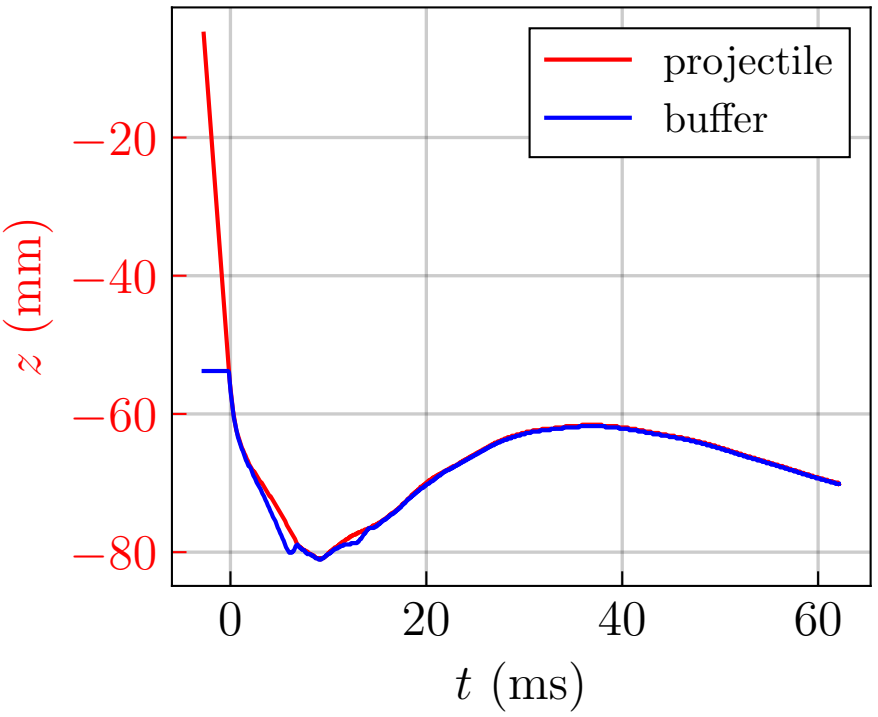

Figure 48: Test B025

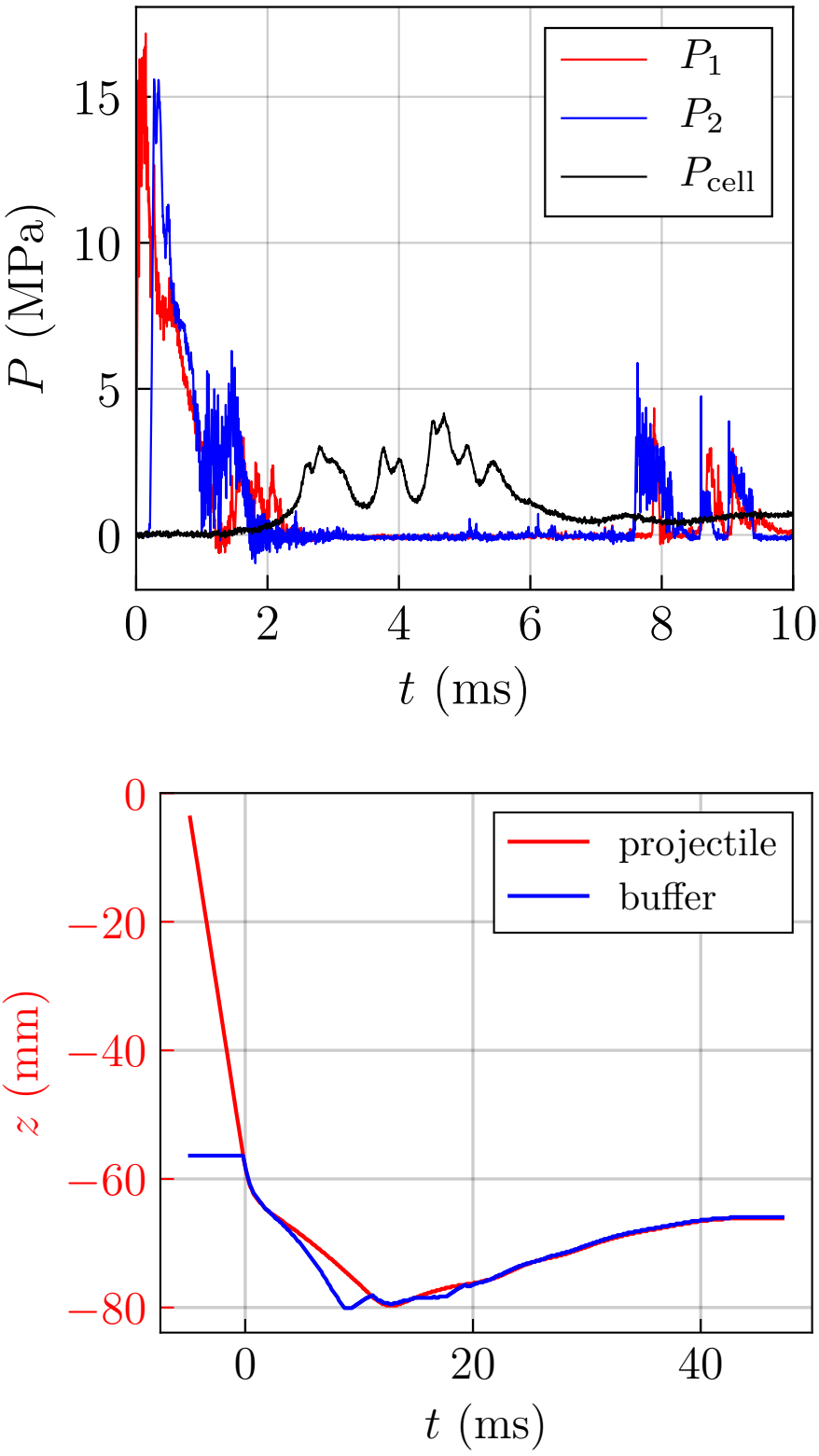

Figure 49: Test B026

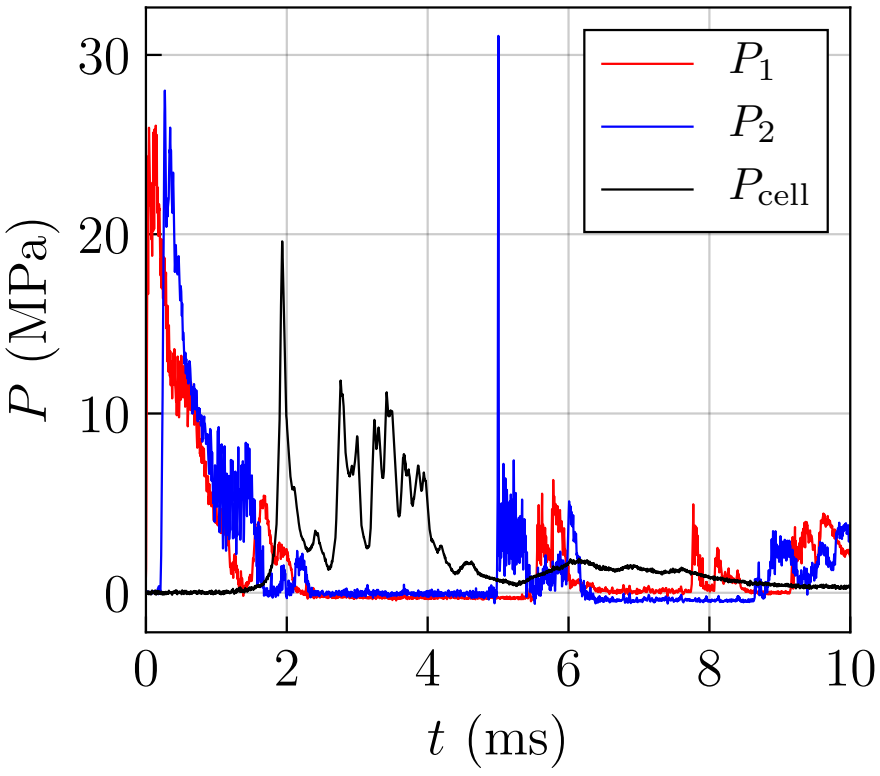

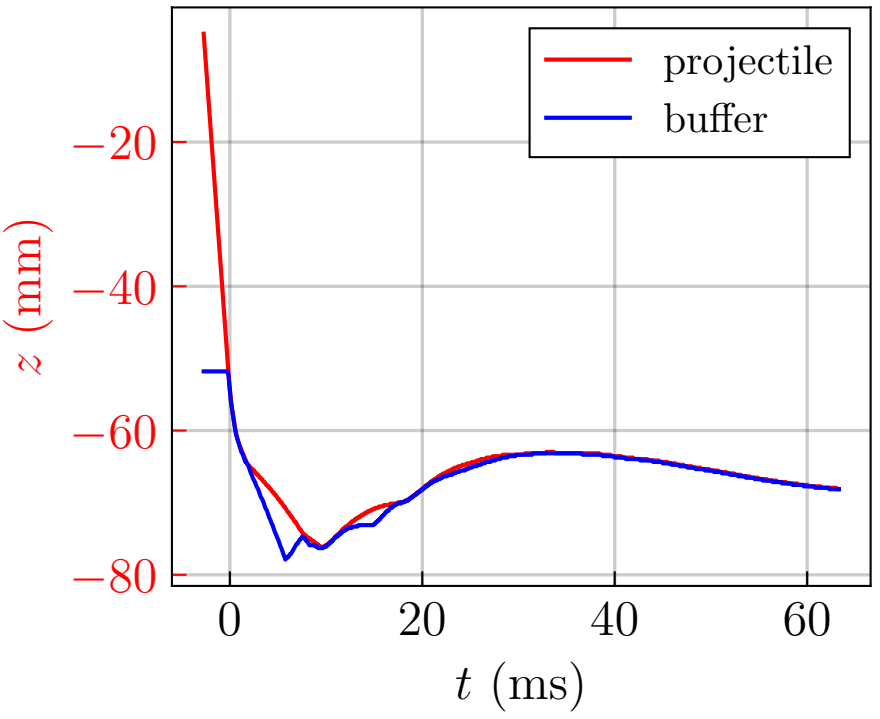

Figure 50: Test B027

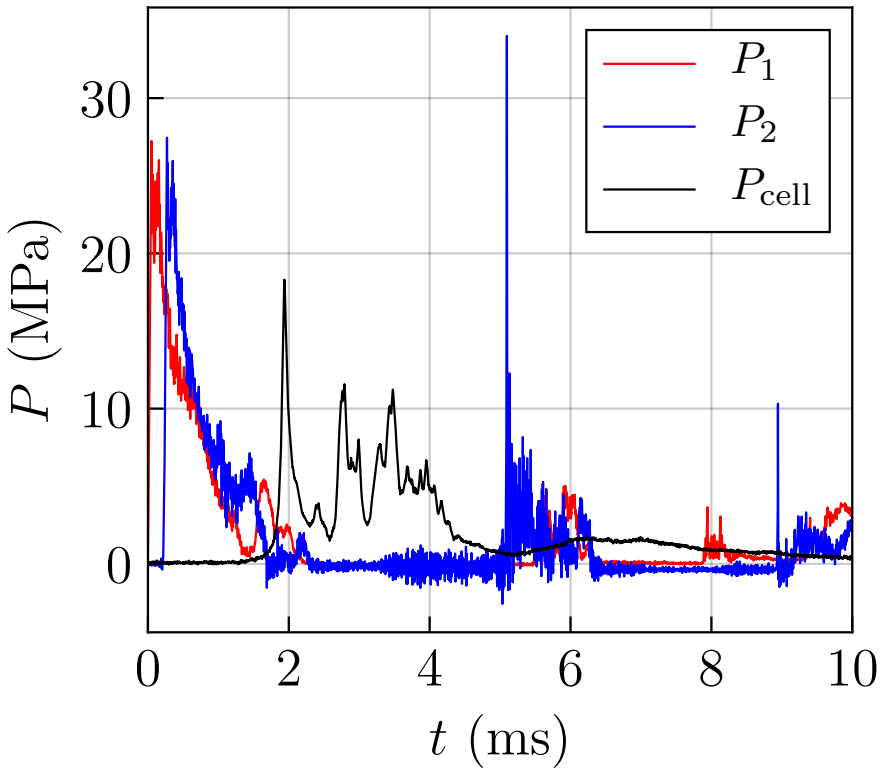

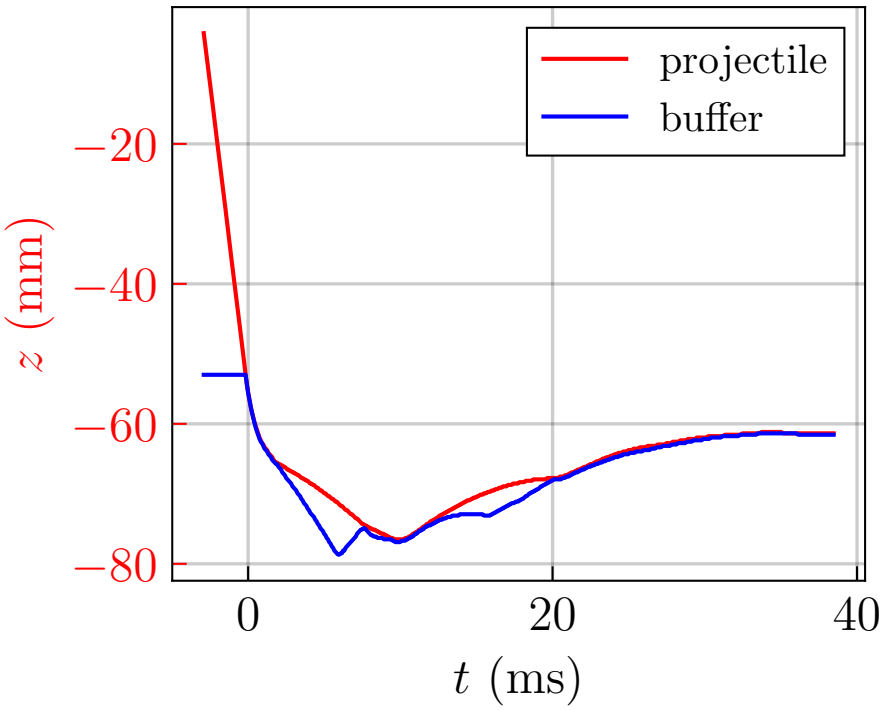

Figure 51: Test B028

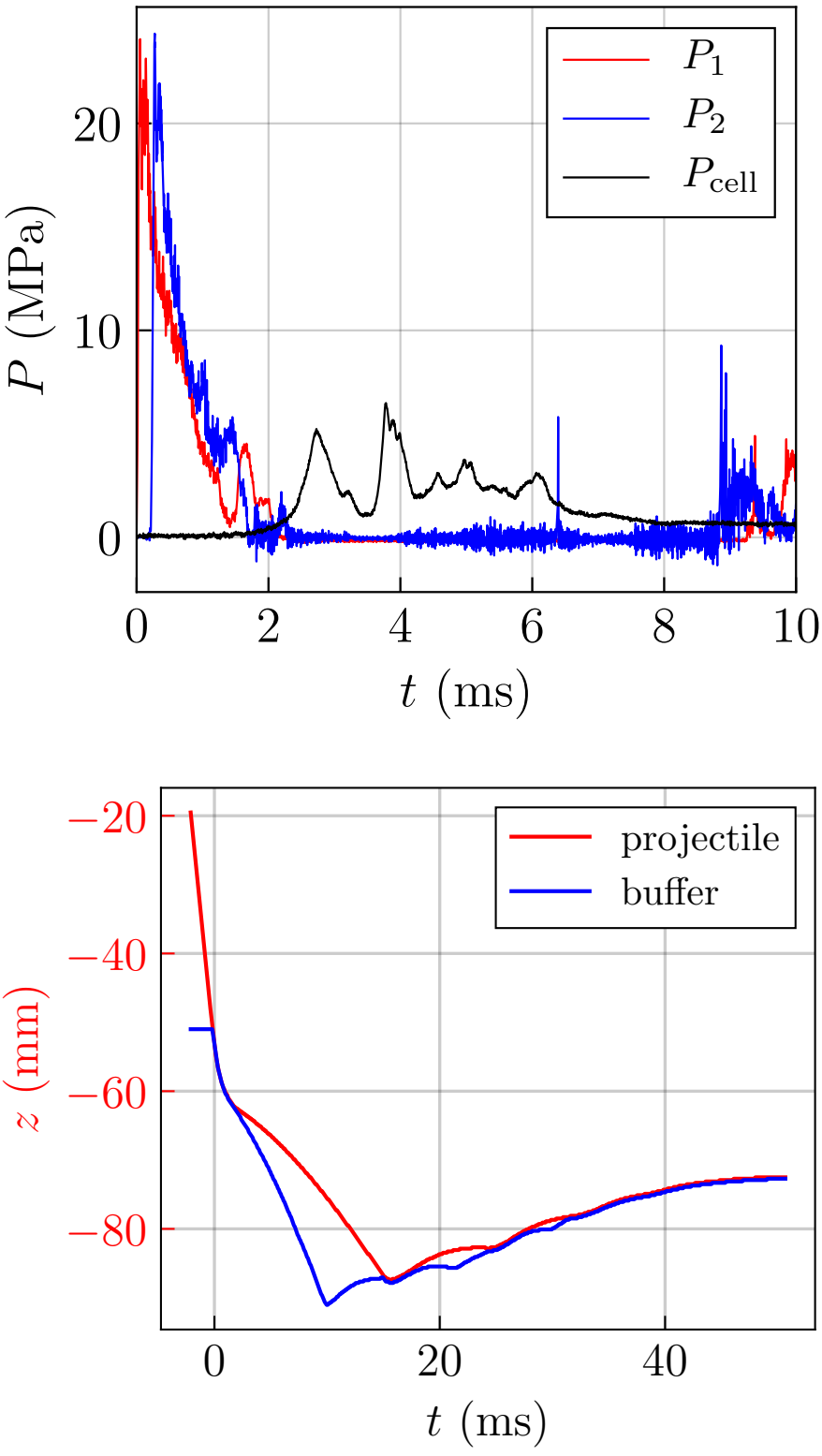

Figure 52: Test B029

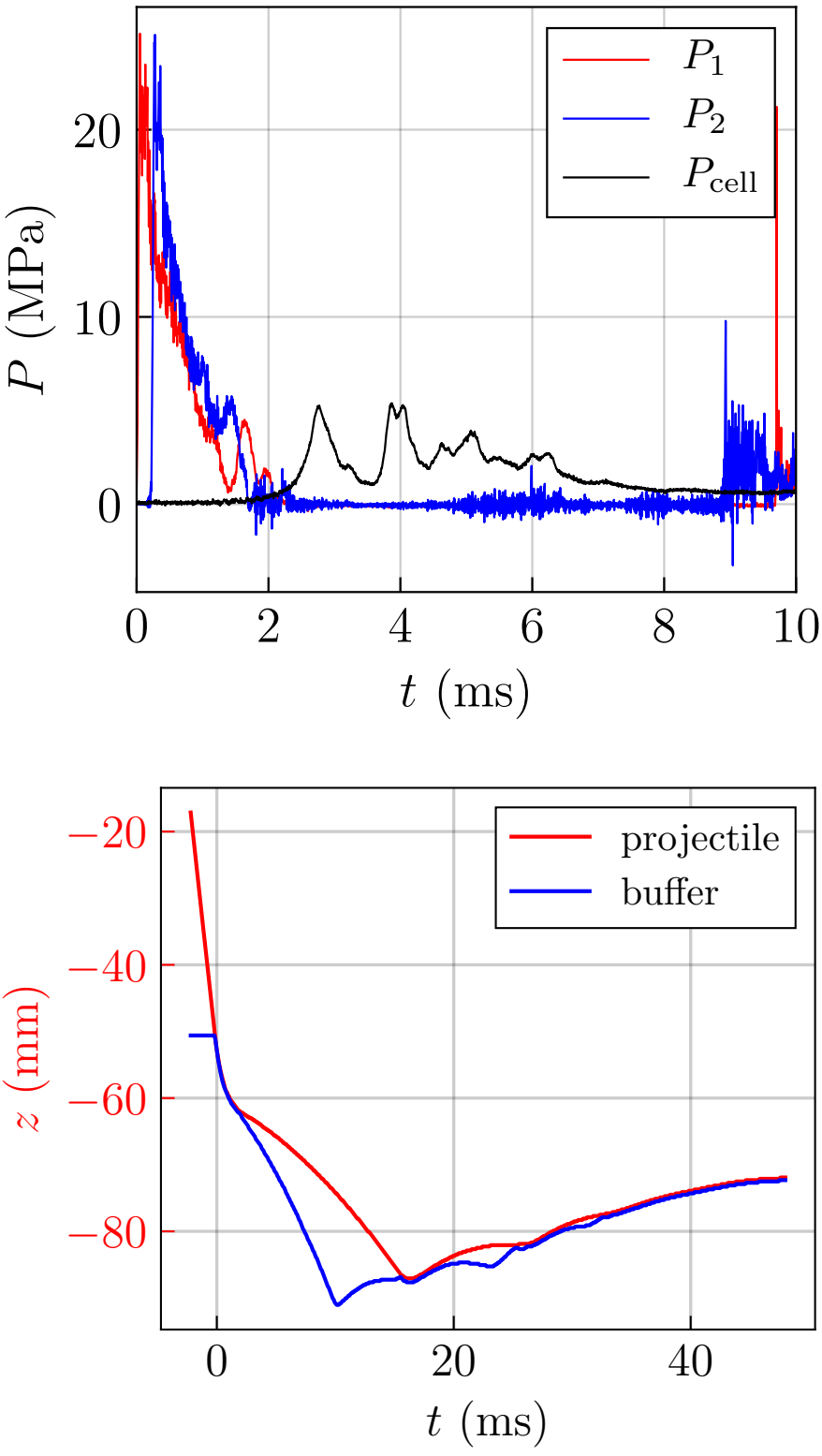

Figure 53: Test B030

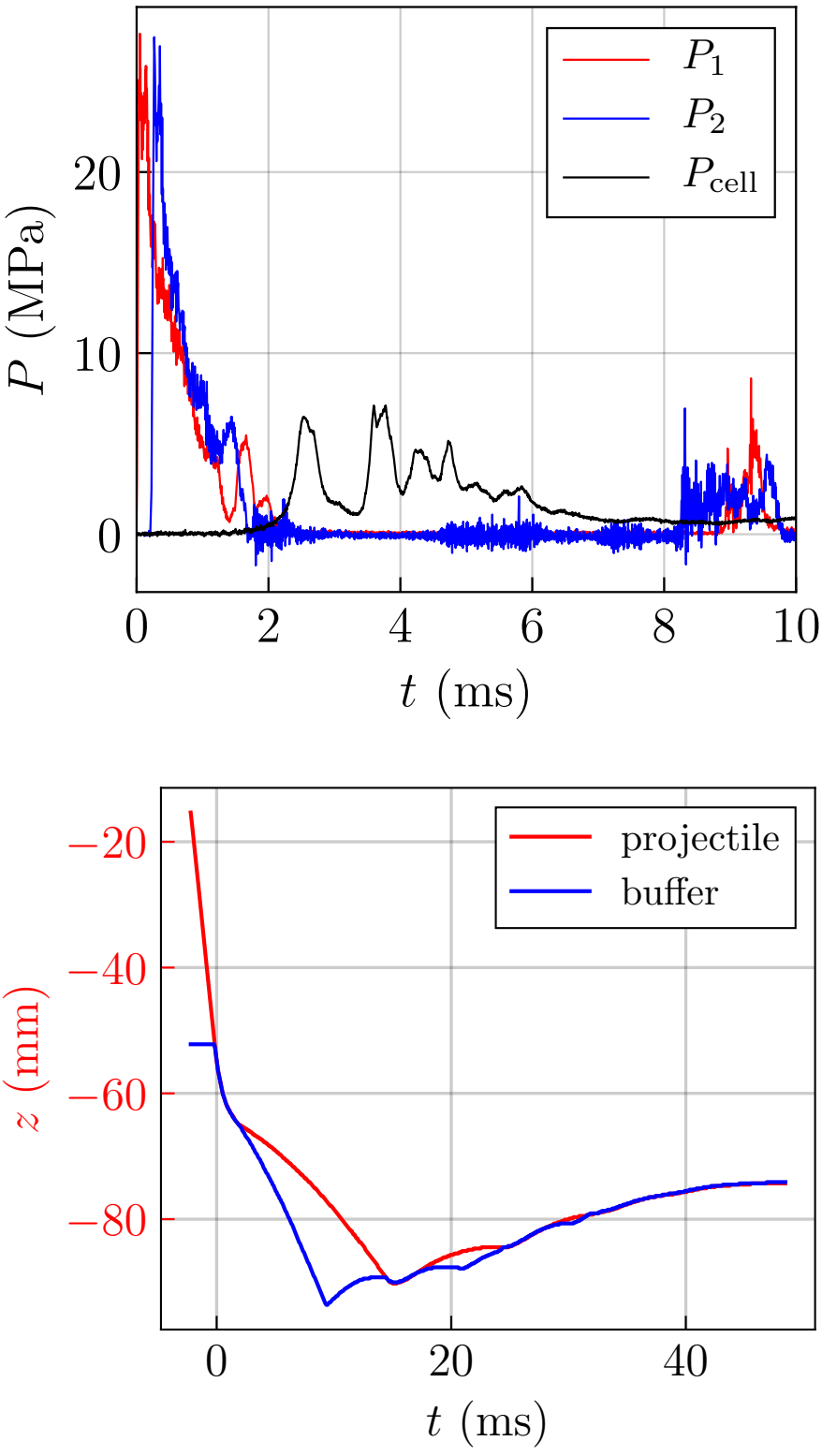

Figure 54: Test B031

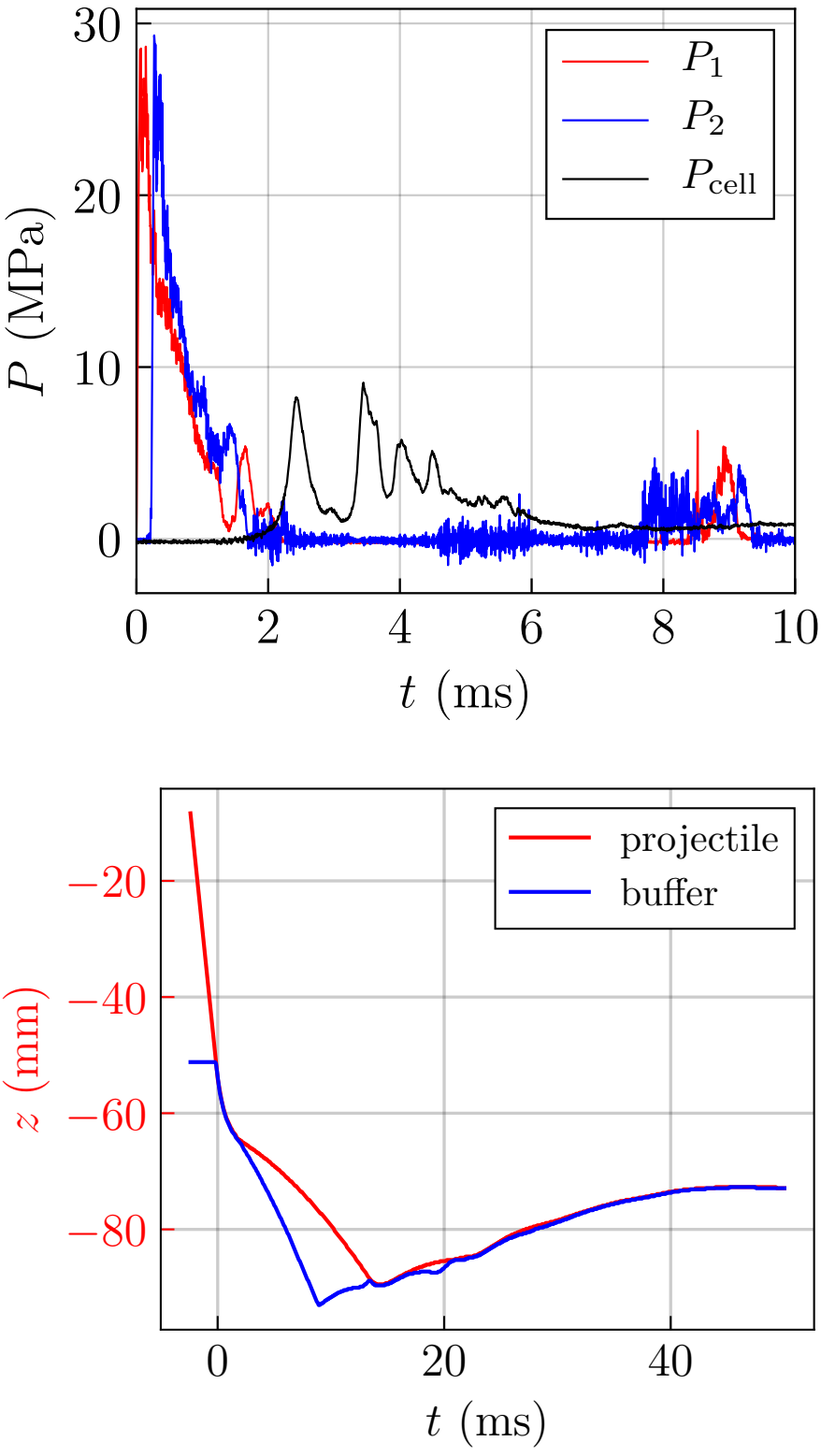

Figure 55: Test B032

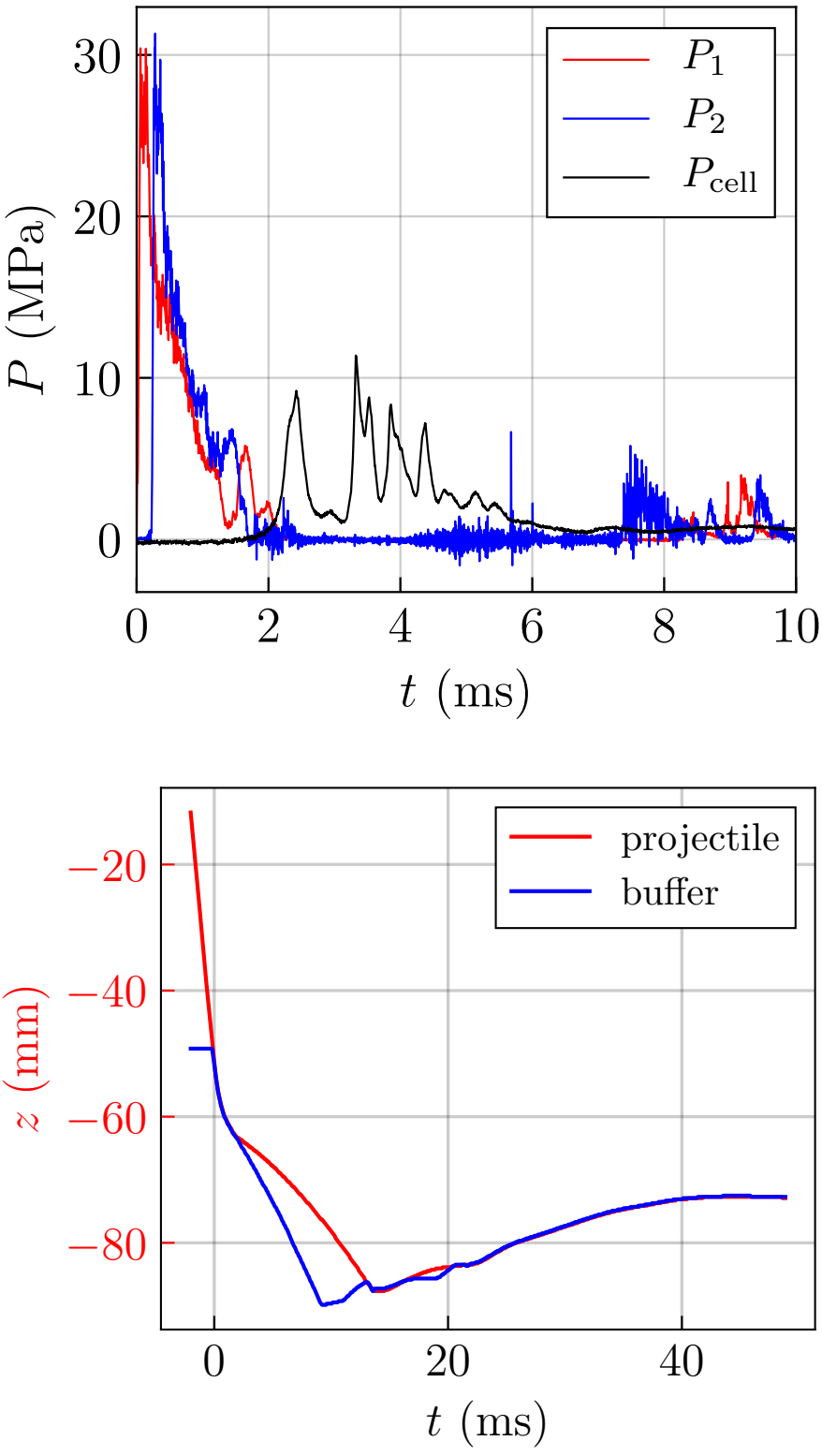

Figure 56: Test B033

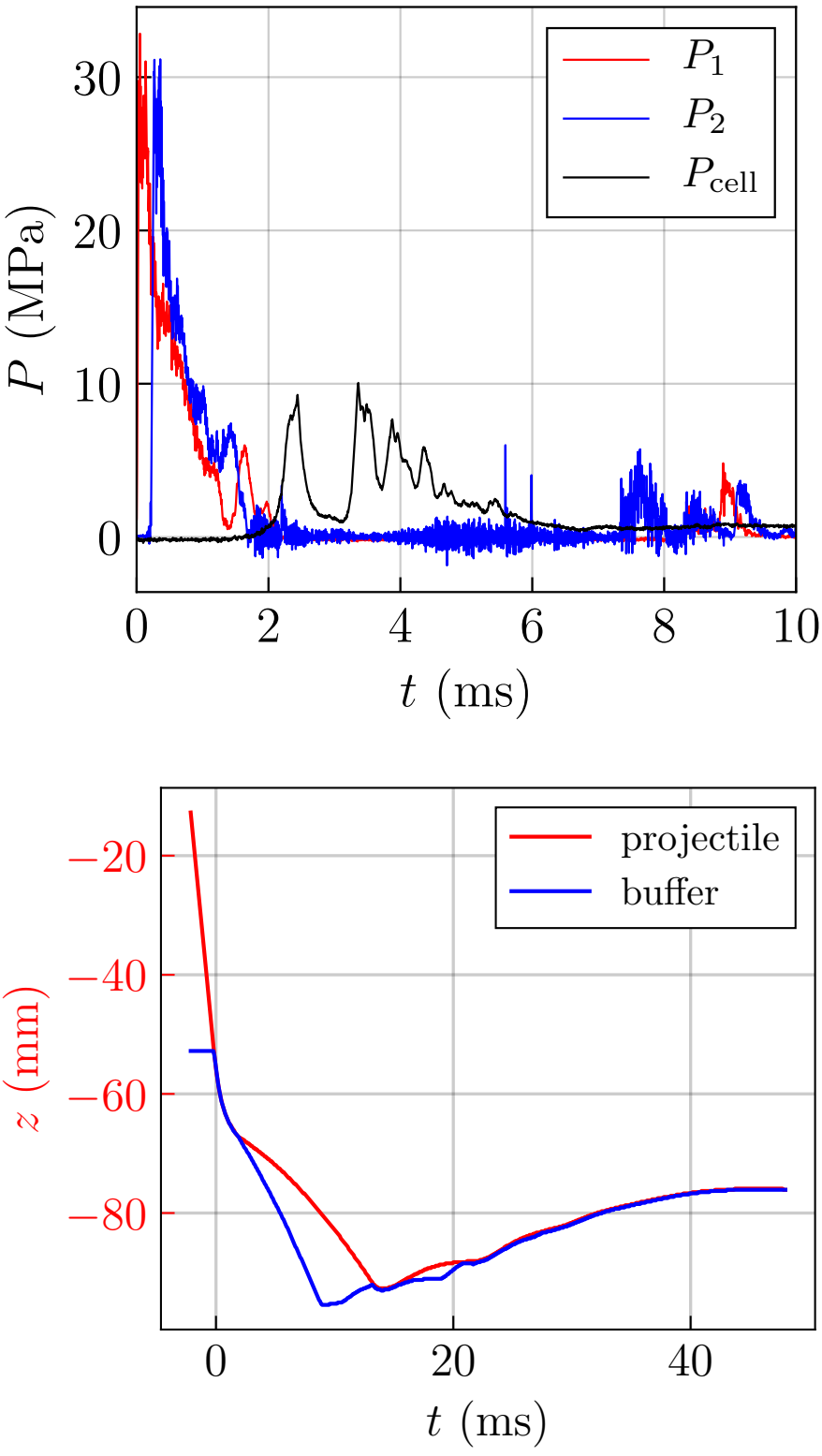

Figure 57: Test B034

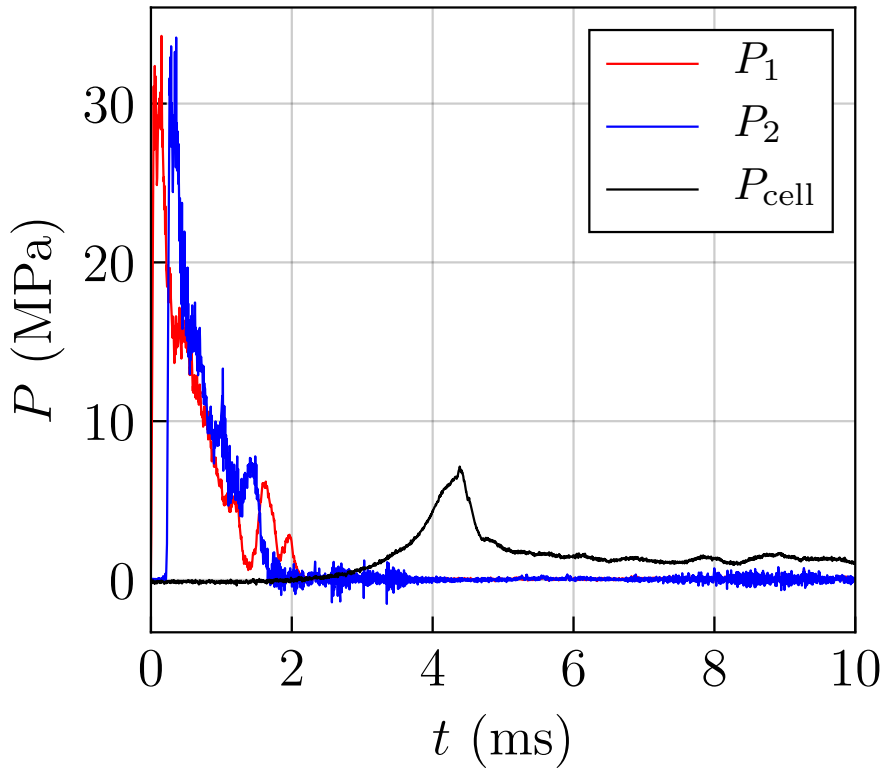

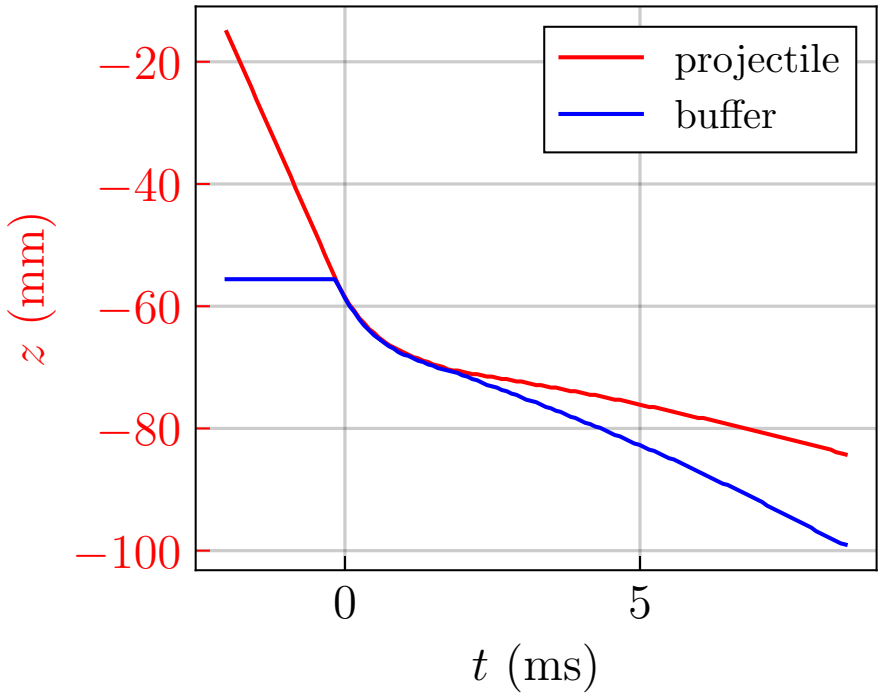

Figure 58: Test B035

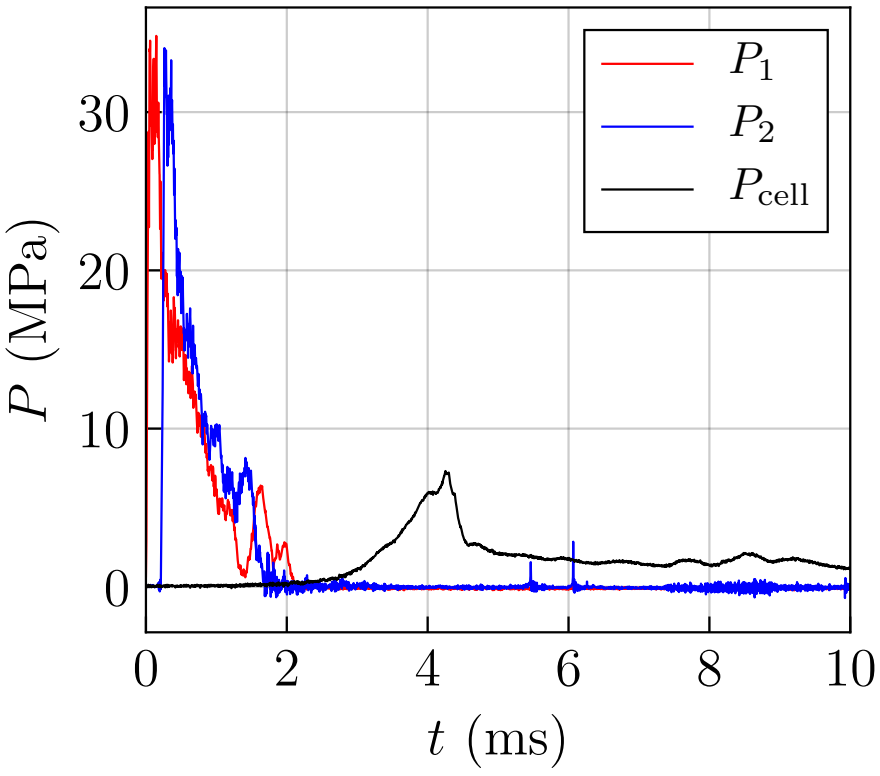

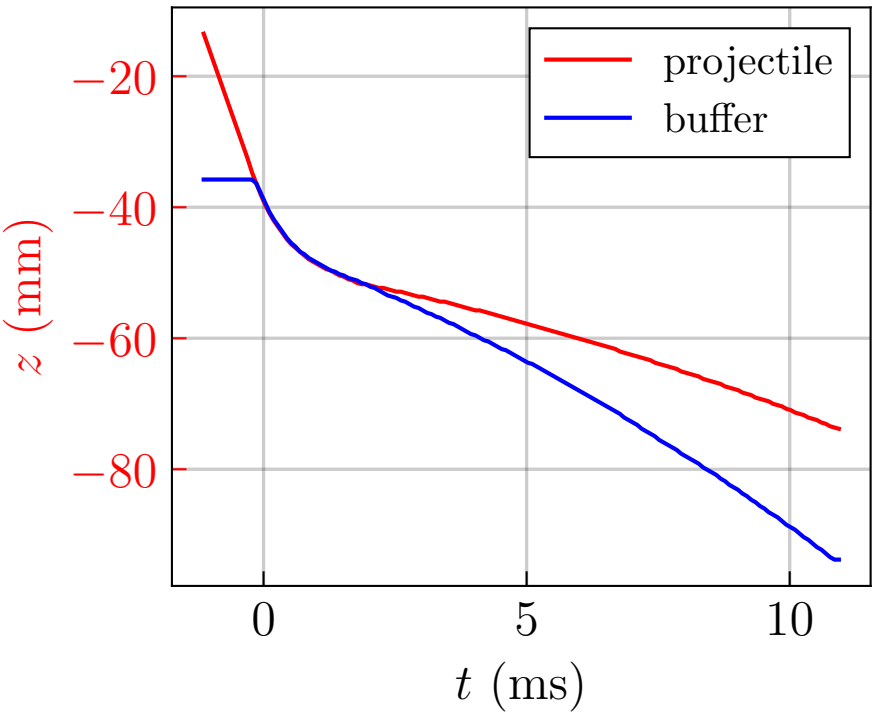

Figure 59: Test B036

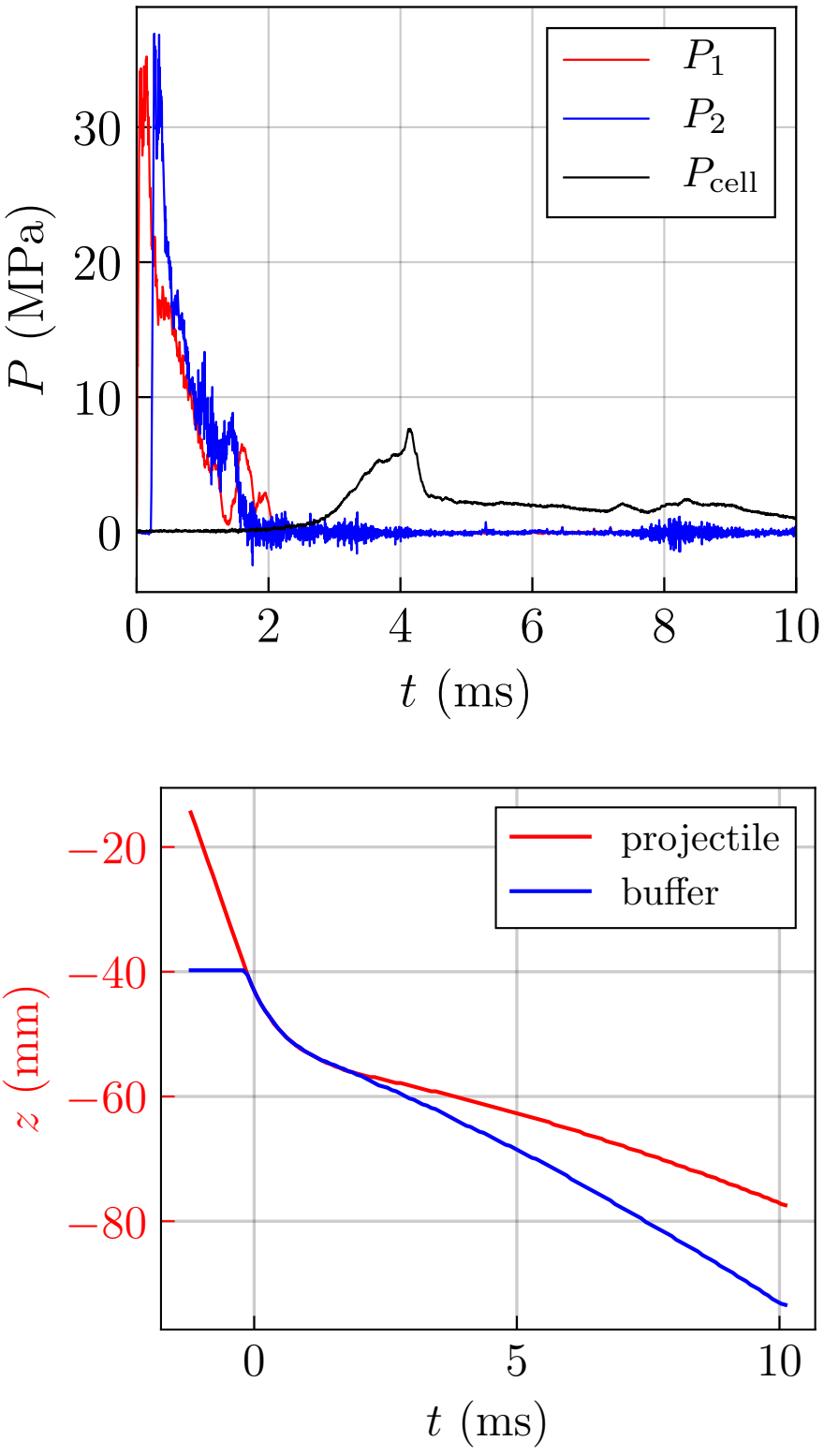

Figure 60: Test B037

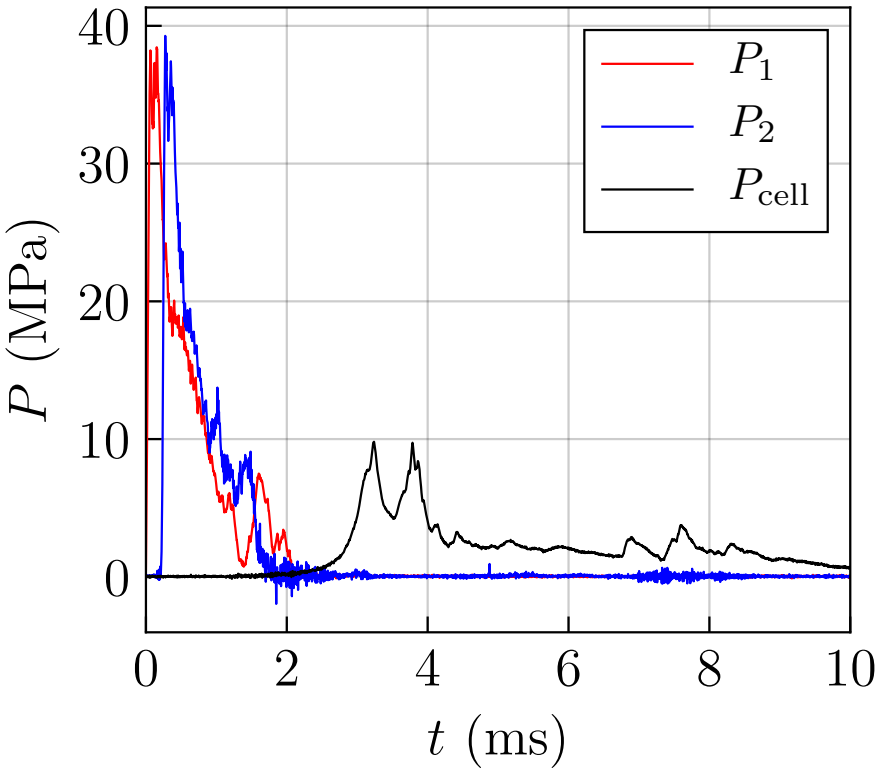

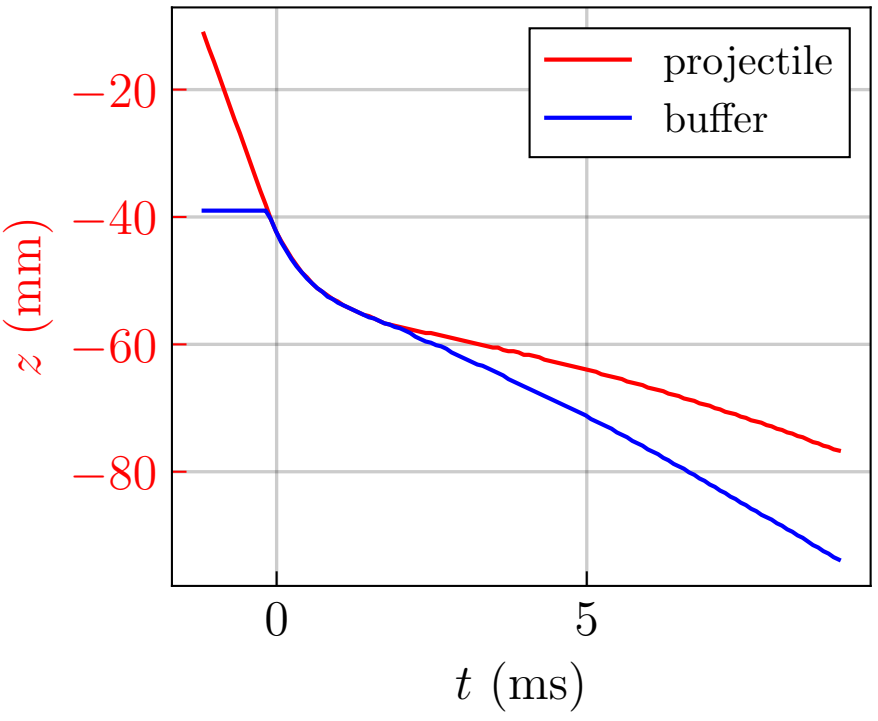

Figure 61: Test B038

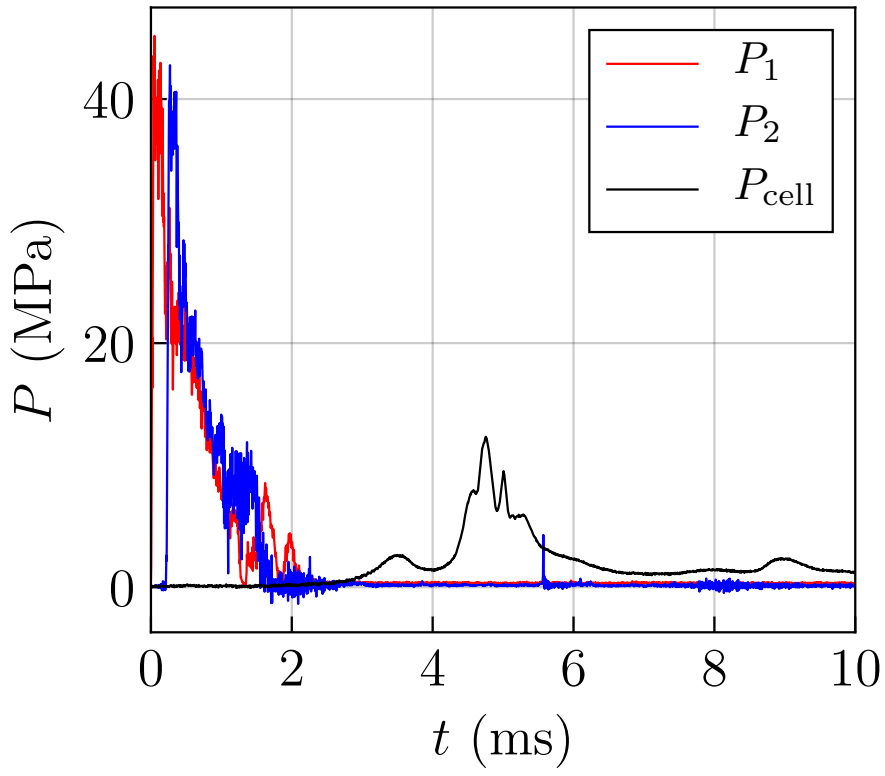

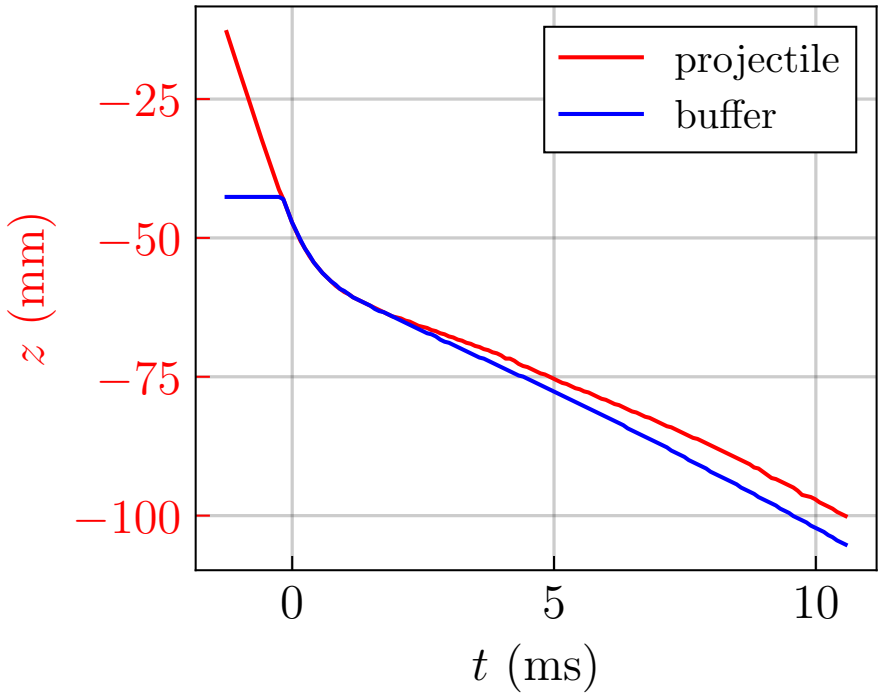

Figure 62: Test B039

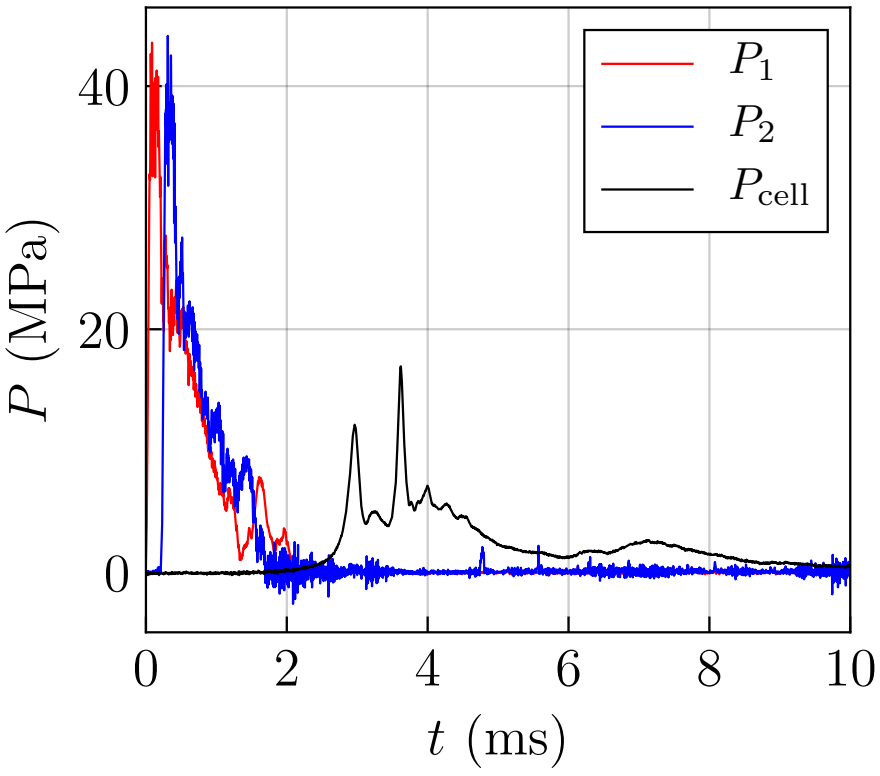

Figure 63: Test B040

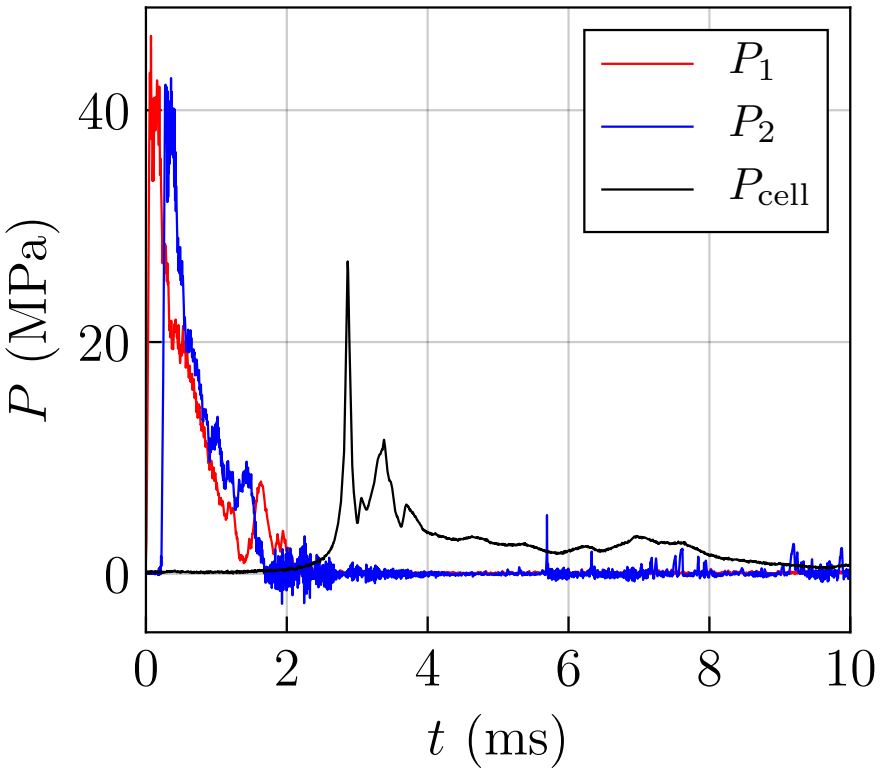

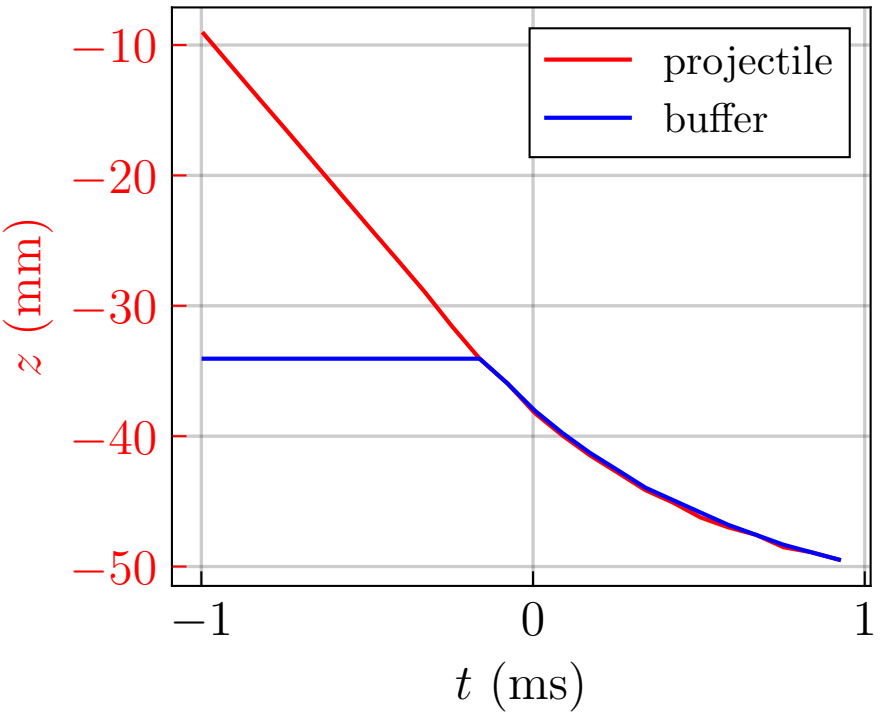

Figure 64: Test B041

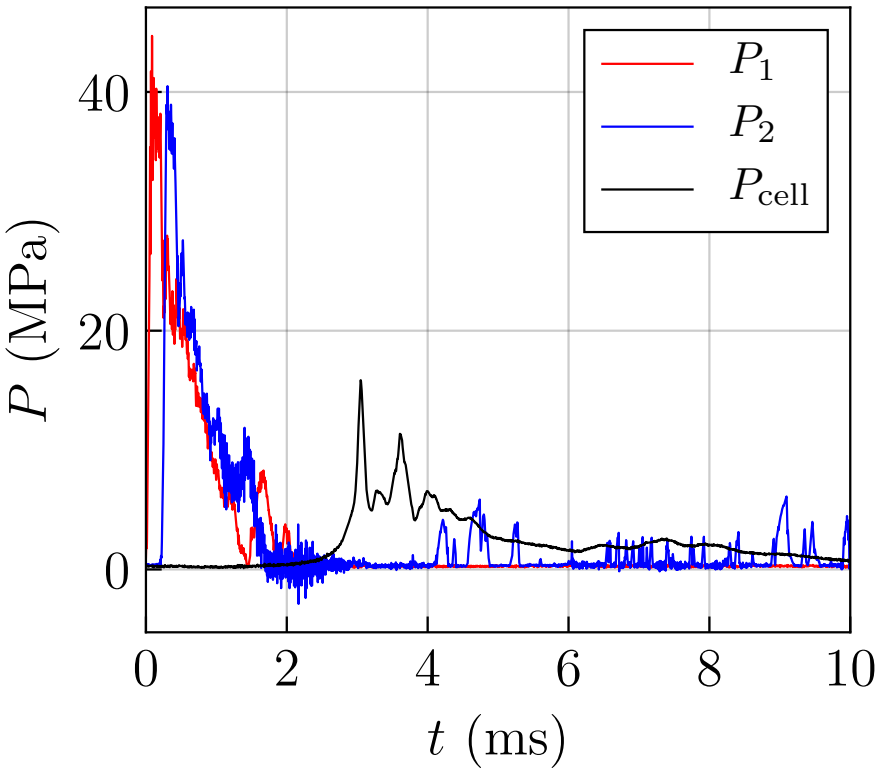

Figure 65: Test B042

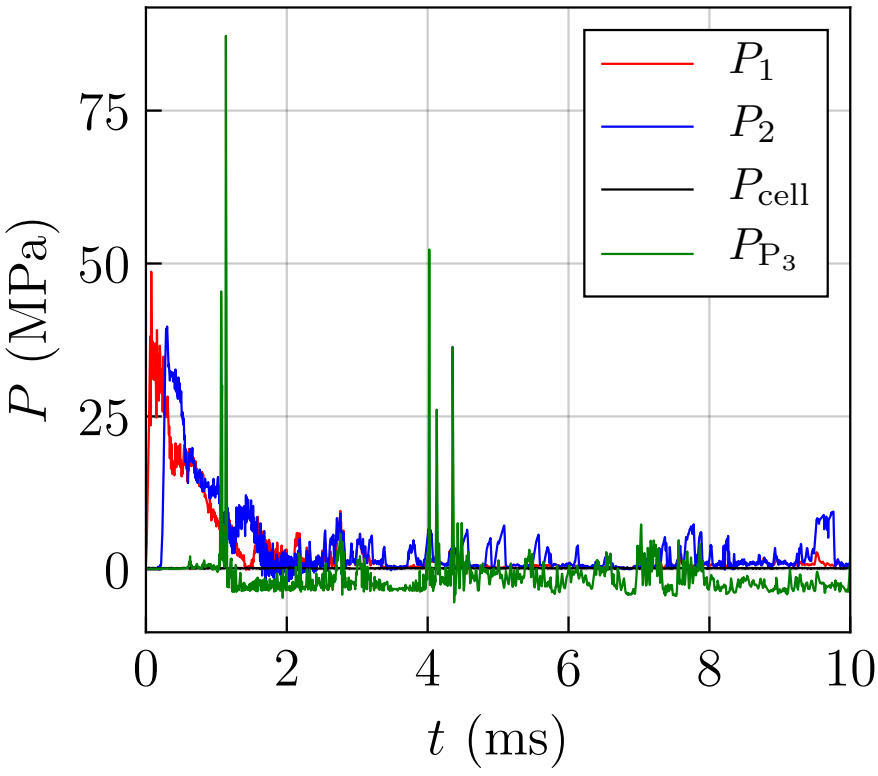

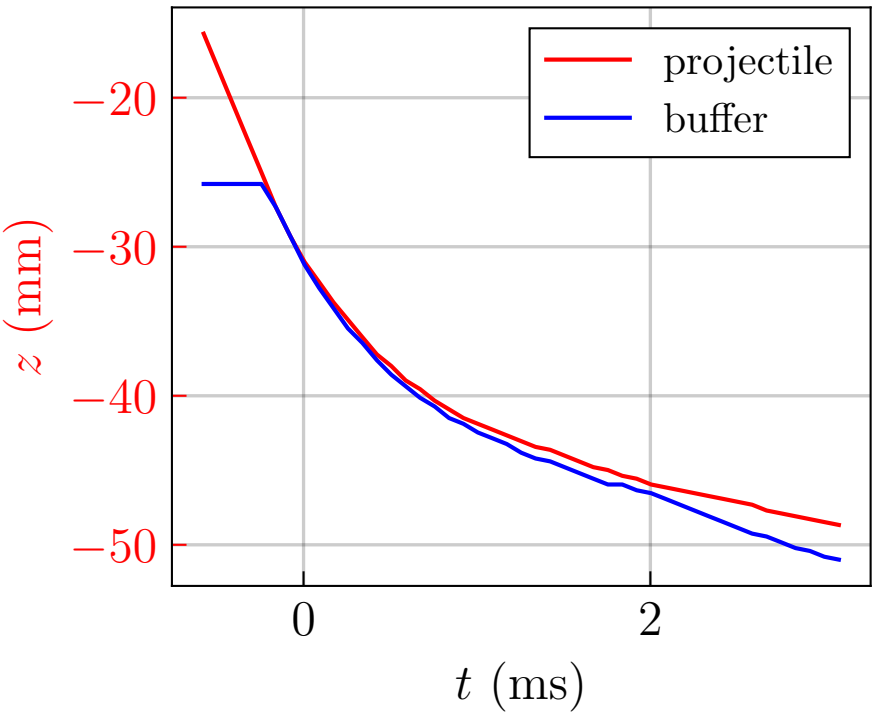

Figure 66: Test B043

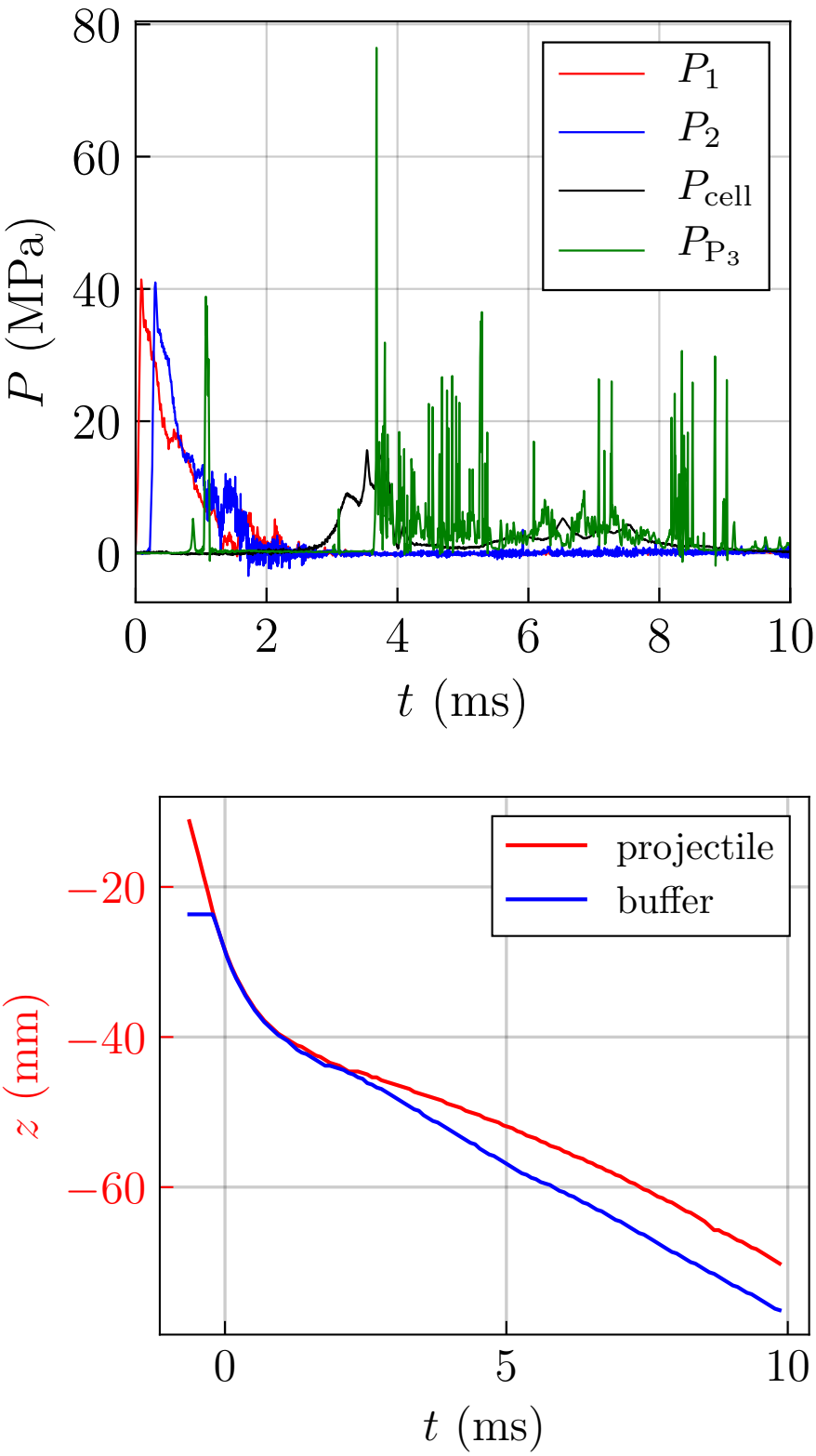

Figure 67: Test B044

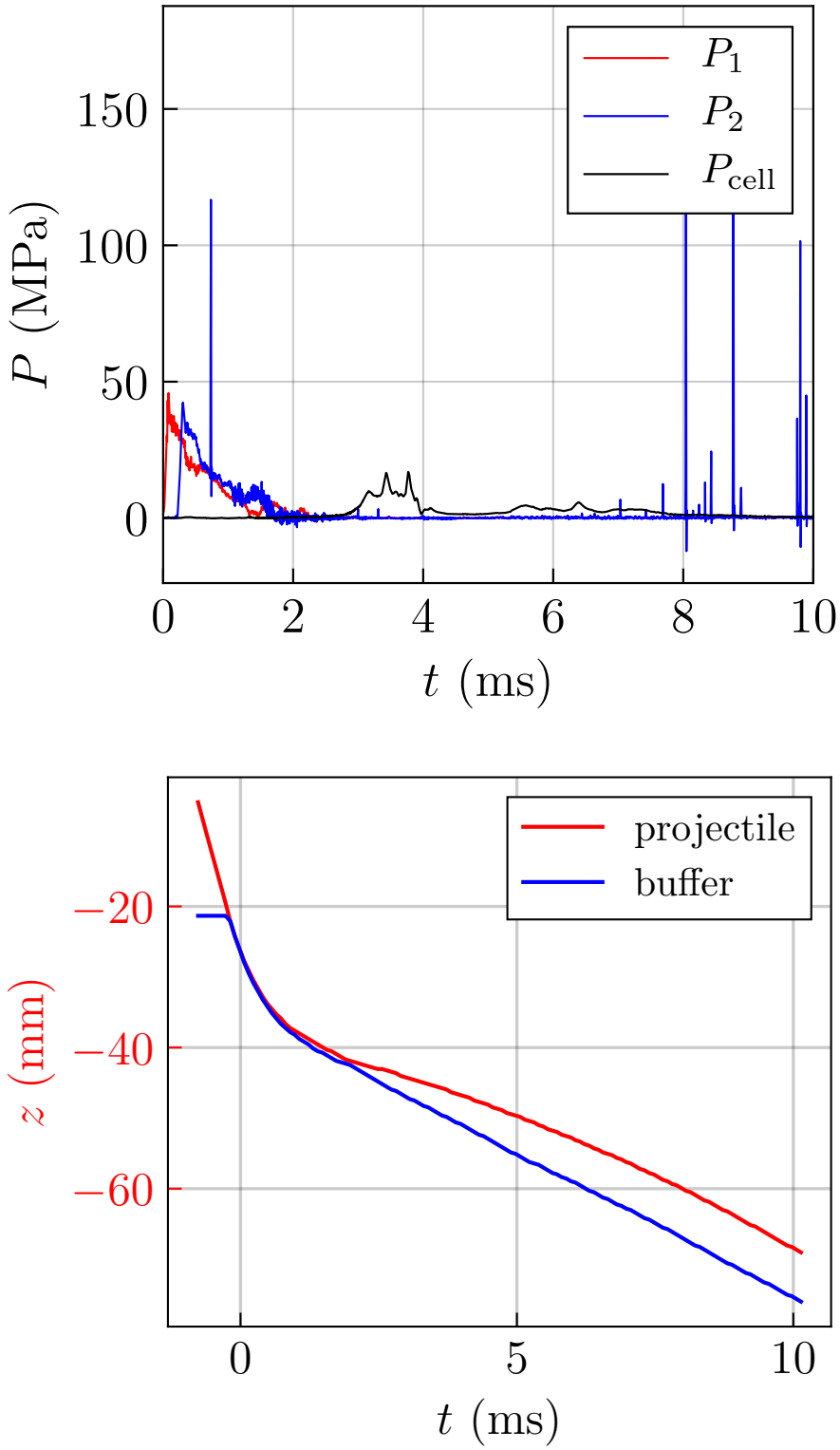

Figure 68: Test B045

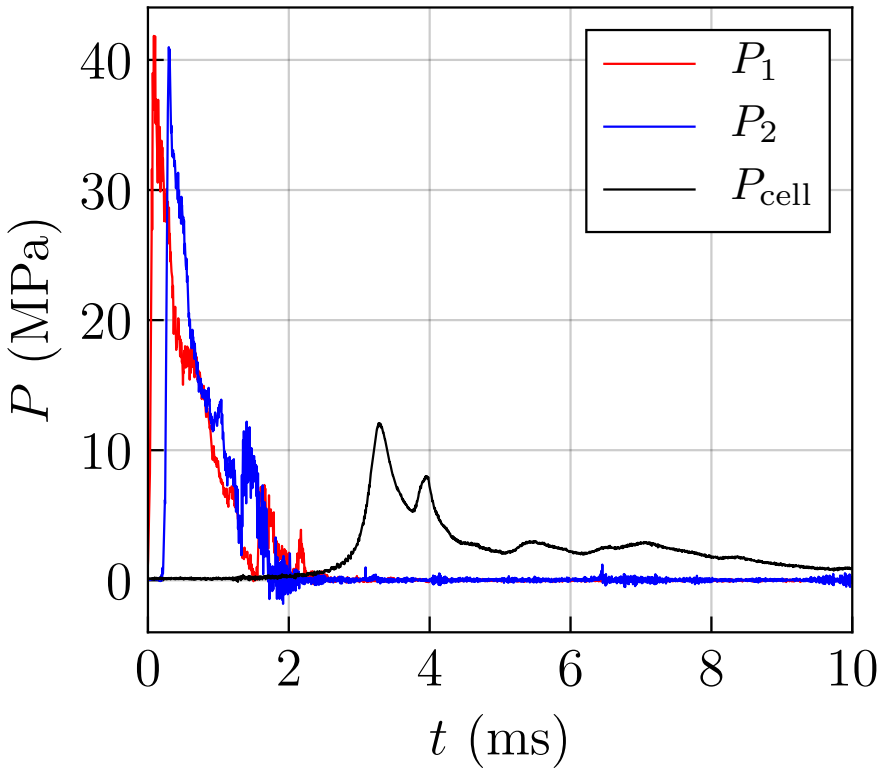

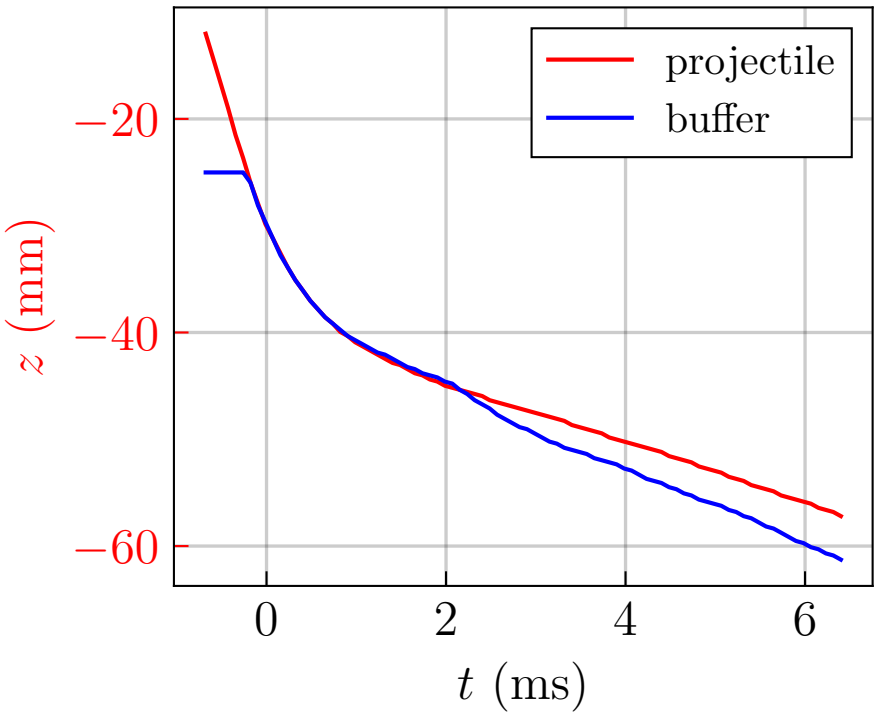

Figure 69: Test B046

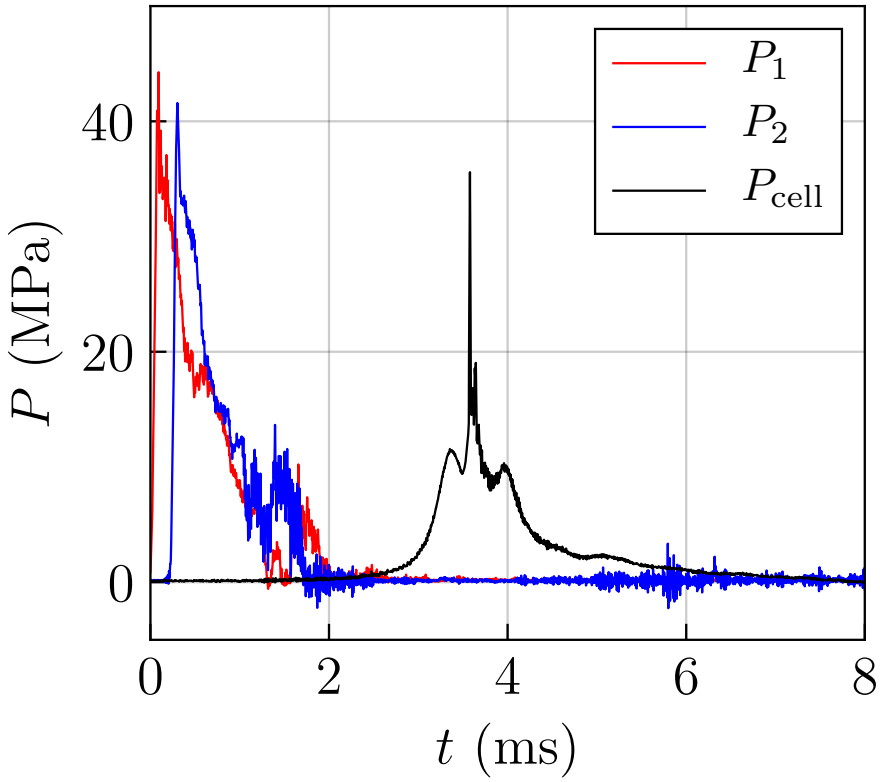

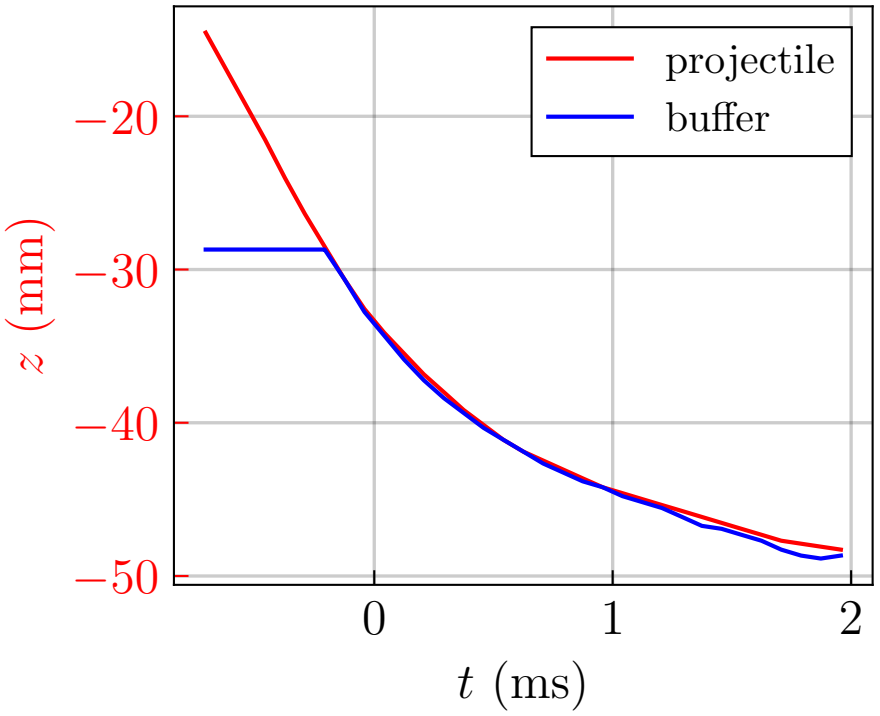

Figure 70: Test B047

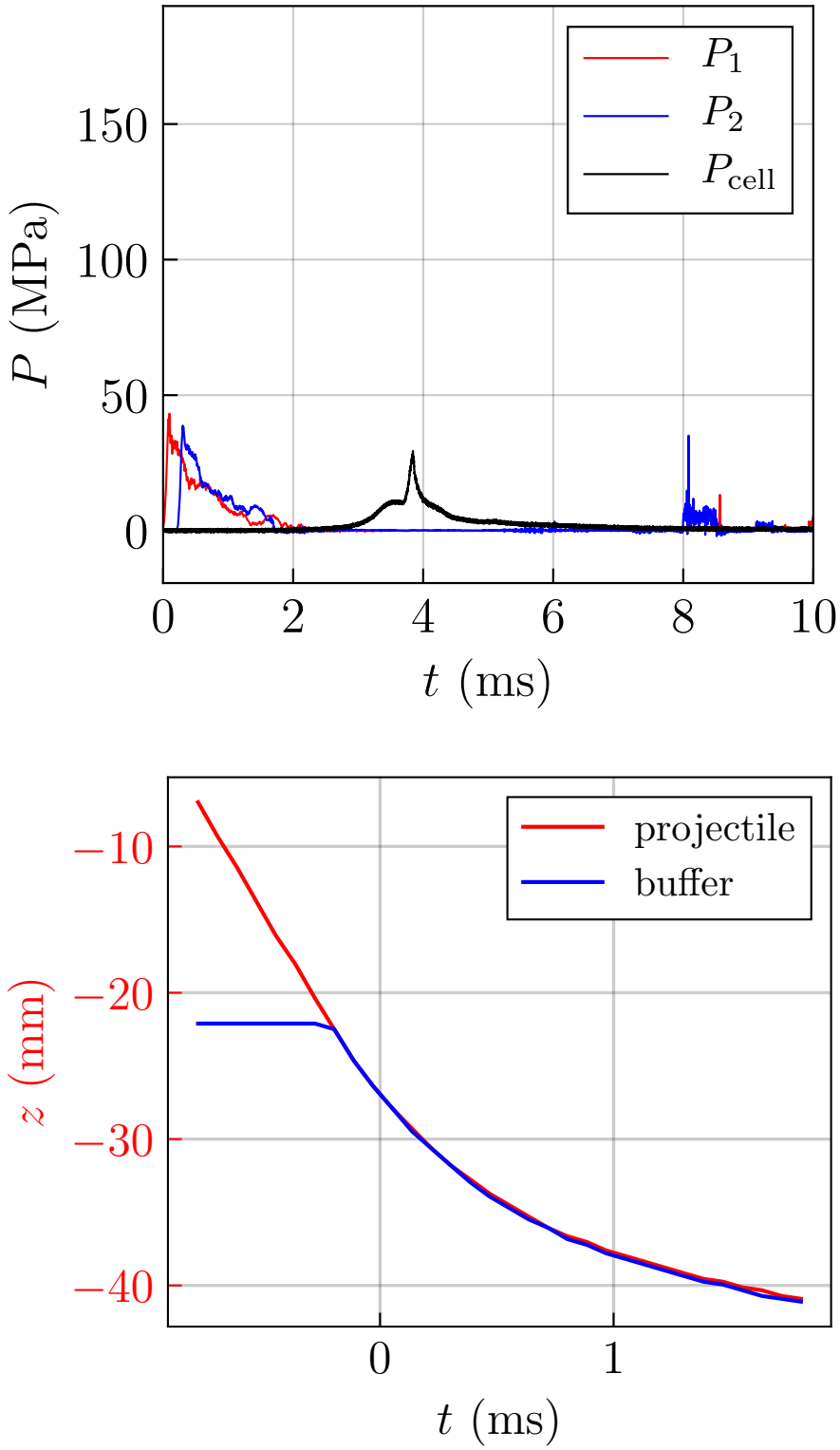

Figure 71: Test B048

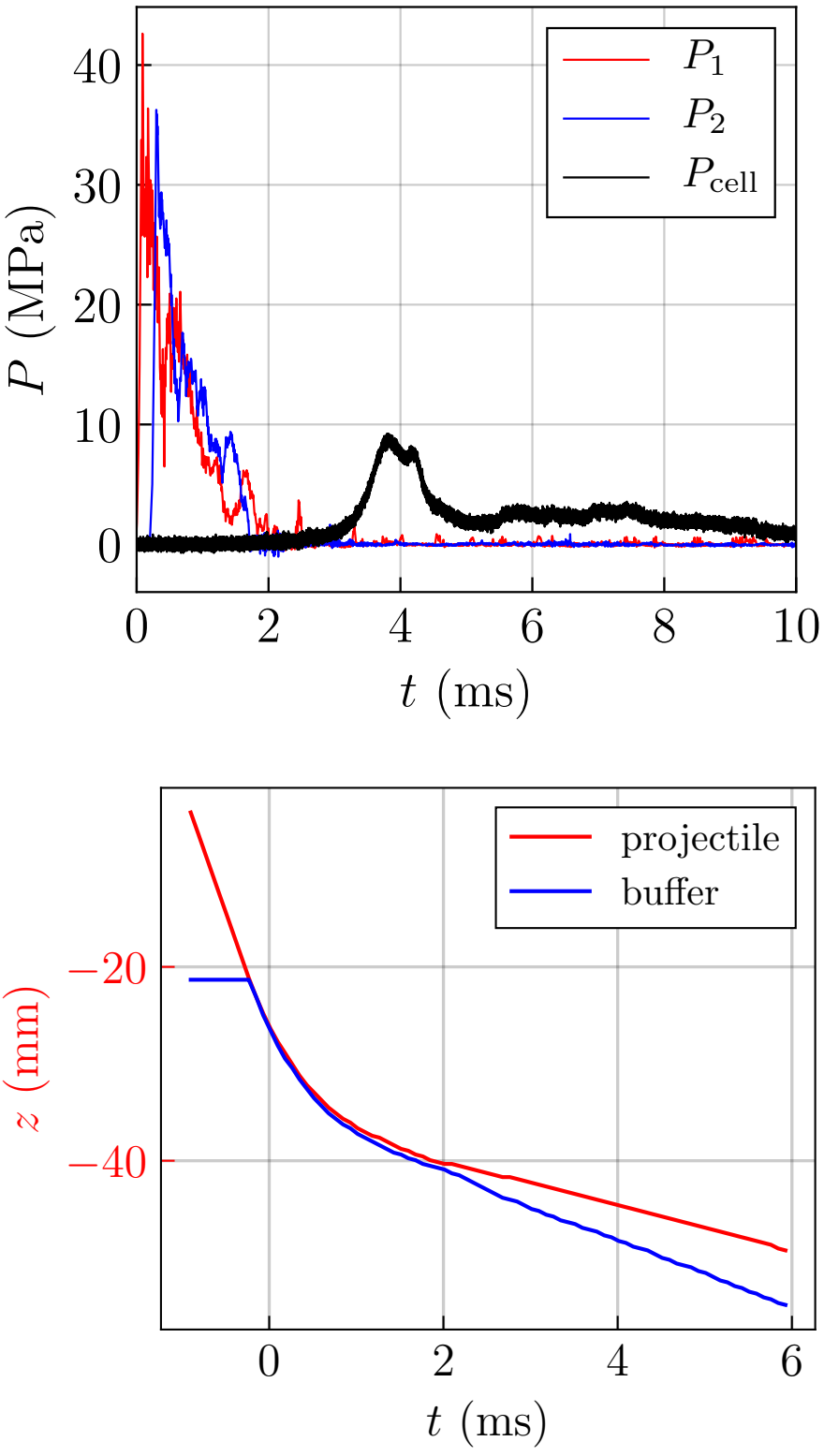

Figure 72: Test B049

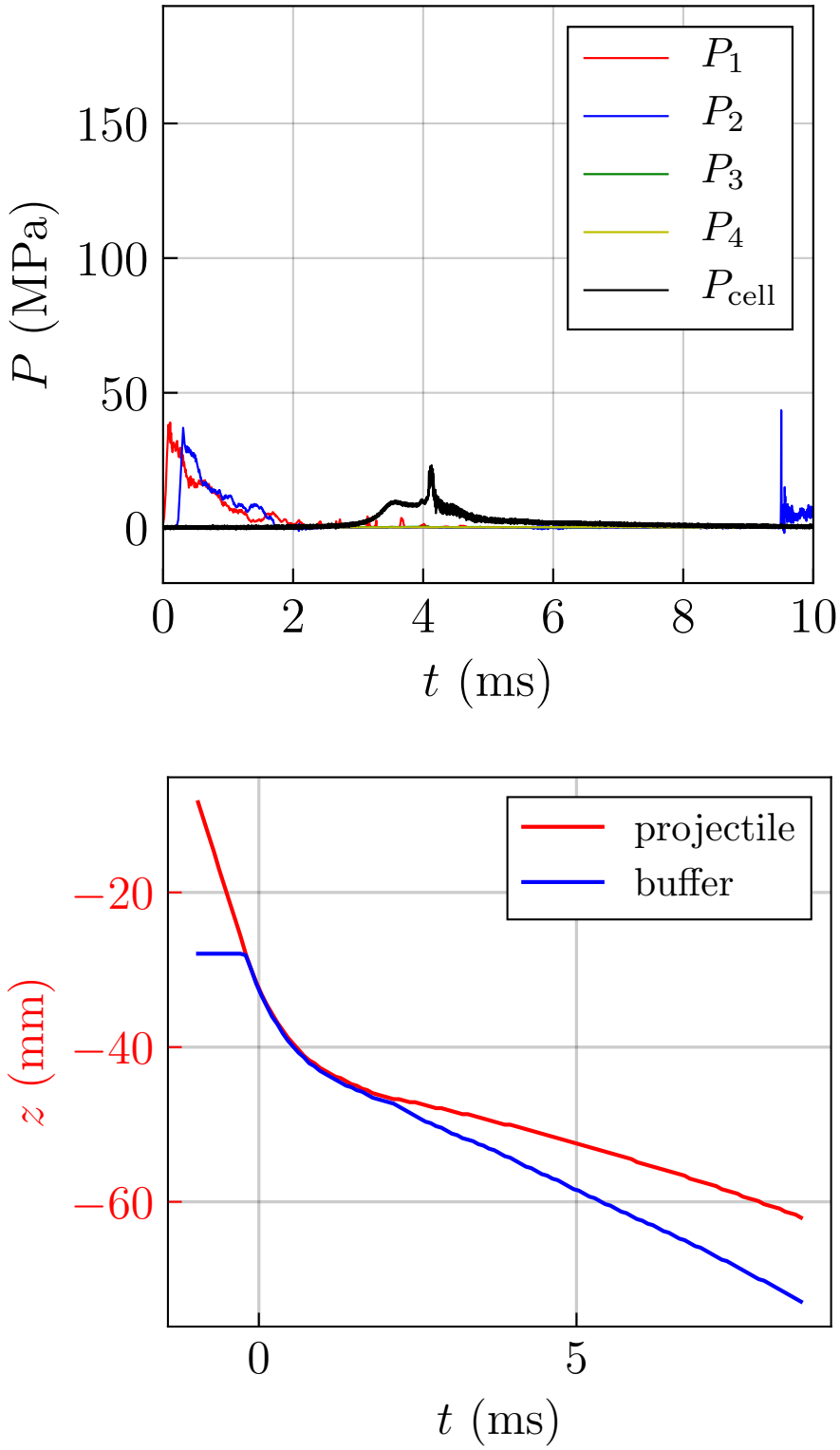

Figure 73: Test B050

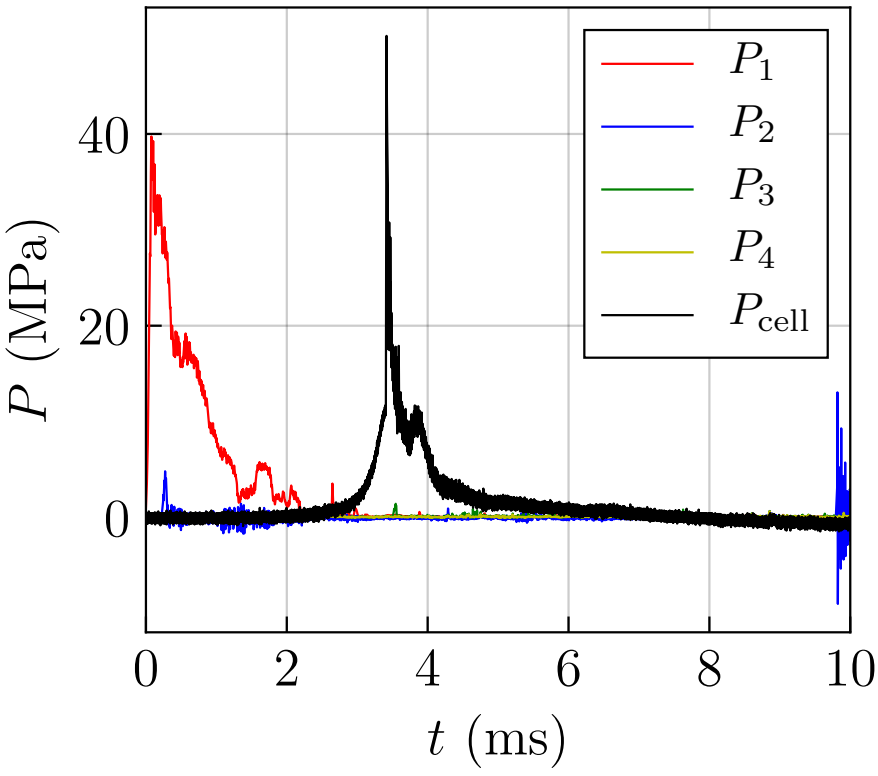

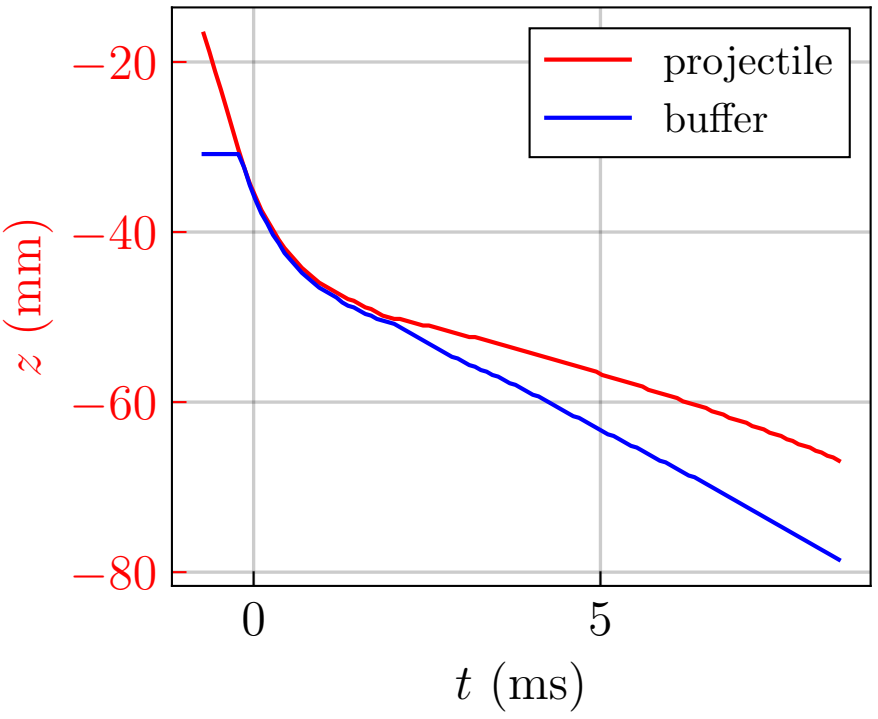

Figure 74: Test B051

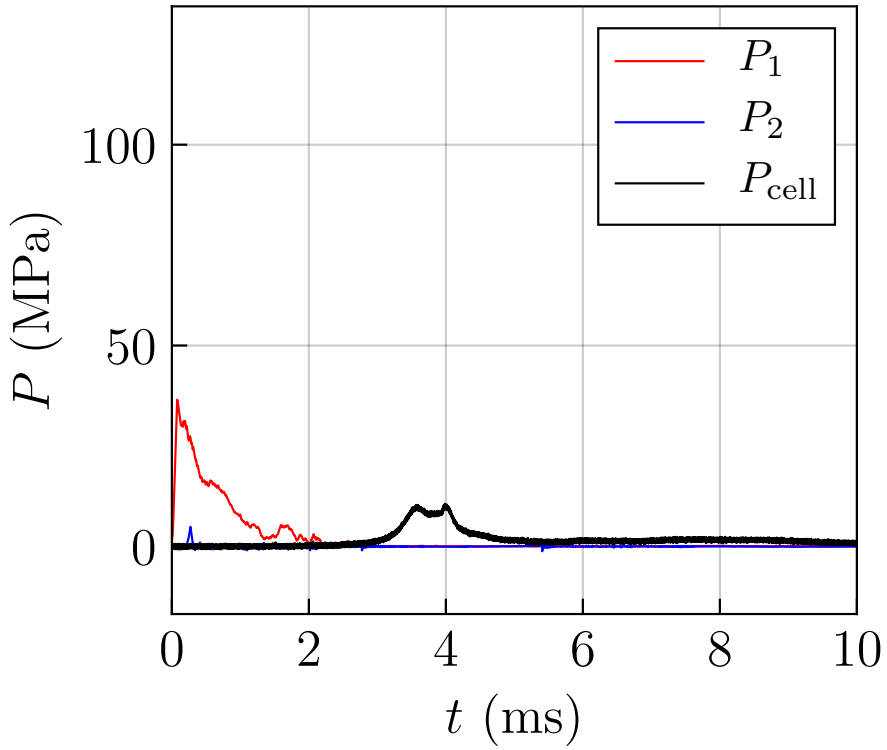

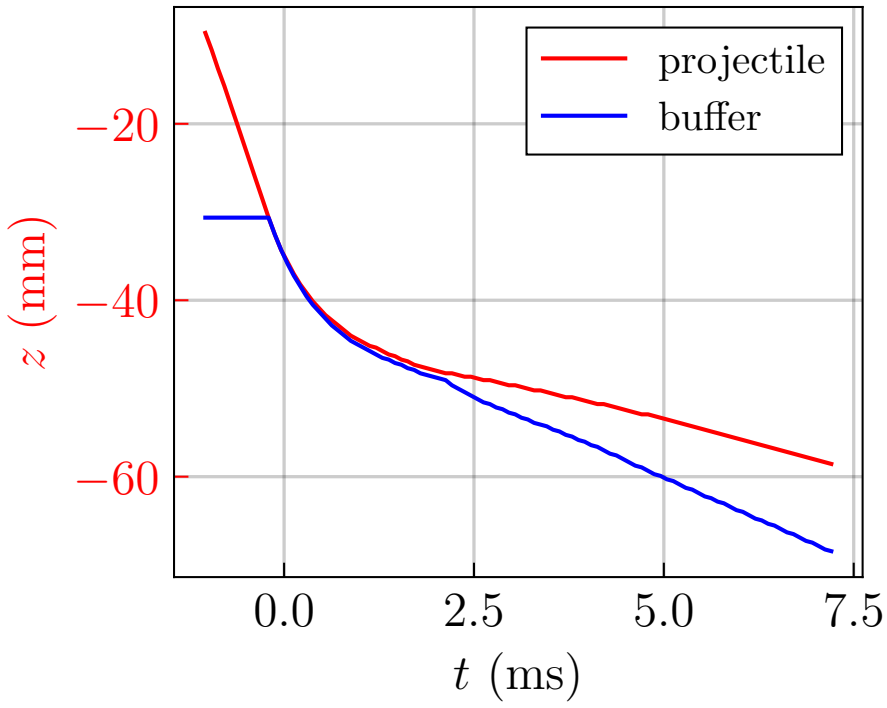

Figure 75: Test B052

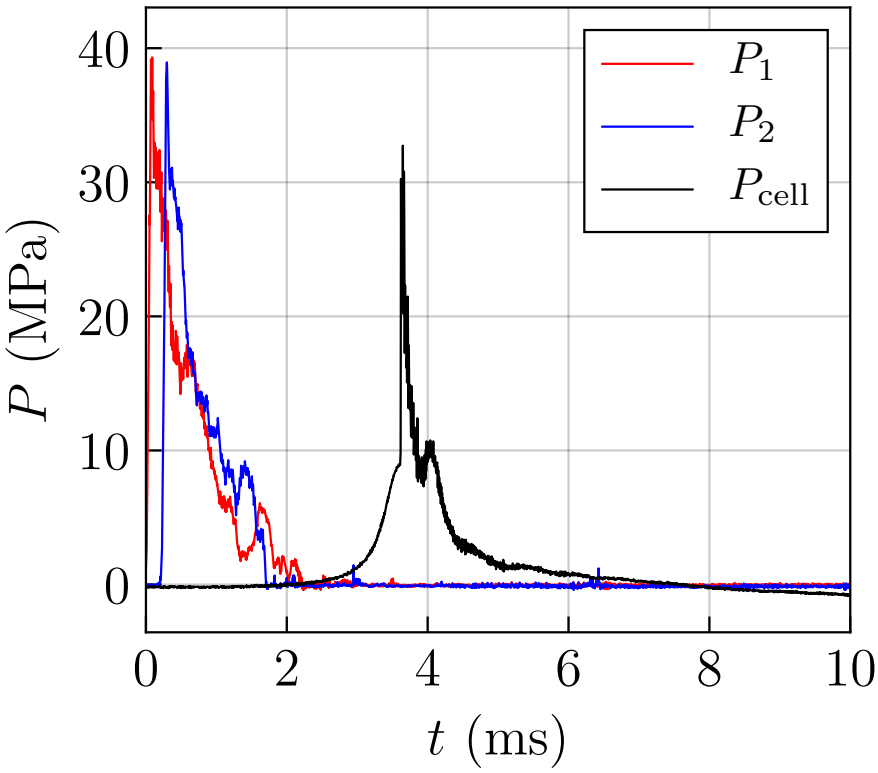

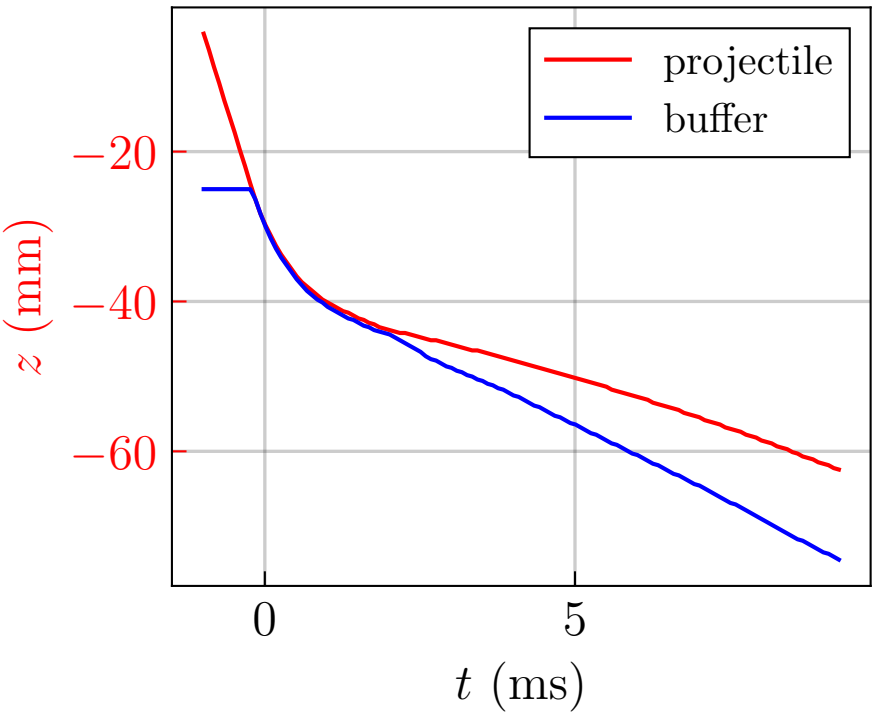

Figure 76: Test B053

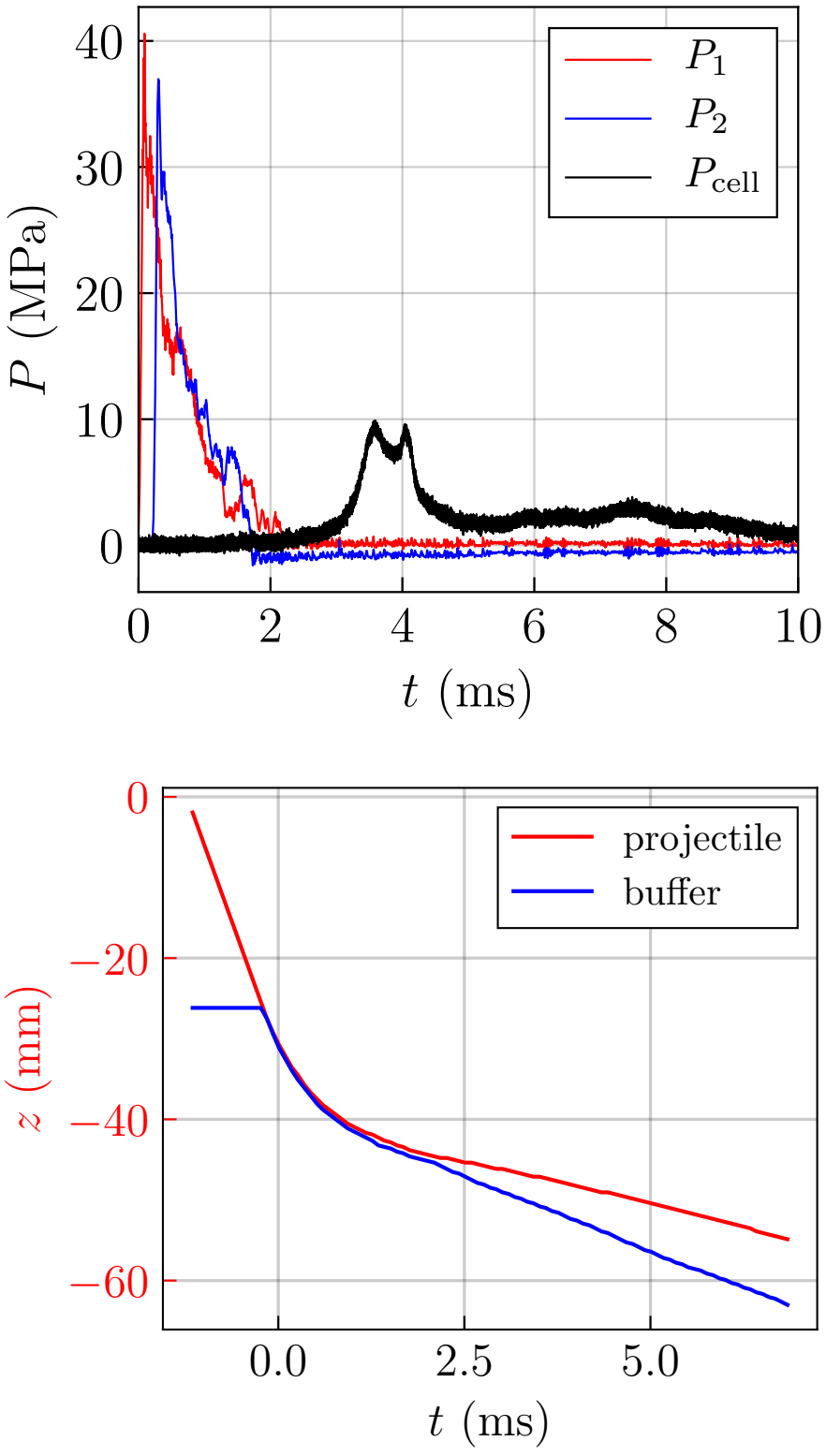

Figure 77: Test B054

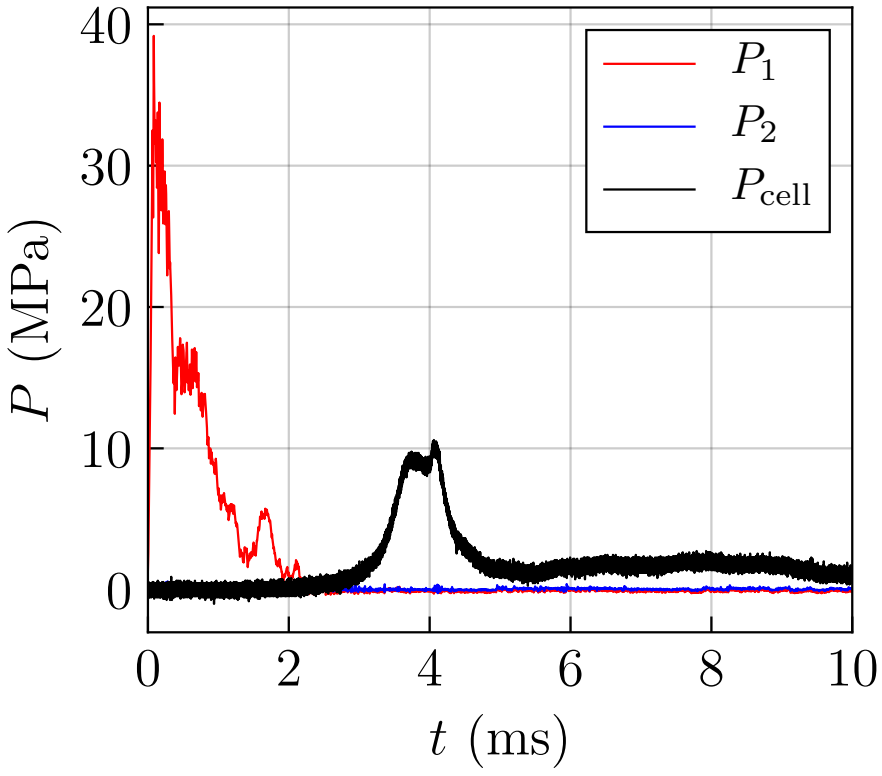

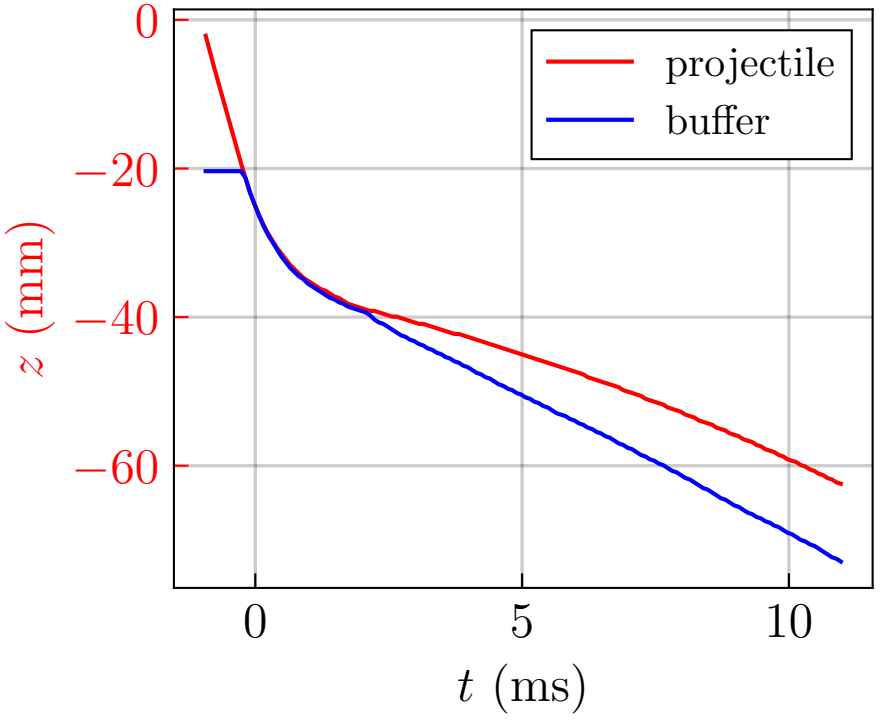

Figure 78: Test B055

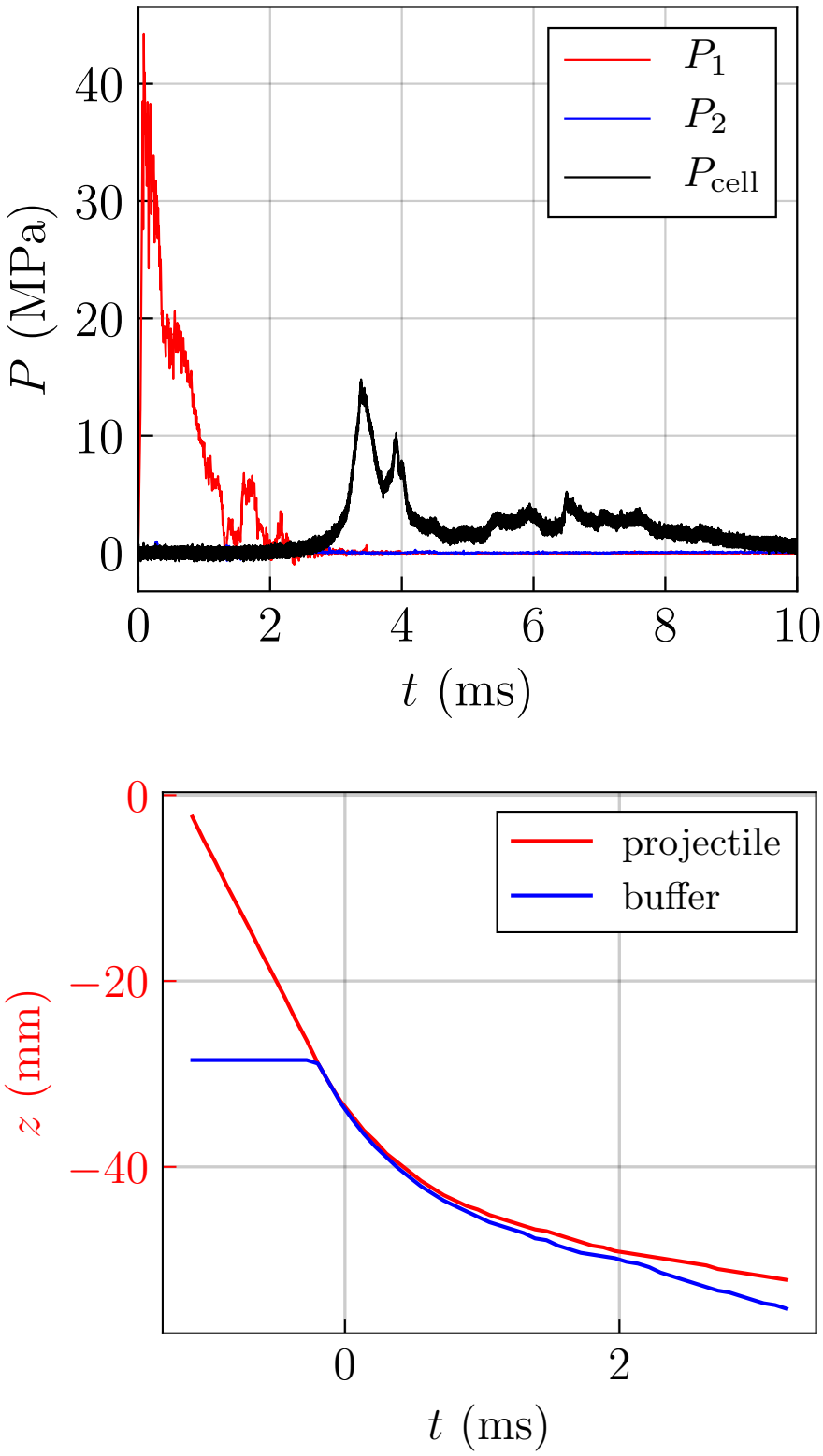

Figure 79: Test B056

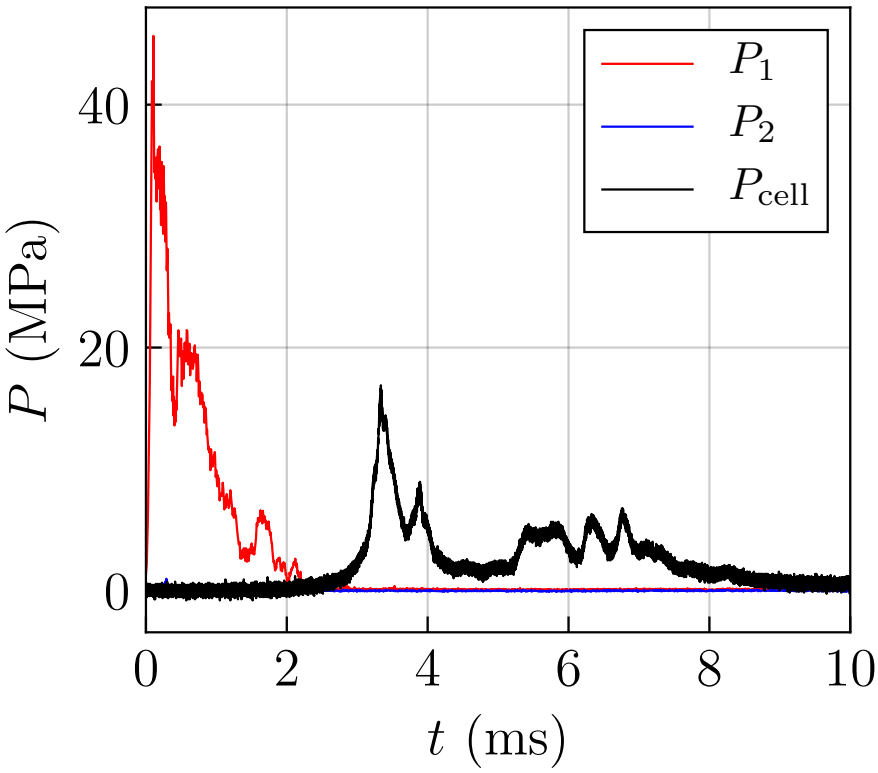

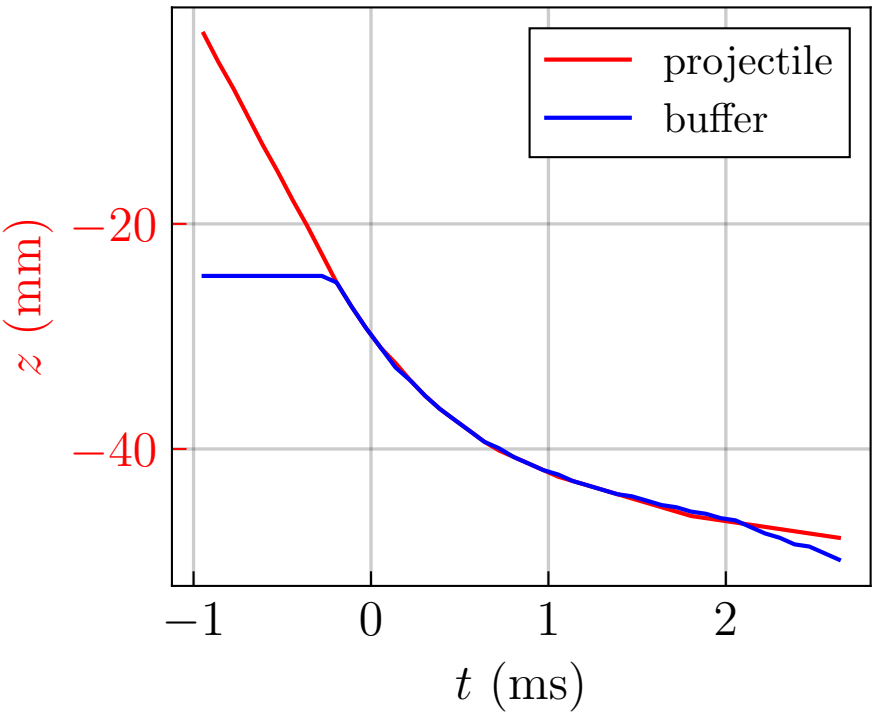

Figure 80: Test B057

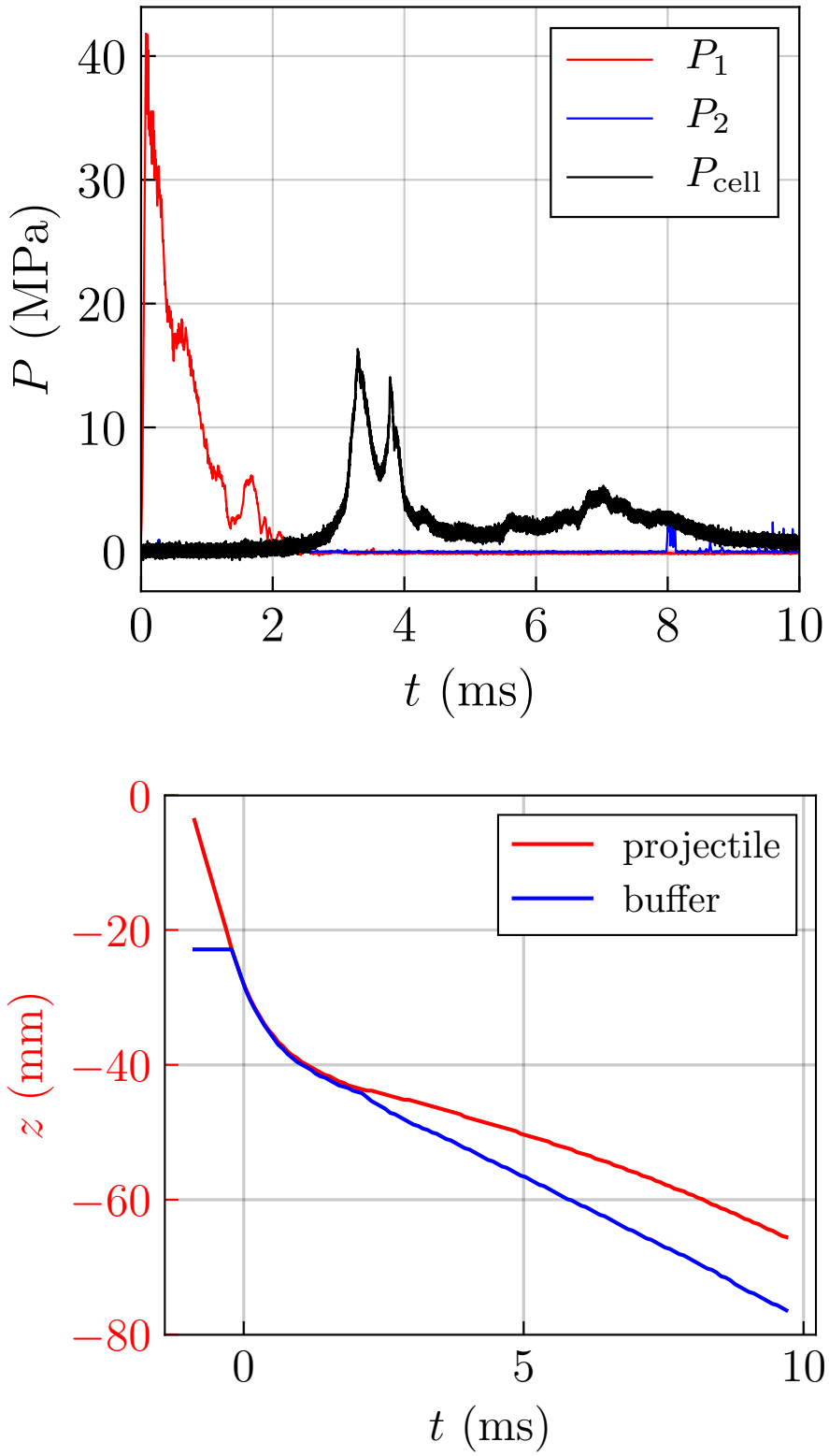

Figure 81: Test B058

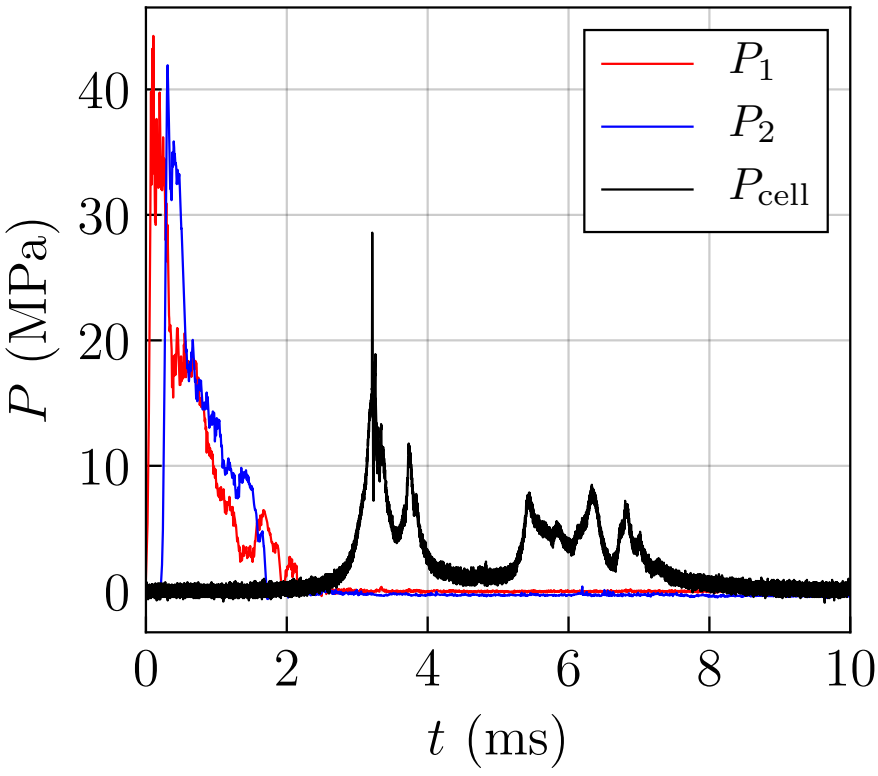

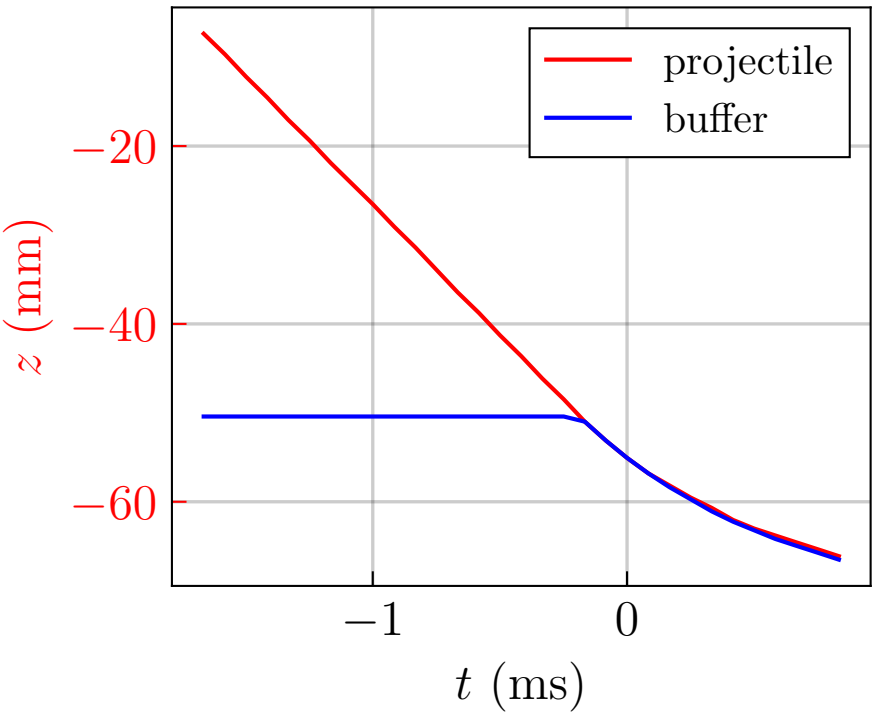

Figure 82: Test B059

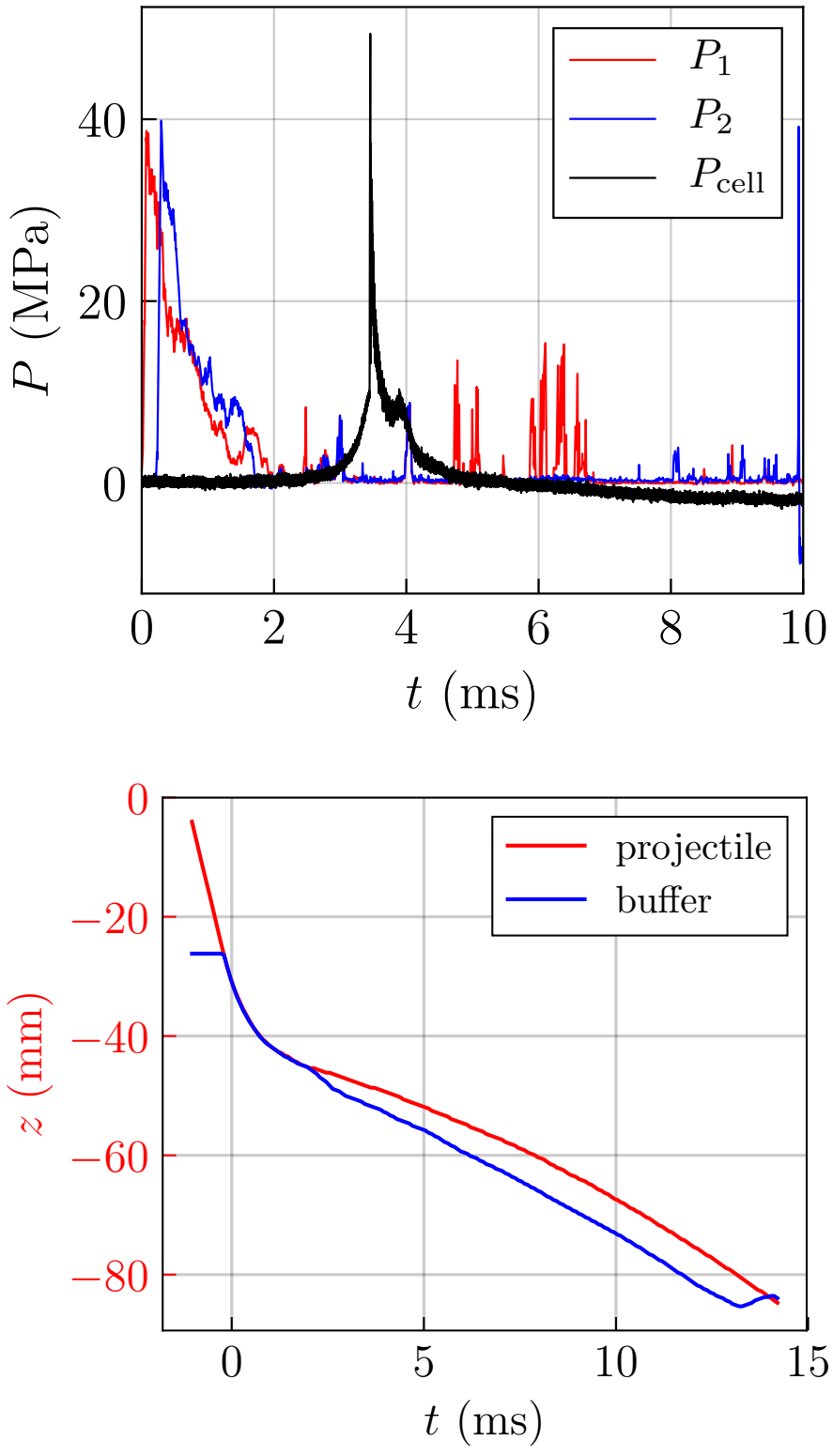

Figure 83: Test B060

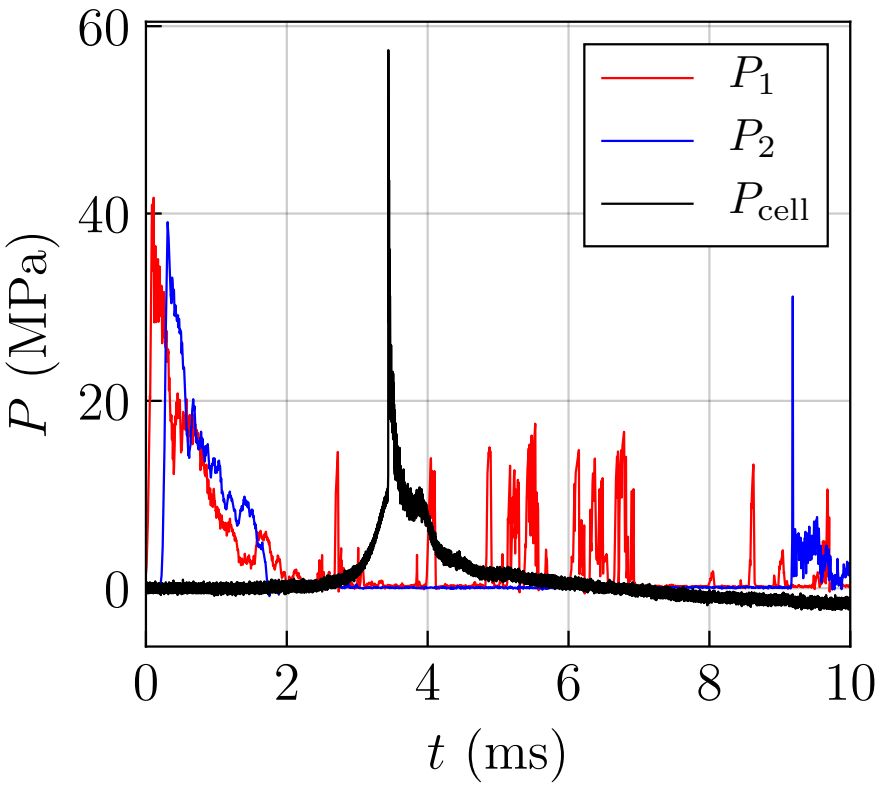

Figure 84: Test B061

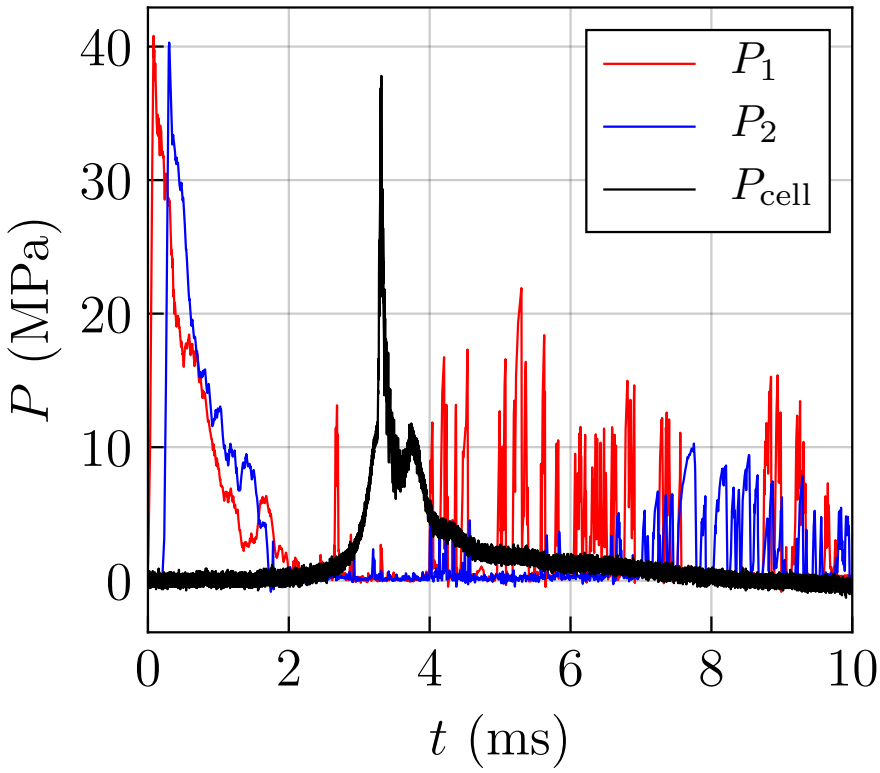

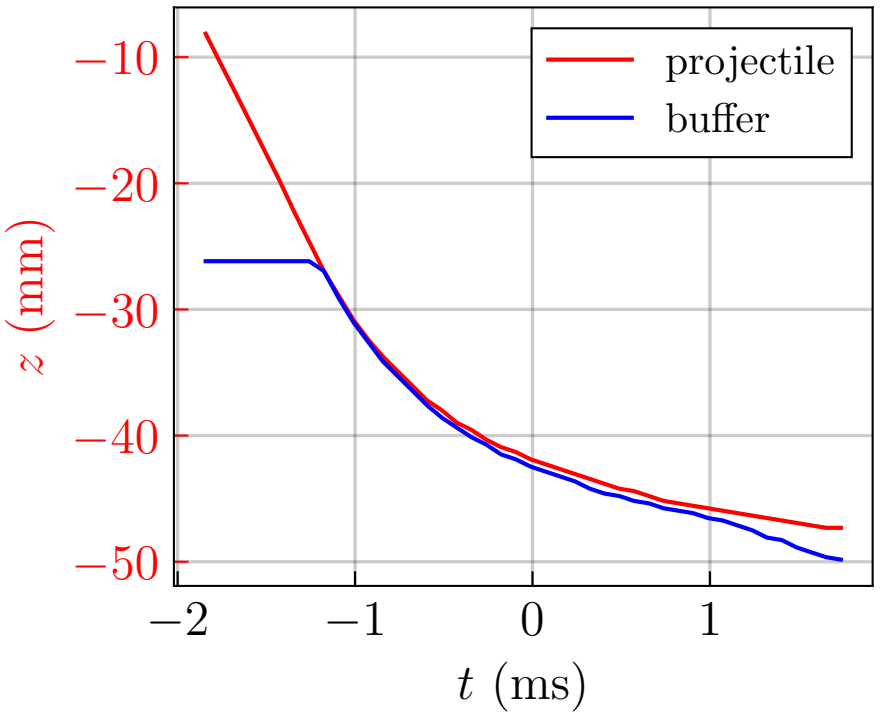

Figure 85: Test B062

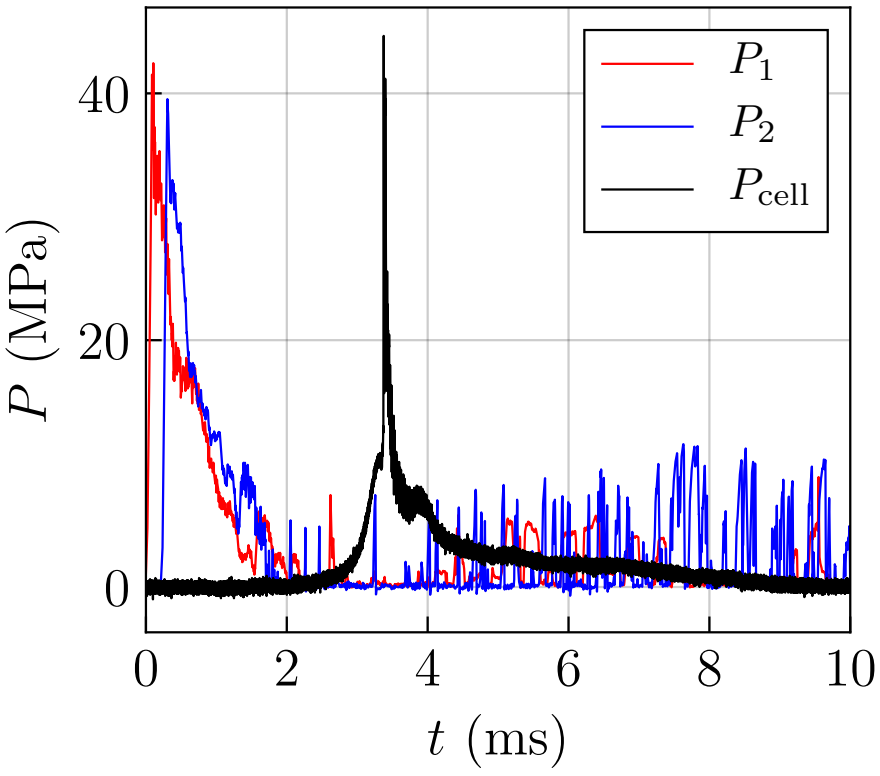

Figure 86: Test B063

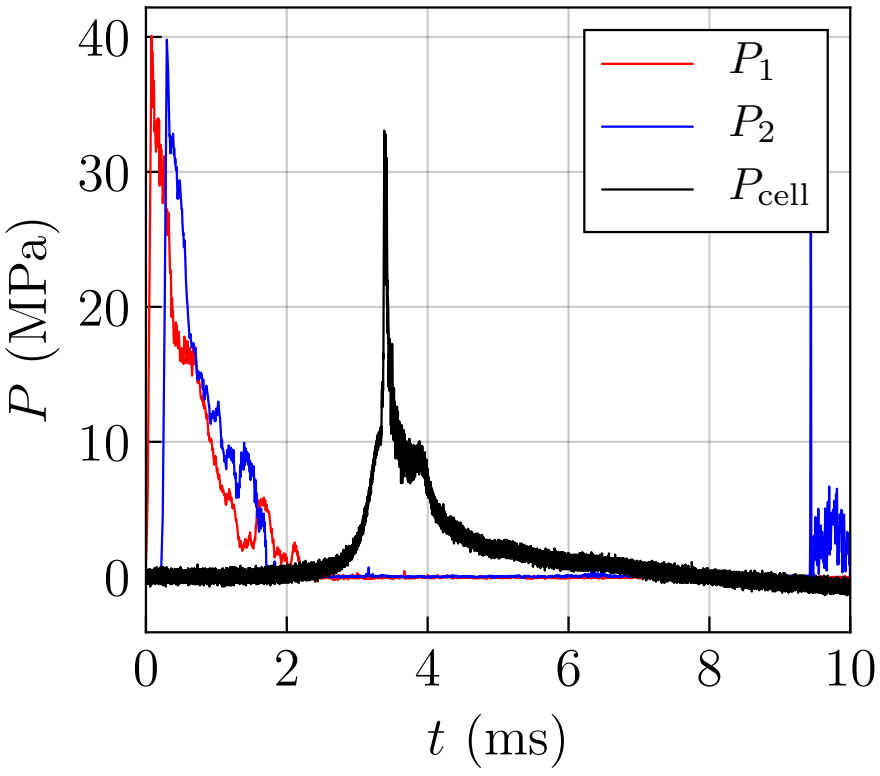

Figure 87: Test B064

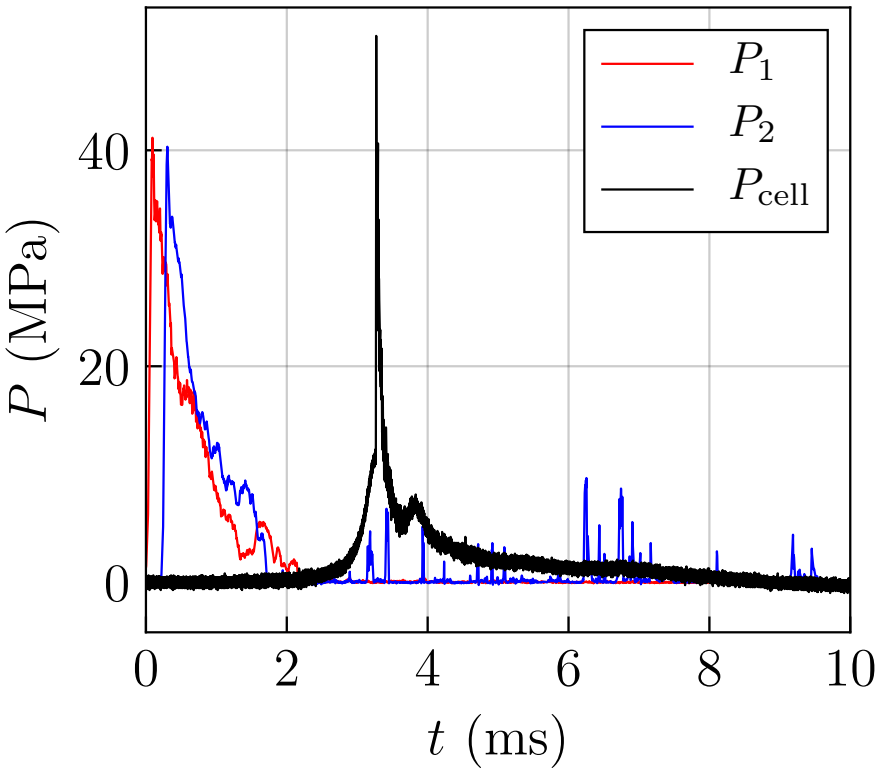

Figure 88: Test B065

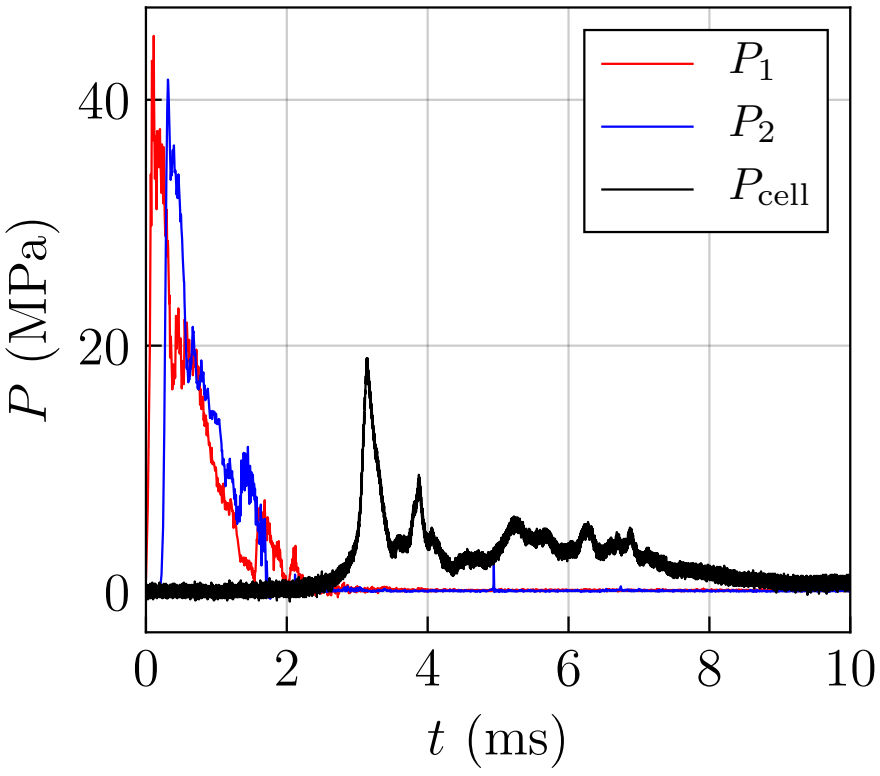

Figure 89: Test B066

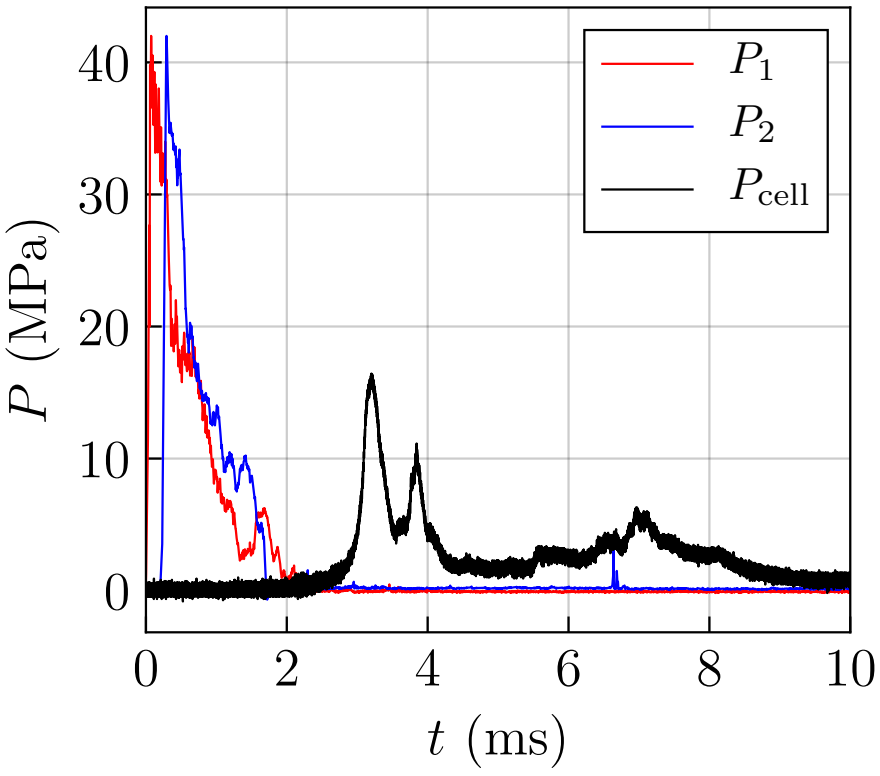

Figure 90: Test B067

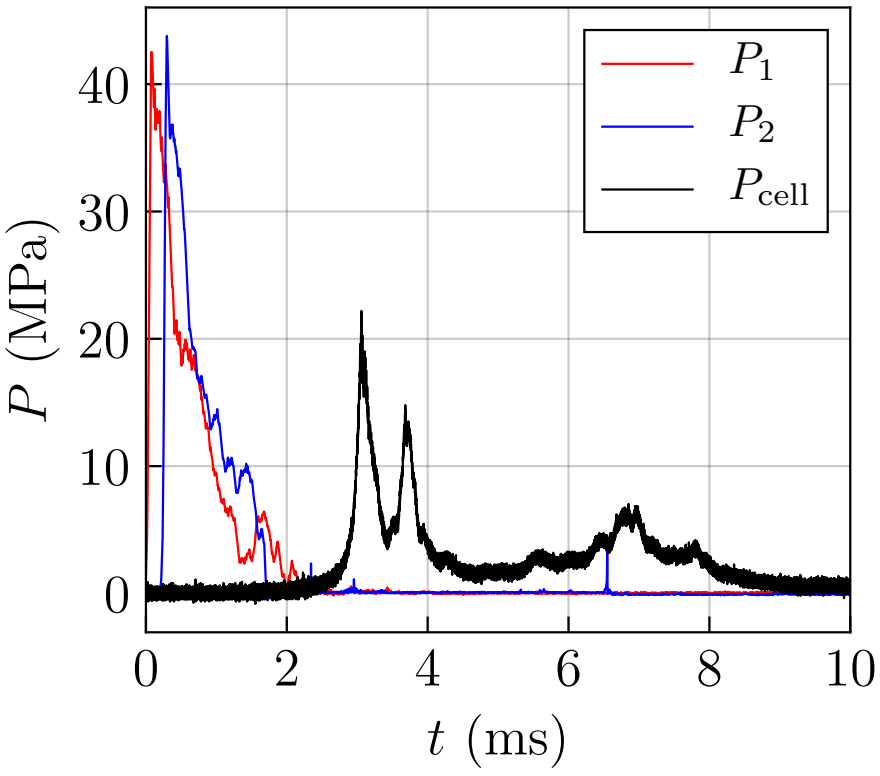

Figure 91: Test B068

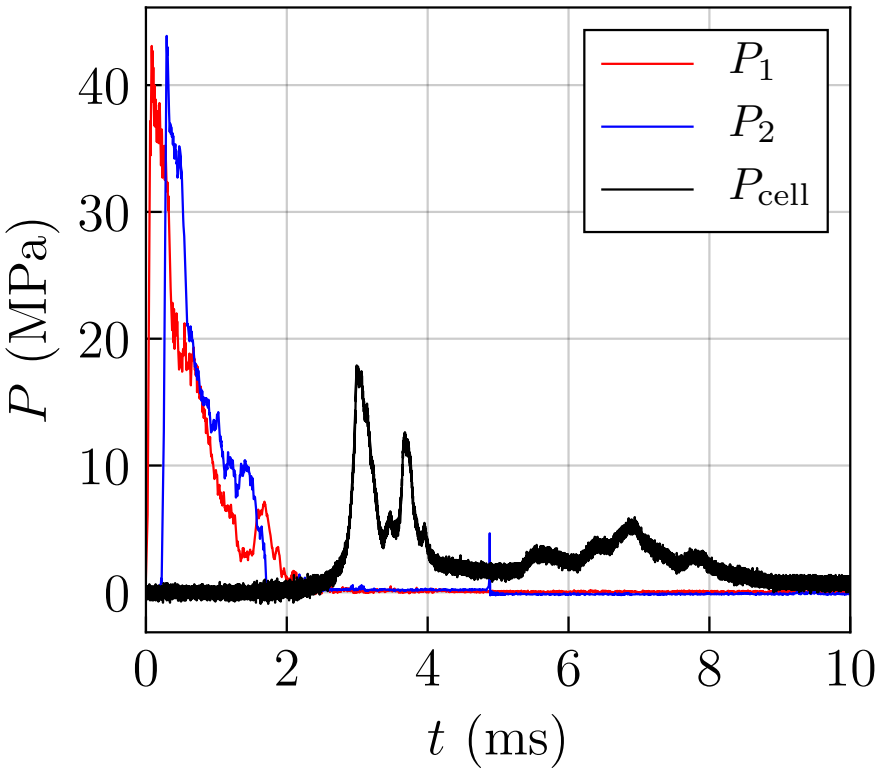

Figure 92: Test B069

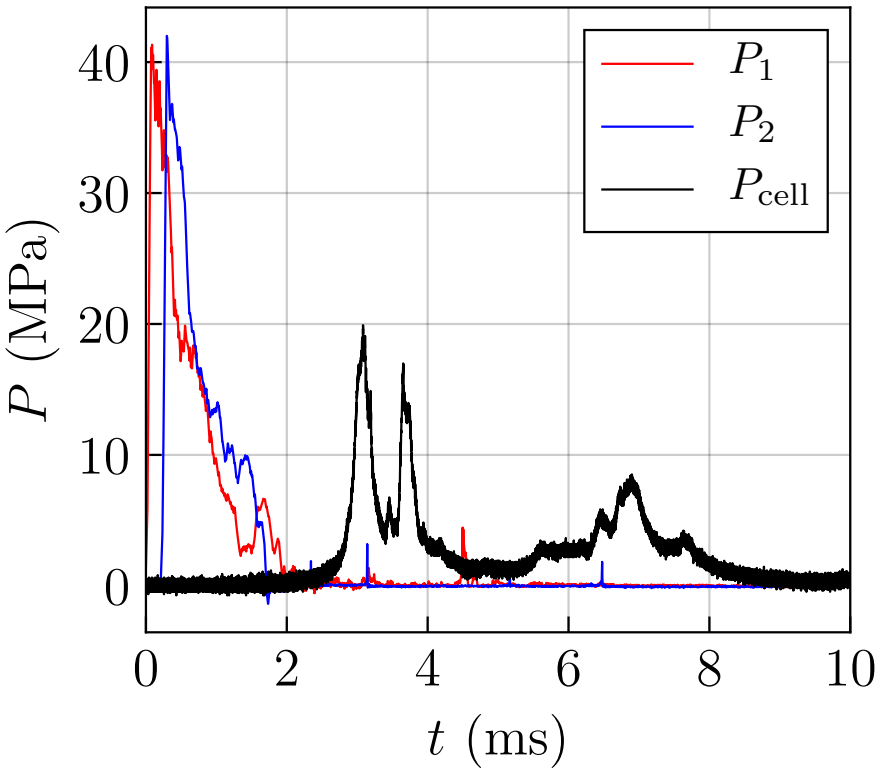

Figure 93: Test B070

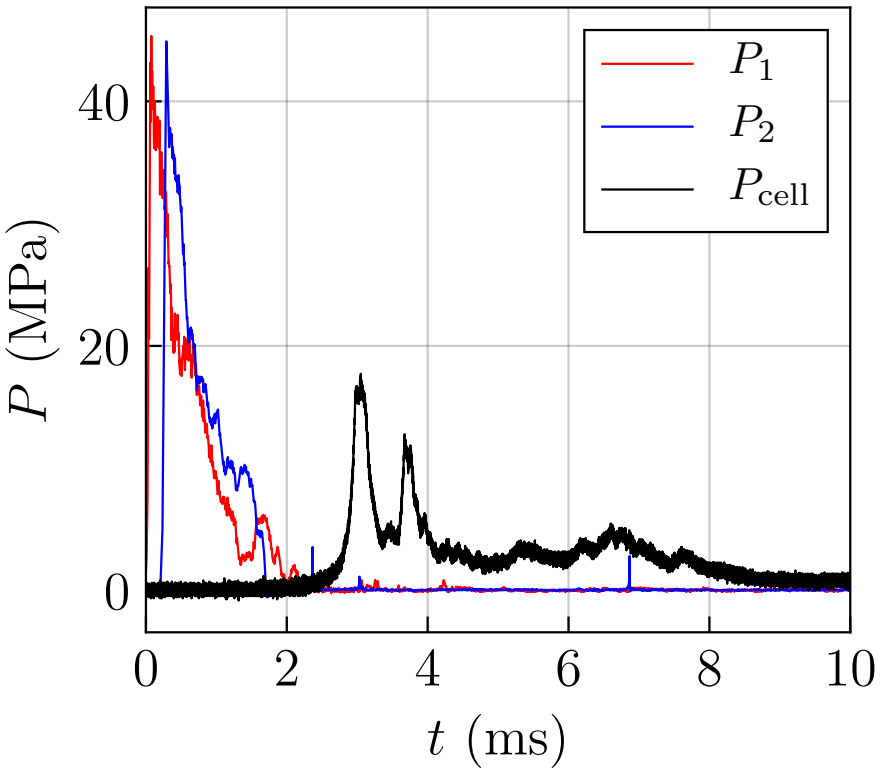

Figure 94: Test B071

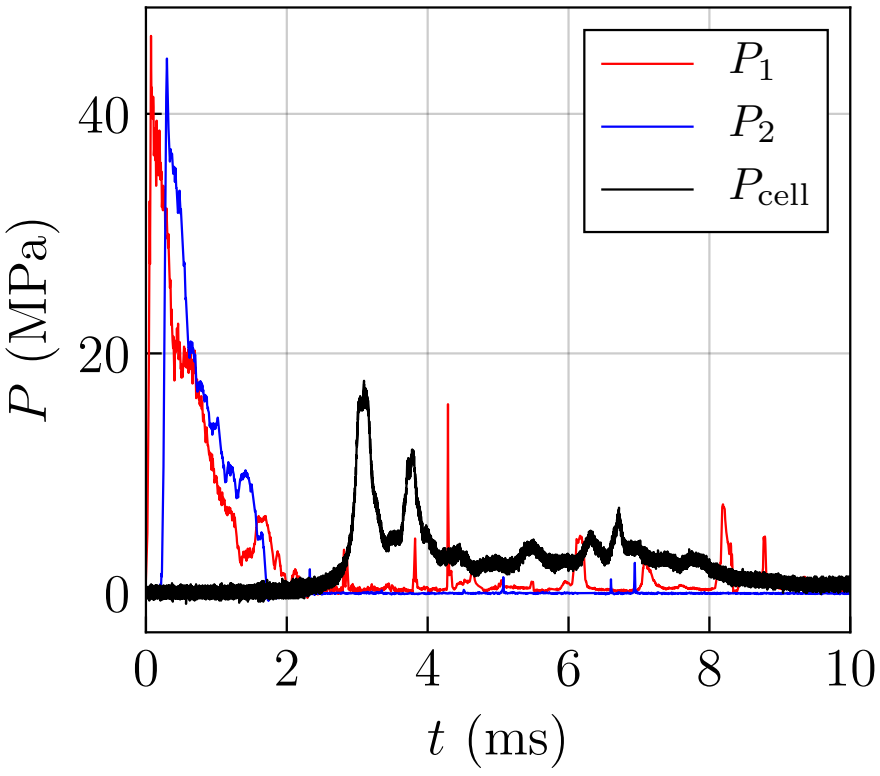

Figure 95: Test B072

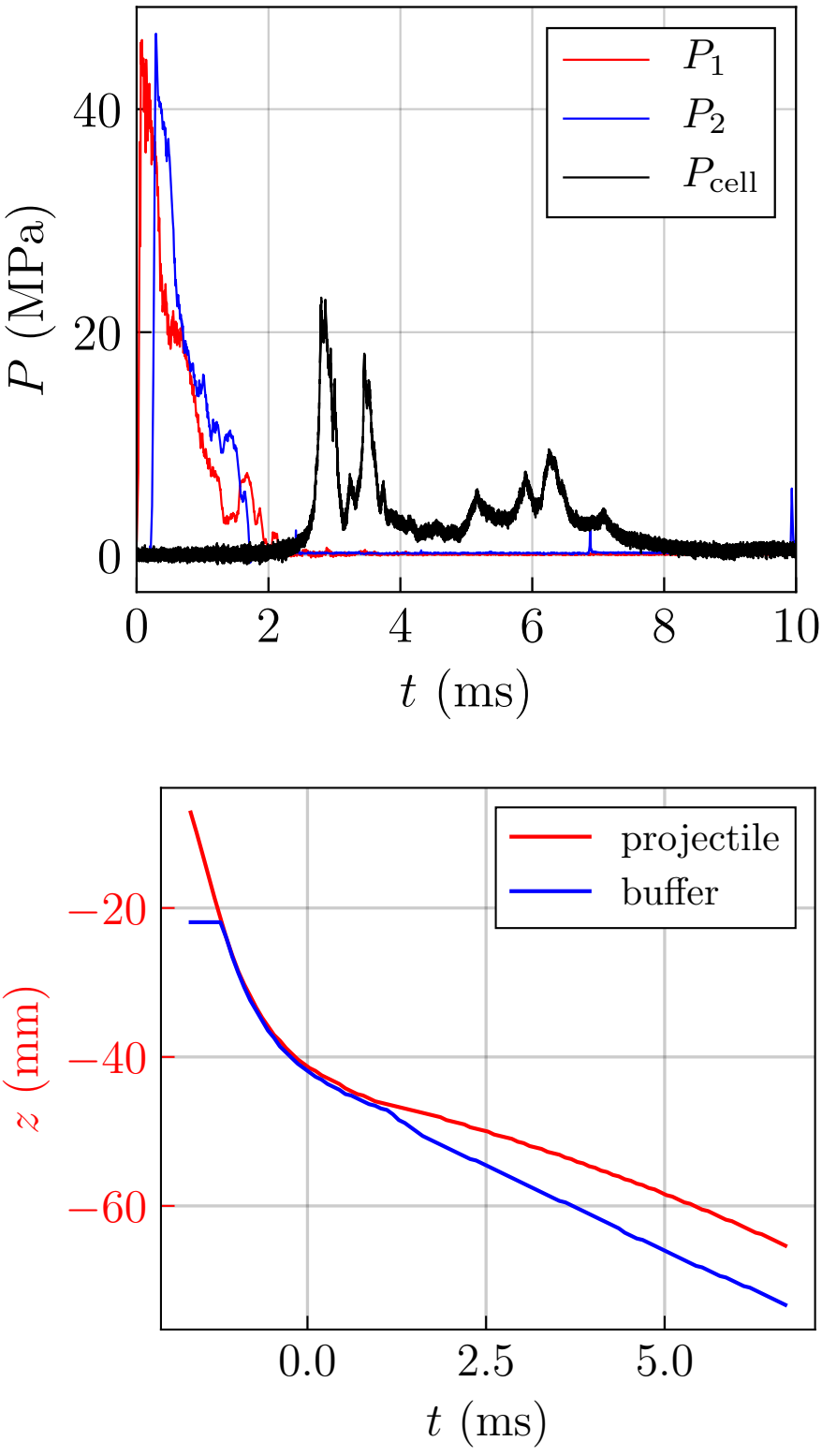

Figure 96: Test B073

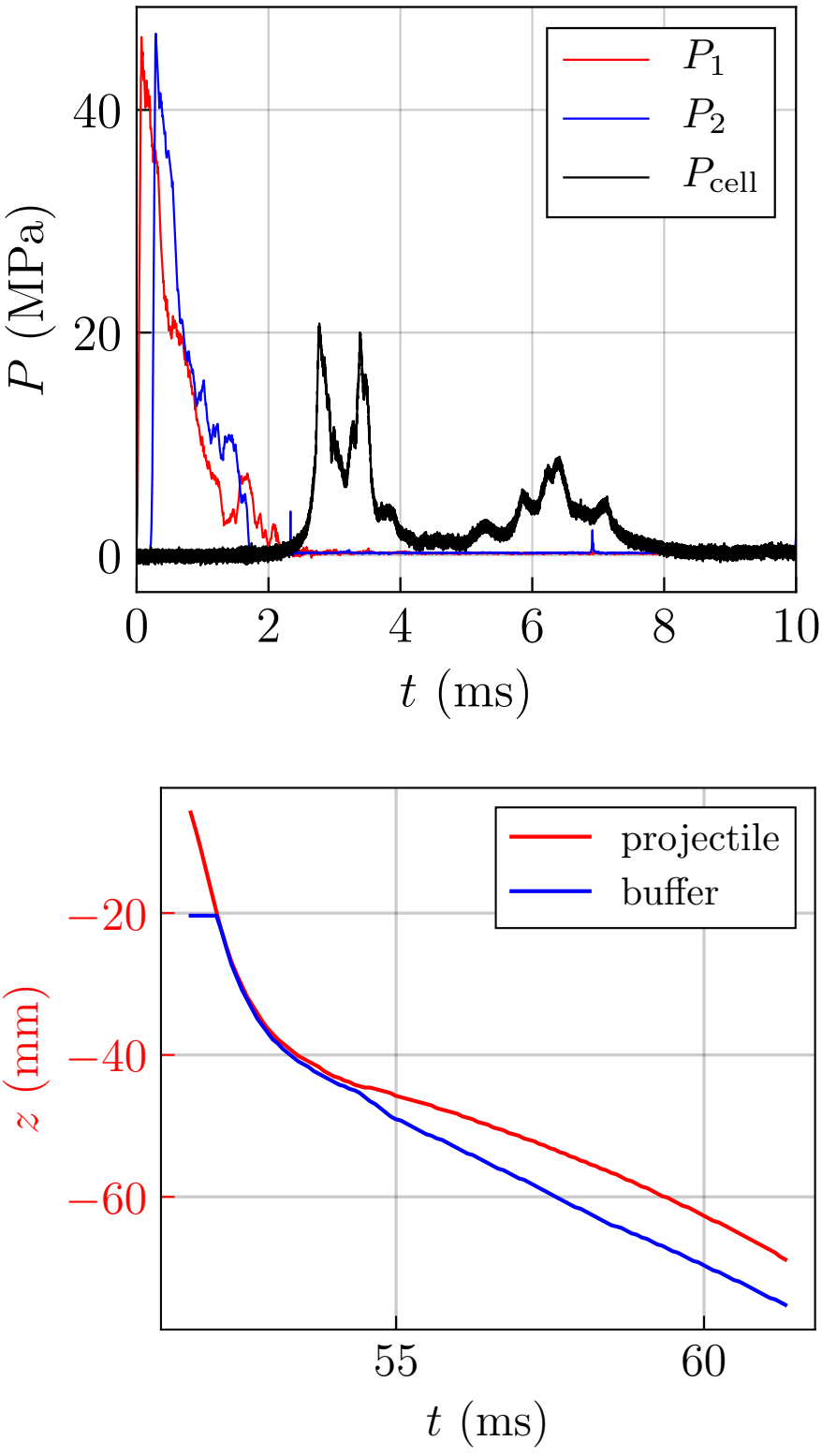

Figure 97: Test B074